

Jordan Journal of
P H Y S I C S

An International Peer-Reviewed Research Journal

Volume 1, No. 1, June 2008, Jumada 1 1429 H

Jordan Journal of Physics (JJP): An International Peer-Reviewed Research Journal established by the Higher Research Committee, Ministry of Higher Education & Scientific Research, Jordan, and published quarterly by the Deanship of Research & Graduate Studies, Yarmouk University, Irbid, Jordan.

EDITOR-IN-CHIEF:

Ibrahim O. Abu Al-Jarayesh

Department of Physics, Yarmouk University, Irbid, Jordan.

E-mail: ijaraysh@yu.edu.jo

EDITORIAL BOARD:

Hisham B. Ghassib

President: Princess Sumaya University for Technology, Amman, Jordan.

E-mail: ghassib@psut.edu.jo

Nabil Y. Ayoub

German Jordanian University, Amman, Jordan.

E-mail: nabil.ayoub@qju.edu.jo

Marwan S. Mousa

Department of Physics, Mu'tah University, Al-Karak, Jordan.

E-mail: mmousa@mutah.edu.jo

Sami H. Mahmood

Department of Physics, Yarmouk University, Irbid, Jordan.

E-mail: mahmoods@yu.edu.jo

Dia-Eddin M. Arafah

Department of Physics, University of Jordan, Amman, Jordan.

E-mail: darafah@ju.edu.jo

Nihad A. Yusuf

Department of Physics, Yarmouk University, Irbid, Jordan.

E-mail: nihad.yusuf@qju.edu.jo

Jamil M. Khalifeh

Department of Physics, University of Jordan, Amman, Jordan.

E-mail: jkhalifa@ju.edu.jo

LANGUAGE EDITOR: Ahmad Saleh.

EDITORIAL SECRETARY: Majdi Al-Shannaq.

Manuscripts should be submitted to:

Prof. Ibrahim O. Abu Al-Jarayesh
Editor-in-Chief, Jordan Journal of Physics
Deanship of Research and Graduate Studies
Yarmouk University-Irbid-Jordan
Tel. 00 962 2 7211111 Ext. 3735
E-mail: jjp@yu.edu.jo
Website: <http://jjp.yu.edu.jo>

Jordan Journal of PHYSICS

An International Peer-Reviewed Research Journal

Volume 1, No. 1, June 2008, Jumada 1 1429 H

INTERNATIONAL ADVISORY BOARD

Prof. Dr. Ahmad Saleh

Department of Physics, Yarmouk University, Irbid, Jordan.
salema@yu.edu.jo

Prof. Dr. Aurore Savoy-Navarro

LPNHE Universite de Paris 6/IN2P3-CNRS, Tour 33, RdC 4,
Place Jussieu, F 75252, Paris Cedex 05, France.
auore@lpnhe.in2p3.fr

Prof. Dr. Bernard Barbara

Laboratoire Louis Neel, Salle/Room: D 108, 25, Avenue des
Martyrs BP 166, 38042-Grenoble Cedex 9, France.
Barbara@grenoble.cnrs.fr

Prof. Dr. Bruno Guiderdoni

Observatoire Astronomique de Lyon, g, avenue Ch. Antre-F-
69561, Saint Genis Laval Cedex, France.
Bruno.guiderdoni@olos.univ-lyon1.fr

Prof. Dr. Buford Price

Physics Department, University of California, Berkeley, CA
94720, U. S. A.
bprice@berkeley.edu

Prof. Dr. Colin Cough

School of Physics and Astronomy, University of Birmingham,
B15 2TT, U. K.
c.cough@bham.ac.uk

Prof. Dr. Desmond Cook

Department of Physics, Condensed Matter and Materials
Physics Research Group, Old Dominion University, Norfolk,
Virginia 23529, U. S. A.
Dcook@physics.odu.edu

Prof. Dr. Evgeny Sheshin

MIPT, Institutskij per. 9, Dogoprudnyi 141700, Russia.
sheshin@lafaet.mipt.ru

Prof. Dr. Hans Ott

Laboratorium Fuer Festkorperphysik, ETH Honggerberg, CH-
8093 Zurich, Switzerland.
ott@solid.phys.ethz.ch

Prof. Dr. Herwig Schopper

President SESAME Council, Chairman Scientific Board
UNESCO IBSP Programme, CERN, 1211 Geneva, Switzerland.
Herwig.Schopper@cern.ch

Prof. Dr. Humam Ghassib

Department of Physics, Jordan University, Amman, Jordan.
hghassib@nic.net.jo

Prof. Dr. Ingo Hofmann

GSI Darmstadt, Planckstr. 1, 64291, Darmstadt, Germany.
i.hofmann@gsi.de

Prof. Dr. Jozef Lipka

Department of Nuclear Physics and Technology, Slovak
University of Technology, Bratislava, Ilkovicova 3, 812 19
Bratislava, Slovakia.
Lipka@elf.stuba.sk

Prof. Dr. Khalid Touqan

Chairman of Jordan Atomic Energy Commission, Amman,
Jordan.

Prof. Dr. Mark J. Hagmann

Desert Electronics Research Corporation, 762 Lacey Way, North
Salt Lake 84064, Utah, U. S. A.
MHagmann@NewPathResearch.Com

Prof. Dr. Nasr Zubeidey

President: Al-Zaytoonah University of Jordan, Amman, Jordan.
President@alzaytoonah.edu.jo

Prof. Dr. Patrick Roudeau

Laboratoire de l'Accelérateur, Lineaire (LAL), Universite Paris-
Sud 11, Batiment 200, 91898 Orsay Cedex, France.
roudeau@mail.cern.ch

Prof. Dr. Paul Chu

Department of Physics, University of Houston, Houston, Texas
77204-5005, U. S. A.
Ching-Wu.Chu@mail.uh.edu

Prof. Dr. Peter Dowben

Nebraska Center for Materials and Nanoscience, Department of
Physics and Astronomy, 255 Behlen Laboratory (10th and R
Streets), 116 Brace Lab., P. O. Box 880111, Lincoln, NE 68588-
0111, U. S. A.
pdowben@unl.edu

Prof. Dr. Peter Mulser

Institute fuer Physik, T.U. Darmstadt, Hochschulstr. 4a, 64289
Darmstadt, Germany.
Peter.mulser@physik.tu-darmstadt.de

Prof. Dr. Rasheed Azzm

Department of Electrical Engineering, University of New Orleans
New Orleans, Louisiana 70148, U. S. A.
razzam@uno.edu

Prof. Dr. Richard G. Forbes

University of Surrey, Advanced Technology Institute (BB),
School of Electronics and Physical Sciences, Guildford, Surrey
GU2 7XH, U. K.
R.Forbes@surrey.ac.uk

Prof. Dr. Roy Chantrell

Physics Department, York University, York, YO10 5DD, U. K.
Rc502@york.ac.uk

Prof. Dr. Shawqi Al-Dallal

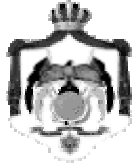
Department of Physics, Faculty of Science, University of Bahrain
Manamah, Kingdom of Bahrain.

Prof. Dr. Susamu Taketomi

Matsumoto Yushi-Seiyaku Co. Ltd., Shibukawa-Cho, Yao City,
Osaka 581-0075, Japan.
staketomi@hotmail.com

Prof. Dr. Wolfgang Nolting

Institute of Physics / Chair: Solid State Theory, Humboldt-
University at Berlin, Newtonstr. 15 D-12489 Berlin, Germany
Wolfgang.nolting@physik.hu-berlin.de



The Hashemite Kingdom of Jordan



Yarmouk University

Jordan Journal of
PHYSICS
An International Peer-Reviewed Research Journal

Volume 1, No. 1, June 2008, Jumada 1 1429 H

Instructions to Authors

Instructions to authors concerning manuscript organization and format apply to hardcopy submission by 1-mail, and also to electronic online submission via the Journal homepage website (<http://jjp.yu.edu.jo>).

Manuscript Submission

1- **Hardcopy:** The original and three copies of the manuscript, together with a covering letter from the corresponding author, should be submitted to the Editor-in-Chief:

Professor Ibrahim O. Abu Al-Jarayesh
Editor-in-Chief, Jordan Journal of Physics
Deanship of Scientific Research and Graduate Studies
Yarmouk University, Irbid, Jordan.
Tel: 00962-2-7211111, Ext. 3735
Fax: 00962-2-7211121
E-mail: jjp@yu.edu.jo

2- **Online:** Follow the instructions at the journal homepage website.

Original *Research Articles*, *Communications* and *Technical Notes* are subject to critical review by minimum of two competent referees. Authors are encouraged to suggest names of competent reviewers. *Feature Articles* in active Physics research fields, in which the author's own contribution and its relationship to other work in the field constitute the main body of the article, appear as a result of an invitation from the Editorial Board, and will be so designated. The author of a *Feature Article* will be asked to provide a clear, concise and critical status report of the field as an introduction to the article. *Review Articles* on active and rapidly changing Physics research fields will also be published. Authors of *Review Articles* are encouraged to submit two-page proposals to the Editor-in-Chief for approval. Manuscripts submitted in *Arabic* should be accompanied by an Abstract and Keywords in English.

Organization of the Manuscript

Manuscripts should be typed double spaced on one side of A4 sheets (21.6 x 27.9 cm) with 3.71 cm margins, using Microsoft Word 2000 or a later version thereof. The author should adhere to the following order of presentation: Article Title, Author(s), Full Address and E-mail, Abstract, PACS and Keywords, Main Text, Acknowledgment. Only the first letters of words in the Title, Headings and Subheadings are capitalized. Headings should be in **bold** while subheadings in *italic* fonts.

Title Page: Includes the title of the article, authors' first names, middle initials and surnames and affiliations.

The affiliation should comprise the department, institution (university or company), city, zip code and state and should be typed as a footnote to the author's name. The name and complete mailing address, telephone and fax numbers, and e-mail address of the author responsible for correspondence (designated with an asterisk) should also be included for official use. The title should be carefully, concisely and clearly constructed to highlight the emphasis and content of the manuscript, which is very important for information retrieval.

Abstract: A one paragraph abstract not exceeding 200 words is required, which should be arranged to highlight the purpose, methods used, results and major findings.

Keywords: A list of 4-6 keywords, which expresses the precise content of the manuscript for indexing purposes, should follow the abstract.

PACS: Authors should supply one or more relevant PACS-2006 classification codes, (available at <http://www.aip.org/pacs/pacs06/pacs06-toc.html>)

Introduction: Should present the purpose of the submitted work and its relationship to earlier work in the field, but it should not be an extensive review of the literature (e.g., should not exceed 1 ½ typed pages).

Experimental Methods: Should be sufficiently informative to allow competent reproduction of the experimental procedures presented; yet concise enough not to be repetitive of earlier published procedures.

Results: should present the results clearly and concisely.

Discussion: Should be concise and focus on the interpretation of the results.

Conclusion: Should be a brief account of the major findings of the study not exceeding one typed page.

Acknowledgments: Including those for grant and financial support if any, should be typed in one paragraph directly preceding the References.

References: References should be typed double spaced and numbered sequentially in the order in which they are cited in the text. References should be cited in the text by the appropriate Arabic numerals, which are superscripted while enclosed in square brackets. Titles of journals are abbreviated according to list of scientific periodicals. The style and punctuation should conform to the following examples:

1. Journal Article:

- a) Heisenberg, W., Z. Phys. 49 (1928) 619.
- b) Bednorz, J. G. and Müller, K. A., Z. Phys. B64 (1986) 189
- c) Bardeen, J., Cooper, L.N. and Schrieffer, J. R., Phys. Rev. 106 (1957) 162.
- d) Asad, J. H., Hijawi, R. S., Sakaji, A. and Khalifeh, J. M., Int. J. Theor. Phys. 44(4) (2005), 3977.

2. Books with Authors, but no Editors:

- a) Kittel, C., "Introduction to Solid State Physics", 8th Ed. (John Wiley and Sons, New York, 2005), chapter 16.
- b) Chikazumi, S., C. D. Graham, JR, "Physics of Ferromagnetism", 2nd Ed. (Oxford University Press, Oxford, 1997).

3. Books with Authors and Editors:

- a) Allen, P. B. "Dynamical Properties of Solids", Ed. (1), G. K. Horton and A. A. Maradudin (North-Holland, Amsterdam, 1980), p137.
- b) Chantrell, R. W. and O'Grady, K., "Magnetic Properties of Fine Particles" Eds. J. L. Dormann and D. Fiorani (North-Holland, Amsterdam, 1992), p103.

4. Technical Report:

Purcell, J. "The Superconducting Magnet System for the 12-Foot Bubble Chamber", report ANL/HEP6813, Argonne Natl. Lab., Argonne, Ill, (1968).

5. Patent:

Bigham, C. B., Schneider, H. R., US patent 3 925 676 (1975).

6. Thesis:

Mahmood, S. H., Ph.D. Thesis, Michigan State University, (1986), USA (Unpublished).

7. Conference or Symposium Proceedings:

Blandin, A. and Lederer, P. Proc. Intern. Conf. on Magnetism, Nottingham (1964), P.71.

8. Internet Source:

Should include authors' names (if any), title, internet website, URL, and date of access.

9. Prepublication online articles (already accepted for publication):

Should include authors' names (if any), title of digital database, database website, URL, and date of access.

For other types of referenced works, provide sufficient information to enable readers to access them.

Tables: Tables should be numbered with Arabic numerals and referred to by number in the Text (e.g., Table 1). Each table should be typed on a separate page with the legend above the table, while explanatory footnotes, which are indicated by superscript lowercase letters, should be typed below the table.

Illustrations: Figures, drawings, diagrams, charts and photographs are to be numbered in a consecutive series of Arabic numerals in the order in which they are cited in the text. Computer-generated illustrations and good-quality digital photographic prints are accepted. They should be black and white originals (not photocopies) provided on separate pages and identified with their corresponding numbers. Actual size graphics should be provided, which need no further manipulation, with lettering (Arial or Helvetica) not smaller than 8 points, lines no thinner than 0.5 point, and each of uniform density. All colors should be removed from graphics except for those graphics to be considered for publication in color. If graphics are to be submitted digitally, they should conform to the following minimum resolution requirements: 1200 dpi for black and white line art, 600 dpi for grayscale art, and 300 dpi for color art. All graphic files must be saved as TIFF images, and all illustrations must be submitted in the actual size at which they should appear in the journal. Note that good quality hardcopy original illustrations are required for both online and mail submissions of manuscripts.

Text Footnotes: The use of text footnotes is to be avoided. When their use is absolutely necessary, they should be typed at the bottom of the page to which they refer, and should be cited in the text by a superscript asterisk or multiples thereof. Place a line above the footnote, so that it is set off from the text.

Supplementary Material: Authors are encouraged to provide all supplementary materials that may facilitate the review process, including any detailed mathematical derivations that may not appear in whole in the manuscript.

Revised Manuscript and Computer Disks

Following the acceptance of a manuscript for publication and the incorporation of all required revisions, authors should submit an original and one more copy of the final disk containing the complete manuscript typed double spaced in Microsoft Word for Windows 2000 or a later version thereof. All graphic files must be saved as PDF, JPG, or TIFF images.

Allen, P.B., ".....", in: Horton, G.K., and Muradudin, A. A., (eds.), "Dynamical.....", (North.....), pp....

Reprints

Twenty (20) reprints free of charge are provided to the corresponding author. For orders of more reprints, a reprint order form and prices will be sent with the article proofs, which should be returned directly to the Editor for processing.

Copyright

Submission is an admission by the authors that the manuscript has neither been previously published nor is being considered for publication elsewhere. A statement transferring copyright from the authors to Yarmouk University is required before the manuscript can be accepted for publication. The necessary form for such transfer is supplied by the Editor-in-Chief. Reproduction of any part of the contents of a published work is forbidden without a written permission by the Editor-in-Chief.

Disclaimer

Opinions expressed in this Journal are those of the authors and neither necessarily reflects the opinions of the Editorial Board or the University, nor the policy of the Higher Scientific Research Committee or the Ministry of Higher Education and Scientific Research. The publisher shoulders no responsibility or liability whatsoever for the use or misuse of the information published by JJP.

Indexing

JJP is currently applying for indexing and abstracting to all related International Services.

Jordan Journal of
P H Y S I C S

An International Peer-Reviewed Research Journal

Volume 1, No. 1, June 2008, Jumada 1 1429 H

Table of Contents:

Articles	Pages
Time-Dependent Response of Field Emission by Single Carbon Nanotubes M. J. Hagmann and M. S. Mousa	1-8
Spectra of Electromagnetic Surface Waves on Plasma–Vacuum Interface Inside a Metallic Cylindrical Pipe W. M. Daqa, A. Al-Khateeb, A. I. Al-Sharif and N. M. Laham	9-17
Optical Characteristics of Amorphous Tin Nitride Thin Films Prepared by Ion Beam Assisted DC Magnetron Reactive Sputtering I. M. Odeh	19-29
Magnetization Measurements on “as Prepared” and Annealed $\text{Fe}_{3-x}\text{Mn}_x\text{Si}$ Alloys M. S. Lataifeh, M. O’Shea, A. S. Saleh and S. H. Mahmood	31-36
Magnetic and Structural Studies of $\text{Ba}_{0.5}\text{Sr}_{0.5}(\text{ZnTi})_x\text{Fe}_{12-2x}\text{O}_{19}$ Prepared by Ball Milling A. González-Angeles, A. Grusková, J. Lipka, J. Sláma and V. Jančárik	37-42
Partial Substitution Effects on the Structure and Electrical Properties of the High Temperature Superconducting System $\text{Bi}_{2-x}\text{Tl}_x\text{Ba}_{2-y}\text{Sr}_y\text{Ca}_2\text{Cu}_3\text{O}_{10+\delta}$ A. El Ali (Al-Dairy), A. D. Alazawi, Y. A. Hamam and K. Khasawinah	43-52
Modeling Atmospheric Turbidity at Zarqa Area Using Meteorological Data S. Hamasha, M. Abu-Allaban and A. Abulaban	53-60

Time-Dependent Response of Field Emission by Single Carbon Nanotubes

M. J. Hagmann^a and M. S. Mousa^b

^a *New Path Research, Salt Lake City, Utah 84110, USA.*

^b *Department of Physics, Mu'tah University, Al-Karak, Jordan.*

Received on: 9/5/2007; Accepted on: 8/5/2008

Abstract: Four field emission tubes that have single carbon nanotubes (CNT) as the emitters were tested; two with single-walled CNT and two with multiwalled CNT. A tube with a tungsten tip was used for comparison. Fowler-Nordheim analysis of the DC current-voltage data gave reasonable values for the local fields at the emitters and the sizes of the emitters. Two oscillators were used to superimpose sinusoidal signals on the applied static field, thus increasing the DC emitted current and causing a mixer current at their difference frequency, in agreement with theory. Square-wave pulses from a single laser diode (20 mW, 658 nm) focused on each emitter increased the emitted current by 5.2% with the CNT and 0.19% with the tungsten tip.

Keywords: Field Emission, Carbon Nanotubes, Fowler-Nordheim analysis.

Introduction

Simulations and preliminary experiments show that photomixing (optical heterodyning) in laser-assisted field emission could be used as a new microwave or terahertz (THz) source, with a multi-octave bandwidth [1]. The field emitter tip is much smaller than the wavelength of the incident optical radiation so quasi-static conditions require that the electric field of the radiation is superimposed on the applied static field to modulate the height of the barrier. Electrons tunnel from the tip into vacuum with a delay τ of less than 2 fs [2]. Thus, because the current-voltage characteristics of field emission are extremely nonlinear, if two lasers are focused on the tip, the mixer current would follow each cycle of the difference frequency of the two lasers from DC up to 500 THz ($1/\tau$). The tip will withstand applied static fields as high as 9 V/nm [3], so that incident laser radiation with comparable field strengths could produce a bright source of microwave or THz radiation.

Carbon nanotubes (CNT) are excellent field emitters and facilitate the

miniaturization of electron devices [4]. Furthermore, the kinetic inductance of CNT causes them to be high impedance (~ 5 k Ω) transmission lines [5, 6], and we have shown that this effect can be used for efficient broadband matching to the high impedance that is inherent in field emission [7]. We will describe the static and dynamic characterization of field emitters consisting of single CNT, both single-walled (SWCNT) and multiwalled (MWCNT), and compare them to a field emitter consisting of an etched single crystal of tungsten. We acknowledge that some of this information was first presented in a paper at an international conference [8].

Description and Static Characterization of the Field Emitters

Four field emission tubes, as shown in Fig. 1, were made for us by Xintek (Chapel Hill, NC). The copper anode is at the right, and the CNT emitter is mounted on a tungsten wire attached to the copper cylinder at the left. Fig. 2 shows images of the CNT emitters for each tube, taken with a

JEOL model JEM 6300 SEM. Tubes M-1 and M-4 have a single MWCNT as the emitter, and tubes C-3 and C-6 have a single SWCNT as the emitter. The CNT are in bundles that have diameters of 10 to 30 nm, but in each tube the field emission is from the one CNT at the end of the bundle where the electric field is most intense. The dimensions of the individual CNT were not determined.



Fig. 1: Appearance of the field emission tubes made for us by Xintek.

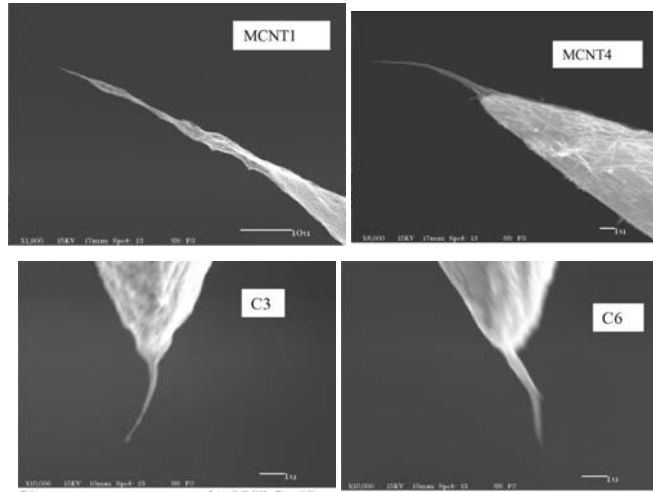


Fig. 2: SEM images of the CNT emitters in the 4 tubes.

The DC current-voltage characteristics were measured for these four tubes, as well as a field emitter tube from Leybold Didactic (Klinger, College Point, NY), which has an etched single crystal of tungsten as the emitter. All of the measurements that were made with the 5 tubes were performed at room temperature. The tungsten tip is mounted on a filament so that this tip is heated for cleaning shortly before each session of measurements. However, it is not possible to clean the CNT, which probably causes the “switch-on” effect—the supply voltage must be momentarily increased well beyond the operating point to initiate field emission with the CNT [9].

The data from the DC measurements were reduced by a Fowler-Nordheim analysis based on the following simplified form of the Fowler-Nordheim equation that gives the magnitude of the current density as a function of the applied static field for field emission from a specific material [10-12]:

$$J = A E^2 \exp(-B/E) \quad (1)$$

Here J and E are the magnitudes of the

current density and the electric field intensity, $A = 1.541 \times 10^{-6}/\Phi$, and $B = 6.831 \times 10^9 \Phi^{3/2}$. The work function $\Phi = 4.5$ eV for tungsten, and for the CNT we set $\Phi = 4.9$ eV for graphene. In order to apply the Fowler-Nordheim equation to the DC current-voltage data, we also use the following equation which is valid for a given tube, where I is the field emission current and V is the potential applied between the anode and cathode:

$$I = CV^2 \exp(-D/V) \quad (2)$$

Equations (1) and (2) may be combined to obtain the following expressions for the parameters S and R , which are used to characterize the field emitters:

$$S = CD^2/AB^2 \quad (3)$$

$$R \equiv V/E = D/B \quad (4)$$

Here S is referred to as the effective emitting area, which would be the physical area of the emitter if the current density were uniform over a fixed area and zero elsewhere. The parameter R is referred to as the effective radius of curvature of the emitter, but it also includes the effects of

local intensification of the electric field caused by elongation of the emitter or the reduction of the field which may be caused by shielding due to adjacent structures.

Fowler-Nordheim plots of the DC current-voltage data were made using $\ln(I/V^2)$ as the ordinate and $1/V$ as the abscissa. Equation (2) requires that these plots should be straight lines, and typically the correlation $R \approx -0.998$. Linear regressions based on these Fowler-Nordheim plots typically have a standard variance $\sigma \approx 0.08$, and the probability for the null-hypothesis, that no linear relationship exists, is less than 0.0001. Values of the parameters C, D, S, and R were determined from the linear regressions.

A series ballast resistor of 100 M Ω was typically used in the measurements. However, when the series ballast resistor was increased to 2.575 G Ω with tube C-6

the data were not consistent with the Fowler-Nordheim equation ($R = -0.846$, $\sigma = 0.738$) even though the emitted current was stable at each value of the applied static potential. Fig. 3 shows the anomalous data which were obtained using the 2.575 G Ω ballast resistor. In order to explain this effect, we hypothesize that for currents greater than 500 nA, field emission with a single CNT may be intermittent, fluctuating at a high frequency. Thus, the average current, as measured by our DC microammeter, may be much greater with a large ballast resistor. This is because at those times when the current is momentarily low, the voltage drop across the ballast resistor is at a minimum so an unusually high voltage is across the tube, and this voltage causes a short-duration surge in the current.

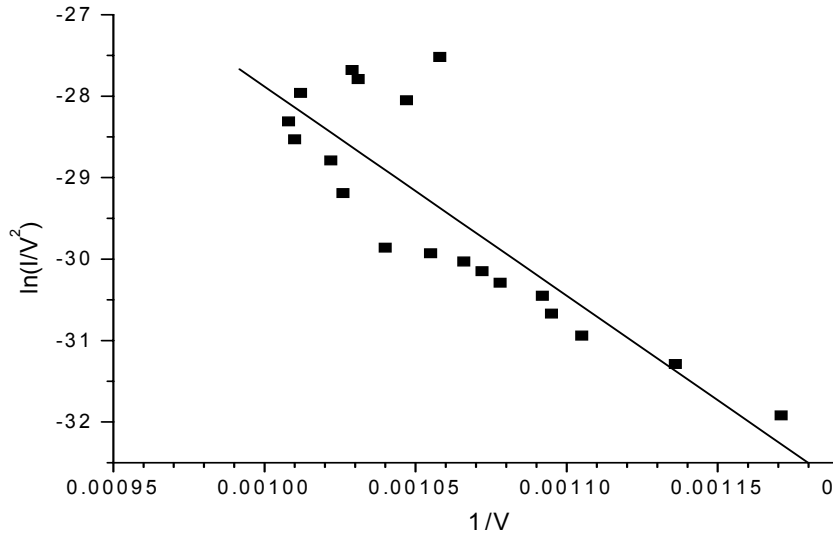


Fig. 3: Fowler-Nordheim plot for tube C-6 with a 2.575 G Ω ballast resistor.

Others have also observed instabilities in the field emission from single CNT [13-15]. However, they did not describe the bias circuits which they used so it is not possible to determine if these instabilities were exacerbated by increasing the ballast resistor. Data which are consistent with the Fowler-Nordheim equation were obtained with tube C-6 when the ballast resistor was decreased to values including 100 M Ω or 595 M Ω .

Values of the parameter R, the effective radius of curvature of the emitter, were found to vary from 77 to 110 nm for the 4 tubes with CNT emitters. This suggests that values of the local electric field at the emitting sites were as high as 14 V/nm in some of these measurements. Others studying field emission from CNT have given

approximate values for the electric field by dividing the applied voltage by the distance between the anode and the emitting tip, noting that this field would be intensified by the shape of the CNT but not estimating the local electric field at the emitting sites—which would have permitted comparison with our values [4].

The Fowler-Nordheim analysis gave a value of 91 nm for the effective radius of curvature of the emitter in the Leybold tube, suggesting that the local electric field was as high as 5 V/nm in some of our measurements. Current densities as high as 10^9 and 10^{12} A/m² may be drawn from a tungsten emitter in steady-state and pulsed operation, respectively [12], and the corresponding values of the applied static field are 4.7 and 8.6 V/nm [3] which may be

considered as limiting field strengths for tungsten under these conditions. Thus, the value of the parameter R which we obtained for the Leybold tube appears to be reasonable.

The Fowler-Nordheim analysis also showed that the parameter S , the effective emitting area, varied from 81 to 230 nm² for the 4 tubes with CNT emitters. If the current density were uniform, this would correspond to circular emitting spots having radii of approximately 5 to 9 nm. Others have recently used Lorenz microscopy to directly observe the emitting sites for field emission from MWCNT, and they find one or more sites having radii of several nm [16]. Their data are in reasonable agreement with our results. The Fowler-Nordheim analysis also shows that the effective emitting area for the tungsten tip in the Leybold tube would correspond to a hemisphere with a radius of 290 nm. This result and the value of 91 nm for the effective radius of curvature of the emitter in the Leybold tube are in reasonable agreement with the radius of 100 to 200 nm which is specified by Leybold.

Measurement of Mixing at Audio Frequencies

We have made rigorous quantum simulations of laser-assisted field emission [17] which show that the radiation from 2 lasers increases the DC current (optical rectification) and also causes harmonics and mixing terms with frequencies $n_1f_1 + n_2f_2$, where f_1 and f_2 are the frequencies of the lasers and the integers n_1 and n_2 may be positive, zero, or negative. However, the high-frequency terms are not seen in measurements of the current that passes through a field emission tube because the tube itself acts as a low-pass filter [18]. We have made antennas and transmission lines on field emitters to couple microwave output power at the difference frequency ($f_1 - f_2$) [1, 19], but these techniques were not implemented in the 5 tubes for this project. Instead, we determined the spectrum of the

field emission current when transformers were used to superimpose low-frequency voltages on the applied static field, with $f_1 = 1.67$ kHz and $f_2 = 1.10$ kHz. These frequencies were chosen because they are low enough that the effects of the capacitances and inductances within the tubes may be neglected [18].

To aid in understanding these phenomena, closed-form expressions for the components of the field emission current may be obtained by using time-dependent perturbation with the Fowler-Nordheim equation. This method requires the adiabatic approximation that the frequencies of the oscillatory fields are low enough that the effects of the photon energy may be neglected [1]. Thus, closed-form expressions may be determined for all of the components of the current which are found in the rigorous quantum simulations [17]. However, with laser radiation it is necessary to multiply each term by the gain that is caused by a resonance in the interaction of the tunneling electrons and the radiation field [20-23].

Consider two sinusoidal voltages superimposed on the applied static potential V_0 , so that

$$V = V_0 + V_1 \cos(\omega_1 t) + V_2 \cos(\omega_2 t) \quad (5)$$

If V_1 and V_2 are much less than V_0 and the parameter D in Eq. (2), and the frequencies ω_1 , ω_2 , are low enough that the effects of the photon energy may be neglected, then a second order Taylor series expansion of Eq. (2) about the operating point (V_0, I_0) , where there is only the applied static potential V_0 and the DC current I_0 , gives the following expression for the total current:

$$I = I_0 + I_\Delta + I_{F1} + I_{F2} + I_{H1} + I_{H2} + I_S + I_D \quad (6)$$

The step increase of the DC current, the two fundamental terms, the two second harmonic terms, and the sum and difference terms are given by:

$$I_\Delta = I_0(D^2/4V_0^2)[(V_1/V_0)^2 + (V_2/V_0)^2][1 + 2V_0/D + 2V_0^2/D^2] \quad (7A)$$

$$I_{F1} = I_0(D/V_0)(V_1/V_0)[1 + 2V_0/D] \cos(\omega_1 t) \quad (7B)$$

$$I_{F2} = I_0(D/V_0)(V_2/V_0)[1 + 2V_0/D] \cos(\omega_2 t) \quad (7C)$$

$$I_{H1} = I_0(D^2/4V_0^2)(V_1/V_0)^2[1 + 2V_0/D + 2V_0^2/D^2] \cos(2\omega_1 t) \quad (7D)$$

$$I_{H2} = I_0(D^2/4V_0^2)(V_2/V_0)^2[1 + 2V_0/D + 2V_0^2/D^2] \cos(2\omega_2 t) \quad (7E)$$

$$I_S = I_0(D^2/2V_0^2)(V_1/V_0)(V_2/V_0)[1 + 2V_0/D + 2V_0^2/D^2] \cos[(\omega_1 + \omega_2)t] \quad (7F)$$

$$I_D = I_0(D^2/2V_0^2)(V_1/V_0)(V_2/V_0)[1 + 2V_0/D + 2V_0^2/D^2] \cos[(\omega_1 - \omega_2)t] \quad (7G)$$

Transformers were used to couple 2 floating battery-operated Wien bridge oscillators in series with the high-voltage anode circuit of each of the 5 field emission tubes in order to superimpose low-frequency sinusoidal signals on the applied static field. The oscillators provided the high voltages $V_1=V_2=120$ V which are required to cause a measurable effect on the current. The full series loop of the electrical circuit included the high-voltage power supply, a 100 M Ω ballast resistor, the secondary windings of the transformers for the oscillators, the field emission tube, a DC microammeter, and a 1 M Ω resistor to ground which was a shunt for the digital oscilloscope.

Capacitive shunts were used to eliminate the effects of the high-voltage power supply, the ballast resistor, and the DC microammeter on the currents at the 6 frequencies. Thus, the DC equivalent circuit consists of the high-voltage power supply, a resistance of 101 M Ω , the tube modeled by the two current sources I_0 and I_Δ in parallel, and the DC microammeter. The equivalent circuit at each of the 6 frequencies consists of the tube modeled by the respective current source, in series with the parallel combination of the 1 M Ω resistor and the digital oscilloscope.

The 2 oscillators were set to the frequencies $f_1 = 1.67$ kHz and $f_2 = 1.10$ kHz, and we determined the step increase in the DC current as well as the components of the current at the 6 frequencies f_1 , f_2 , $2f_1$, $2f_2$, $f_1 + f_2$, and $f_1 - f_2$. These frequencies correspond to 1.67, 1.10, 3.34, 2.20, 2.77 and 0.57 kHz, respectively. Each of the measured currents were compared with values calculated using the respective equivalent circuit with the expressions in Eqs. (7A-7G).

With the Leybold tube we found that the currents at the fundamental frequencies f_1 and f_2 were each within 5% of the predicted values, and the step increase in the DC current and the currents at each of the other 4 frequencies were each within 10% of the predicted values. The measured increase in the DC current, and the currents at the 6 frequencies, were each between 1 and 2 times the predicted values for tubes M-4 and C-6, and between 3 and 4 times the

predicted values for tube M-1. In this series of measurements tube C-3 was too unstable to permit measuring any of the currents at the 6 frequencies. As it was noted earlier, it is not possible to clean the CNT, and this causes the values of the parameter D in Eqs. (7A-7G) to be less reproducible for the CNT than it is for the Leybold tube. We attribute the greater errors in the measurements with the CNT to this effect.

Measurement of the Change in the DC Current Caused by a Laser

While there is no means to couple microwave or THz power from any of these 5 tubes, we did measure the step increase in the DC current that is caused by focusing a single square-wave modulated laser diode (20 mW, 658 nm) on the field emission tip. The laser diode was maximally-focused to provide a measured Gaussian profile with a power flux density of approximately 10^7 W/m² at the tip. Equations (7A) and (7G) show that this measured current step is equal to one-half of the peak value of the mixer current that would be generated if two stabilized tunable lasers each provided the same power flux density. Thus, this low-frequency measurement may be used to estimate the mixer current which could be obtained by photomixing with these same field emitters.

The laser diode was amplitude-modulated with a square-wave envelope and the field emission current was measured with a digital oscilloscope as shown in the diagram of Fig. 4. It was noted earlier that the field emission tube itself acts as a low-pass filter. Equation (7A) shows that the increase in the field emission current, I_Δ , acts as a current source, and it is easily shown that when a square-wave current source is fed to a parallel R-C circuit, the voltage across the resistor has a saw-tooth waveform with a peak-to-peak value that is given by

$$V_{pp} = R I_\Delta (1 - e^{-1/2\tau f}) / (1 + e^{-1/2\tau f}) \quad (8)$$

where I_Δ is the peak-to-peak value of the current waveform and $\tau \equiv RC$. Equation (8) shows that $V_{pp0} \equiv V_{pp}(f = 0) = R I_\Delta$, and $V_{pp} = R I_\Delta / 4\tau f = V_{pp0} / 4\tau f$ for $f \gg 1/\tau$.

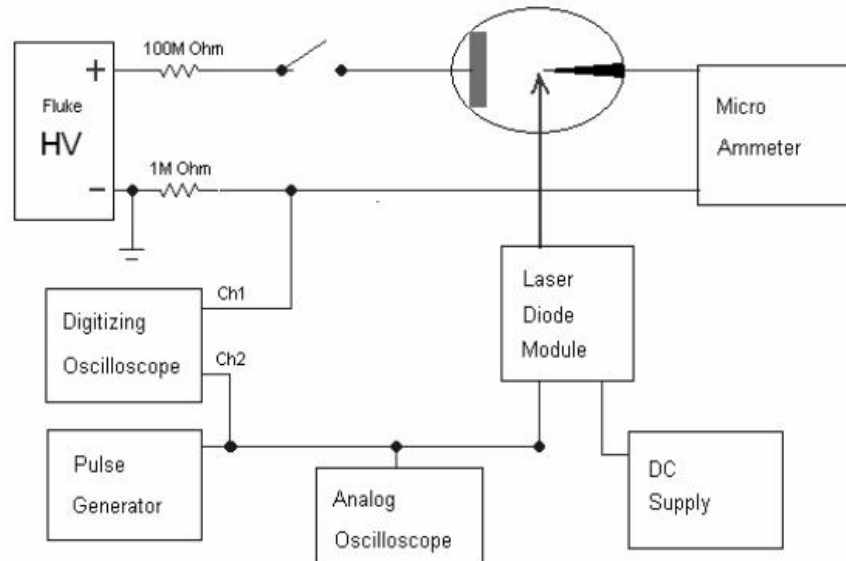


Fig. 4: Experimental configuration for measurements with a square-wave modulated laser diode.

The peak-to-peak value of the voltage across the resistor was measured as a function of the modulation frequency for each of the tubes. A DC current of $1 \mu\text{A}$ was used with each of the 4 CNT tubes, and $8 \mu\text{A}$ was used with the Leybold tube. However, tube C-6 could not be used in this test because ripples in the glass envelope interfered with focusing of the laser on the tip. Least-square regression was used to determine the values of I_{Δ} and τ from these data.

Table I shows the parameters that were measured with calculated characteristics of the tubes, and Fig. 5 shows the measured value of the apparent peak-to-peak amplitude of the field emission current as a function of the modulation frequency for tube

M-4. This figure shows the inverse behavior which is predicted at frequencies which are much greater than $1/\tau$. From Table I, the actual value of I_{Δ} for tube M-4 is 83 pA , which is seen in the data that were taken for much lower modulation frequencies. Table I also shows that the mean increase in the DC current is 6.2% for the 3 tubes with CNT, as compared with 0.20% for the Leybold tube. This suggests that if two stabilized tunable lasers each provided the same power flux density, the peak value of the mixer current, occurring at the difference frequency ($f_1 - f_2$), would be an average of 12% of the DC current for the tubes with CNT, as compared with 0.40% for the Leybold tube.

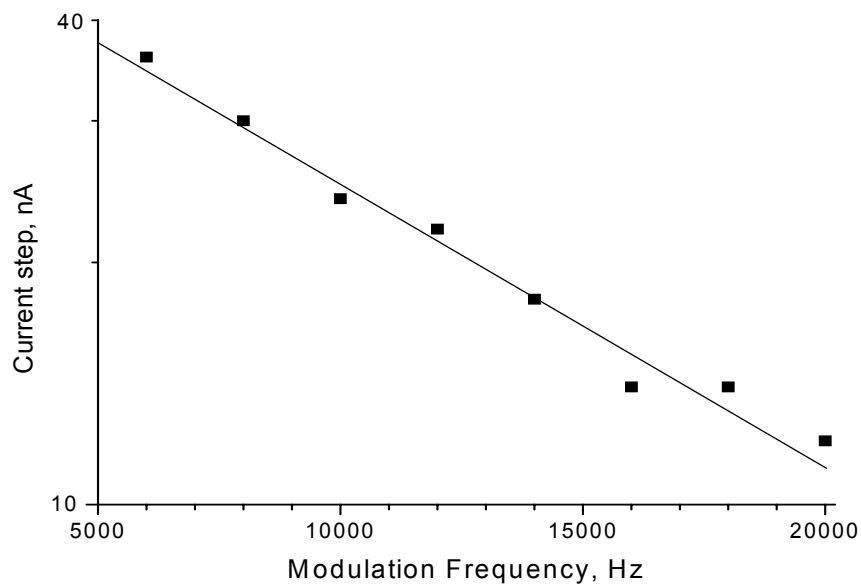


Fig. 5: Step in current caused by the laser vs. modulation frequency for tube M-4.

Table I: Measured and calculated parameters for the step-increase in the DC current caused by a laser

Tube	M-1	M-4	C-3	Leybold
I_0 , the DC current, μA	1.0	1.0	1.0	8.0
DC voltage across tube, V	980	840	920	4600
R, k Ω	500	500	500	1000
T, μs	110	80	86	510
C, pF	220	160	170	510
I_{Δ} , pA	56	83	48	16
I_{Δ}/I_0 , %	5.6	8.3	4.8	0.20

Discussion and Conclusions

Four field emission tubes having single CNT as the emitters were tested, and a tube having a tungsten tip was used for comparison. Fowler-Nordheim analysis of the DC current-voltage data gave reasonable values for the local fields at the emitters and the sizes of the emitter sites. Also, two audio-frequency oscillators superimposed sinusoidal signals on the applied static field, thus increasing the DC emitted current and causing components of the current at the two fundamental frequencies, the second harmonics, and the sum and difference frequencies, which are in reasonable agreement with theory. A single square-wave modulated laser diode (20 mW, 658 nm) focused on each emitter, increased the emitted current by an average of 6.2 % during each laser pulse with the CNT and 0.20 % with the tungsten tip.

We have previously made tubes in which antennas and transmission lines couple the microwave power that is generated by photomixing in laser-assisted field emission to an external load, and these tubes have used emitters of tungsten and molybdenum [1, 18]. The present measurements made with the CNT suggest that the mixer current could be 30 times greater if either SWCNT or MWCNT were used in place of the metal emitters, which would increase the microwave output power by 30 dB as a considerable improvement.

Twenty years ago there was considerable controversy regarding the mechanism by which laser radiation increases field emission current. For example, it was observed that when the laser beam is turned on the field emission current increases with a characteristic time that is similar to the calculated thermal relaxation time of the field emitter, so this effect could be thermal [24]. However, we have shown that the slow rise time for the current in such experiments is due to circuit effects, such as that which is described in relation to Eq. (8) of the present paper [25]. Recently, others have generated electron pulses with durations of under 70 fs by irradiating a field emitter with a low-power femtosecond laser [26]. They have shown that this effect is non-thermal; the operating parameters may cause either photofield emission or optical field emission to be dominant. More pertinently, others have used laser radiation to increase the field emission current from a cathode with a dense field of CNT by a factor of 18, and they have shown that this is not a thermal effect by comparing their data with the effect of elevated temperatures on the field emission from CNT [27].

Acknowledgment

This work was supported by the National Science Foundation under Grant No. DMI-0338928.

References

1. M. J. Hagmann. (2003). Appl. Phys. Lett. 83, 1.
2. M. J. Hagmann. (1998). Int. J. Quant. Chem. 70, 703.
3. M. J. Hagmann. (1999). Ultramicroscopy 79, 115.
4. A. N. Obraztsov, I. Paviovsky, A. P. Volkov, E. D. Obraztsova, A. L. Chuvilin and V. L. Kuznetsov. (2000). J. Vac. Sci. Technol. B, 18, 1059.
5. P. J. Burke. (2002). IEEE Trans. Nanotechnology, 1, 129.
6. R. Tarkiainen, M. Ahlskog, J. Penttila, L. Roschier, P. Hakonen, M. Paalanen and E. Sonin. (2001). Phys. Rev. B 64, 195412.
7. M. J. Hagmann. (1995). IEEE Trans. Nanotechnology 4, 289.
8. M. J. Hagmann and M. S. Mousa. (2006). Technical Digest, Vacuum Nanoelectronics Conference 2006 and International Field Emission Symposium (IVNC/IFES) pp. 201-202.
9. Y. Liu and S. Fan. (2005). Solid State Commun. 133, 131.
10. R.H. Fowler and L. W. Nordheim. (1928). Proc. R. Soc. Lond. A, Math. Phys. Sci. 119, 173.
11. L.W. Nordheim. (1928). Proc. R. Soc. Lond. A, Math Phys. Sci. 121, 626.
12. R. Gomer. (1993). *Field Emission and Field Ionization* (American Institute of Physics, New York).
13. J.-M. Bonard, K. A. Dean, B. F. Coll and C. Klinke. (2002). Phys. Rev. Lett. 89, 197602.
14. K. A. Dean and B. R. Chalamala. (2000). Appl. Phys. Lett. 76, 375.
15. J.-M. Bonard, J.-P. Salvetat, T. Stöckli, L. Forró and A. Châtelain. (1999). Appl. Phys. A 69, 245.
16. T. Fujieda, K. Hidaka, M. Hayashibara, T. Kamino, Y. Ose, H. Abe, T. Shimizu and H. Tokumoto. (2005). Jpn. J. Appl. Phys. 44, 1661.
17. M. J. Hagmann. (1999). Int. J. Quant. Chem. 75, 417.
18. M. J. Hagmann, M. S. Mousa, M. Brugat, E. P. Sheshin and A. S. Baturin. (2004). Surf. Interface Anal. 36, 402.
19. K. Alonso and M. J. Hagmann. (2001). J. Vac. Sci. Technol. B 19, 68.
20. M. J. Hagmann. (1995). J. Appl. Phys. 78, 25.
21. A. Mayer and J.-P. Vigneron. (2000). Phys. Rev. B. 62, 16138.
22. A. Mayer, N. M. Miskovsky and P. H. Cutler. (2002). Phys. Rev. B 65, 195416.
23. A. Mayer, N. M. Miskovsky and P. H. Cutler. (2003). J. Vac. Sci. Technol. B 21, 395.
24. M. J. G. Lee and E. S. Robins. (1989). J. Appl. Phys. 65, 1699.
25. M. Brugat, M. S. Mousa, E. P. Sheshin and M. J. Hagmann. (2002). Mater. Sci. Eng. A. 327, 7.
26. P. Hommelhoff, Y. Sortais, A. Anghajani-Talesh and M. A. Kasevich. (2006). Phys. Rev. Lett. 96, 077401.
27. H.-F. Cheng, Y.-S. Hsieh, Y.-C. Chen and I.-N. Lin. (2004). Diam. Relat. Mater. 13, 1004.

Spectra of Electromagnetic Surface Waves on Plasma–Vacuum Interface Inside a Metallic Cylindrical Pipe

W. M. Daqa, A. Al–Khateeb, A. I. Al–Sharif and N. M. Laham

Department of Physics, Faculty of Science, Yarmouk University, Irbid, Jordan

Received on: 28/5/2007; Accepted on: 17/2/2008

Abstract: A general nonlinear dispersion relation, for the spectra of electromagnetic surface waves on the interface separating an axially symmetric plasma and vacuum both enclosed in a resistive cylindrical pipe, have been derived and various limiting cases were discussed. The spectra were found to be similar to those of electrostatic surface wave modes existing at plasma–vacuum interface for cases such as thin plasma or a conducting wall far away from the plasma–vacuum interface. For moderate values of ka , where k is the wave number and a is the width of plasma, appreciable modifications of spectral curves have been observed. By including the surface impedance Z_m of the pipe–wall, the dispersion relation of the electromagnetic surface waves becomes a function of the dispersive properties of the wall. Investigating the surface impedance shows no observable effect on the real part of the surface wave spectra, but it introduces an imaginary part into the frequency ω . The corresponding peak values have been obtained for various representative situations. When coupled to an external driver such as particle beams, surface wave fields can be excited, causing beam energy losses, and thus affecting the beam dynamics

Key Words: Electromagnetic Surface Waves, Surface Waves In Plasmas, Resistive Cylindrical Pipe.

Introduction

Surface waves (SW's) are proper modes propagating along the interface between two media, and are characterized by having fields concentrated near the boundary interfaces. In order for a surface wave to exist, the corresponding wave fields must be evanescent in both regions. The presence of the bounding walls can alter the plasma behavior and then the spectra of waves and oscillations existing in such plasmas. Surface waves are of importance in laser –produced–plasmas fusion research [1, 2] and in all industrial applications of guided–wave–produced plasmas [3]. These plasmas can be sharply bounded, inhomogeneous, and anisotropic so that they are capable of supporting surface waves [4].

Being periodic surface charges at boundary interfaces, amplitudes of the fields associated with SW's reach their maximum

values at the bounding surfaces and decay in both media by moving far away from the interface [5, 3, 6]. Study of electrostatic surface waves (ESW) on cylindrical cold plasmas was first carried out by Trivelpiece and Gould [7]. For semi–infinite plasma with planar vacuum boundary, surface waves exist with spectra ranging from $\omega = \omega_p / \sqrt{2}$ for plasma–vacuum interface, and $\omega = \omega_p / \sqrt{1 + \epsilon_d}$ for plasma–dielectric interface, down to $\omega = 0$, where ω_p is the bulk plasma frequency, $\epsilon_p = 1 - \omega_p^2 / \omega^2$ is the cold plasma dielectric constant, $\epsilon_d = \epsilon_d / \epsilon_0$ is the relative dielectric constant of bounding dielectric, and ϵ_0 is the permittivity of free space.

By adopting a plasma kinetic approach,

Guernsey investigated the effects of thermal motion on the ESW spectra [8]. It has been found that ESW are more strongly Landau damped than the corresponding bulk mode. For sufficiently large k values, thermal effects may be modeled by replacing the cold plasma dielectric constant by $\varepsilon_p = 1 - (\omega_p^2 + \gamma_e v_{th}^2 k^2) / \omega^2$, where γ_e is the ratio of specific heats for electrons and v_{th} is their average thermal speed. Exact treatment of surface waves shows that $\gamma_e = 3$ corresponds to the wave spectra correction when fluid theory is used for semi-infinite plasma [8]. It has been shown in previous studies that the effect of electron thermal motion becomes important only in the quasi-static limit of small phase velocities of surface waves compared to the speed of light [9].

Electromagnetic treatment of surface waves in plasmas showed that SW's are neither pure longitudinal nor pure transverse [10, 11, 12]. Since perturbations in wave fields are both longitudinal and transverse, surface modes are hybrid modes. Generally, they are mixture of both longitudinal space charge and transverse electromagnetic waves, and only in the frequency domain such that $\varepsilon(\omega) \omega / c \ll k$ where c is the speed of light, the magnetic field component of the wave field in a given medium can be neglected. This corresponds to the electrostatic limit in which SW's may be treated as potential waves [7, 13, 14].

In the absence of a steady magnetic field there is no interior space charge bunching and the waves are surface waves. For a homogeneous plasma filling a conducting tube and in the presence of an axial dc magnetic field, the cases of strong and weak magnetic fields $\omega_c > \omega_p$, where ω_c is the gyro-frequency, and $\omega_p > \omega_c$ result in two propagating and two non-propagating (evanescent) bands corresponding to real and imaginary propagation constants, respectively [7, 15]. For a cold plasma partially filling the conducting tube, and as the magnetic field is reduced to zero, only one circularly symmetric mode propagating at low frequency will survive with asymptotic frequency $\omega = \omega_p / \sqrt{1 + \varepsilon_d}$ for short wavelengths.

Theoretical studies of surface waves in the presence of plasmas with sharp boundaries, neglecting transition layers with smooth density increase existing near the boundary, are valid to first approximation and can explain most properties of surface waves, as long as wavelengths of interest are much larger than the width of the transition layer [16]. Effects of gradients in plasma density, contrary to thermal and collisional effects which broaden the frequency domain of the surface waves, can lead to a significant modification of the dispersion curve of SW's by forming a maximum in the dispersion curves and shifting it down to lower values [3, 10, 16].

In the present article, we investigate the spectra of electromagnetic surface waves (EMSW's) at the surface of cold, unmagnetized and uniform plasma of finite width in the presence of a finite resistive wall of a cylindrical waveguide. In Sec.2, we derive the EMSW dispersion relation as a function of the dispersive properties of the pipe-wall and discuss some limiting cases such as the quasi-static limit of slow velocity surface waves and the long wavelength limit. In Sec.3, some representative numerical examples of the EMSW's dispersion relation will be given for different plasma-waveguide parameters. Finally, the main conclusions will be presented in Sec.4.

General Dispersion Relation of EMSW

Consider a plasma column of width a surrounded by vacuum in a conducting cylindrical pipe of radius b . The wall of the pipe has a large, but finite conductivity σ_ω . In the presence of a plasma, modes can no longer be separated into pure transverse magnetic (TM) and transverse electric (TE), except for the lowest azimuthal symmetric mode [16, 17, 18, 19]. For uniform plasma with azimuthal symmetry, we only consider transverse magnetic modes such that $H_z = 0$ since transverse electric modes with $E_z = 0$ do not exist for the azimuthal symmetric mode. All other field components will be obtained from E_z using the Maxwell's field equations. In frequency domain, we have the following Maxwell's curl equations,

$$\nabla \times \mathbf{E} = i\omega\mu_0 \mathbf{H}, \quad \nabla \times \mathbf{H} = -i\omega \varepsilon \mathbf{E}, \quad (2.1)$$

where $\varepsilon = \varepsilon_0 \varepsilon$ and ε is the dielectric constant of the medium under consideration. Due to the azimuthal symmetry, the only

nonvanishing field components are E_z , E_r and H_θ . For modes propagating along the positive z-axis such as $e^{i(kz-\omega t)}$, and upon using circular cylindrical coordinates, we obtain the following equations,

$$r^2 E_z'' + r E_z' - r^2 (k^2 - \omega^2 \mu_0 \epsilon) E_z = 0 \quad (2.2)$$

$$H_\theta = -i \frac{\omega \epsilon}{k^2 - \omega^2 \mu_0 \epsilon} E_z, E_r = -i \frac{k}{k^2 - \omega^2 \mu_0 \epsilon} E_z, \quad (2.3)$$

where the prime and double prime stand for differentiation with respect to the radial coordinate r . The wave equations for E_{pz} in the plasma region from $r=0$ to $r=a$ and for E_{vz} in the vacuum between a and b become

$$r^2 E_{pz}'' + r E_{pz}' - \tau^2 r^2 E_{pz} = 0, \quad (2.4)$$

$$r^2 E_{vz}'' + r E_{vz}' - \tau_0^2 r^2 E_{vz} = 0, \quad (2.5)$$

$$\tau^2 = k^2 - \omega^2 \mu_0 \epsilon_p, \tau_0^2 = k^2 - \omega^2 \mu_0 \epsilon_0. \quad (2.6)$$

The general solutions for E_z in both regions are as follows,

$$E_z = \begin{cases} AI_0(\tau r) & 0 < r < a \\ BI_0(\tau_0 r) + CK_0(\tau_0 r) & a < r < b, \end{cases} \quad (2.7)$$

$$E_z = \begin{cases} I_0(\tau r) & 0 \leq r \leq a \\ I_0(\tau_0 a) \frac{I_0(\tau_0 r) [i\tau_0 k_0(\tau_0 b) - z_m \omega \epsilon_0 k_0'(\tau_0 b)] - k_0(\tau_0 r) [i\tau_0 I_0(\tau_0 b) - z_m \omega \epsilon_0 I_0'(\tau_0 b)]}{I_0(\tau_0 a) [i\tau_0 k_0(\tau_0 b) - z_m \omega \epsilon_0 k_0'(\tau_0 b)] - k_0(\tau_0 a) [i\tau_0 I_0(\tau_0 b) - z_m \omega \epsilon_0 I_0'(\tau_0 b)]} & a < r < b, \end{cases} \quad (2.9)$$

where I_0' and K_0' are the derivatives with respect to the argument. Imposing the

$$\epsilon_P = \frac{\tau I_0(\tau_0 a) I_0'(\tau_0 a) [i\tau_0 K_0(\tau_0 b) - Z_m \omega \epsilon_0 K_0'(\tau_0 b)] - K_0'(\tau_0 a) [i\tau_0 I_0(\tau_0 b) - Z_m \omega \epsilon_0 I_0'(\tau_0 b)]}{\tau_0 I_0'(\tau_0 a) I_0(\tau_0 a) [i\tau_0 K_0(\tau_0 b) - Z_m \omega \epsilon_0 K_0'(\tau_0 b)] - K_0(\tau_0 a) [i\tau_0 I_0(\tau_0 b) - Z_m \omega \epsilon_0 I_0'(\tau_0 b)]}. \quad (2.10)$$

Equation (2.10) is the general dispersion relation for the TM electromagnetic surface waves on the interface between an axially symmetric plasma enclosed by vacuum in a resistive cylindrical pipe. Finite extent of plasma and bounding conductor in the transverse direction, and the finite surface impedance of the bounding wall are

where I_0 and K_0 are the zero order modified Bessel's functions of first and second kinds, respectively. The constants A , B and C are to be determined using appropriate boundary conditions at the plasma–vacuum and vacuum–metallic cylinder interfaces.

To find the unknown constants, we apply the continuity of E_z at $r=a$ and at $r=b$. On z the metallic surface $r=b$, we use the impedance (Leontovich) boundary condition to account for the finite resistivity of the surface [20, 21, 22, 23]. The surface impedance of the metallic surface Z_m is [21, 22],

$$Z_m = \frac{1-i}{\sigma_w \delta_s}, \quad \delta_s = \sqrt{\frac{2}{\mu_0 \sigma_w \omega}} \quad (2.8)$$

where σ_w is the wall conductivity and δ_s is the skin depth at frequency ω . The boundary conditions concerning the continuity of E_z at $r=a$ and the impedance boundary condition $E_{vz} = Z_m H_{v\theta}$ at $r=b$ results in the following expression for the longitudinal electric field E_z ,

continuity of H_θ at $r=a$ results in the following dispersion relation,

accounted for via a , b and Z_m , respectively.

For a perfectly conducting wall at $r=b$ such that $Z_m=0$ and for a cold plasma, equation (2.10) reduces into the following dispersion relation [7, 14, 15, 16, 17, 18],

$$\varepsilon_p = \frac{\tau I_0(\tau_0 a) I_0'(\tau_0 a) K_0(\tau_0 b) - I_0(\tau_0 b) K_0'(\tau_0 a)}{\tau_0 I_0'(\tau_0 a) I_0(\tau_0 a) K_0(\tau_0 b) - I_0(\tau_0 b) K_0(\tau_0 a)}. \quad (2.11)$$

With $I_0'(x) = I_1(x)$ and $K_0'(x) = -K_1(x)$, equation (2.11) can be written as follows,

$$\varepsilon_p = \frac{\tau I_0(\tau_0 a) \frac{I_1(\tau_0 a) \frac{K_0(\tau_0 b)}{I_0(\tau_0 b)} + K_1(\tau_0 a)}{I_0(\tau_0 a) \frac{K_0(\tau_0 b)}{I_0(\tau_0 b)} - K_0(\tau_0 a)}}{\tau_0 I_0'(\tau_0 a) \frac{I_1(\tau_0 a) \frac{K_0(\tau_0 b)}{I_0(\tau_0 b)} + K_1(\tau_0 a)}{I_0(\tau_0 a) \frac{K_0(\tau_0 b)}{I_0(\tau_0 b)} - K_0(\tau_0 a)}}. \quad (2.12)$$

For a cold plasma column in free space such that $b \rightarrow \infty$, the ratio $K_0(\tau_0 b)/I_0(\tau_0 b)$ varies with b as $e^{-2\tau_0 b} \rightarrow 0$. Accordingly, equation (2.12)

$$\varepsilon_p = 1 - \frac{\omega_p^2}{\omega^2} = -\frac{I_0(ka)K_1(ka)}{K_0(ka)I_1(ka)} \rightarrow \frac{\omega}{\omega_p} = \pm \frac{1}{\sqrt{1 + \frac{I_0(ka)K_1(ka)}{K_0(ka)I_1(ka)}}}. \quad (2.14)$$

Numerical Examples

The dispersion relation of equation (2.14) is plotted in Fig. 1 for ω/ω_p versus ka . For the electrostatic surface waves in a cold plasma, and in the absence of the bounding conducting surface, typical characteristics of slow phase velocity SW's are observed [7, 3]. For a fixed plasma width a and very small wave numbers k the curve starts at

takes on the following form,

$$\varepsilon_p = -\frac{\tau I_0(\tau a) K_1(\tau_0 a)}{\tau_0 I_1(\tau a) K_0(\tau_0 a)}. \quad (2.13)$$

For slow (electrostatic) wave conditions such that the phase velocity v_ϕ of the modes is much less than the speed of light $v_\phi = \omega/k \ll c$, eq.(2.13) takes the following form for $\tau = \tau_0 = k$ [14],

$\omega = 0$, but for large k values it approaches the cutoff frequency of the plasma–vacuum interface $\omega = \omega_p/\sqrt{2}$. Low and large values of ω for a fixed k correspond, respectively, to two different physical situations, namely, thin and thick plasmas. The dispersion curve is uniquely determined by the product of k and a , namely, $x = ka$.

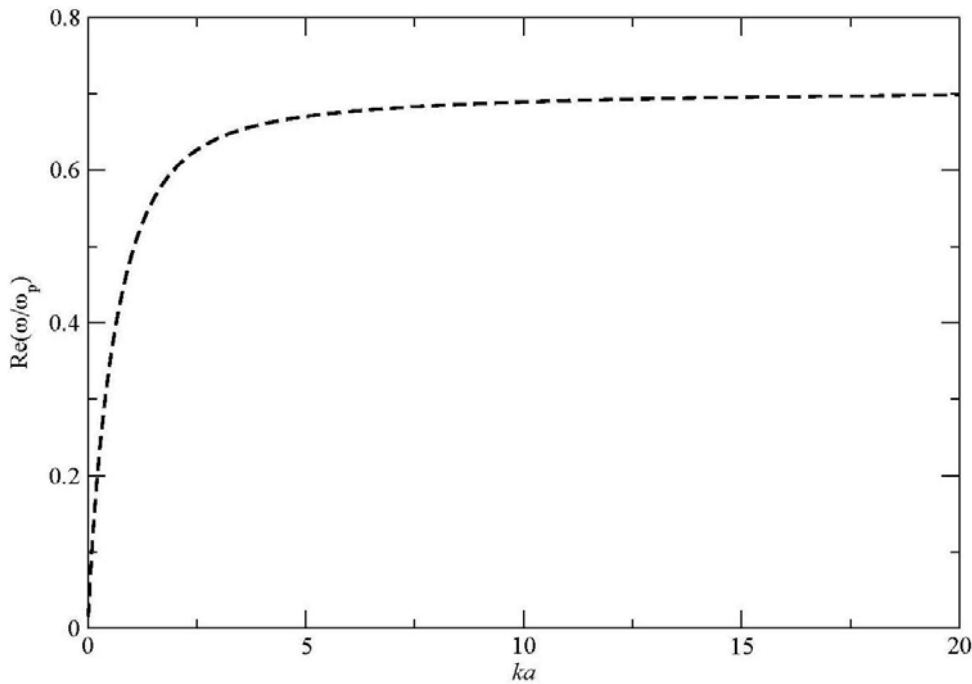


Fig. 1: Spectra of electrostatic SW's according to equation (2.14) for plasma in free space with the pipe wall moved to infinity.

When the radius of the bounding pipe is finite, and for a perfectly conducting wall, spectra of SW's for a cold plasma are described by equation (2.11). For the azimuthal symmetric mode with only TM modes being considered, characteristics of the dispersion curve are no longer determined by one parameter, as in the electrostatic case of equation (2.14). Plasma frequency and pipe radius, or the ratio (a/b) will affect the evolution of the curve. Presence of a good conducting bounding surface introduces additional dependence of the dispersion curve on the surface impedance Z_m of the metallic wall under consideration, as can be seen from

dispersion relation of equation (2.10).

Possible spectra of surface waves resulting from the numerical solutions of the nonlinear dispersion relation (2.10), together with equation (2.6), are shown in Figs. 2 to 4. Fig. 2 shows the real part of ω versus ka for the representative parameters of wall conductivity of $\sigma_\omega 1.1 \times 10^6$ S/m (siemens per meter), plasma frequency $f_p = 300$ MHz ($\omega_p = 2\pi f_p$), and inner pipe radius $b = 10$ cm for different ratios a/b .

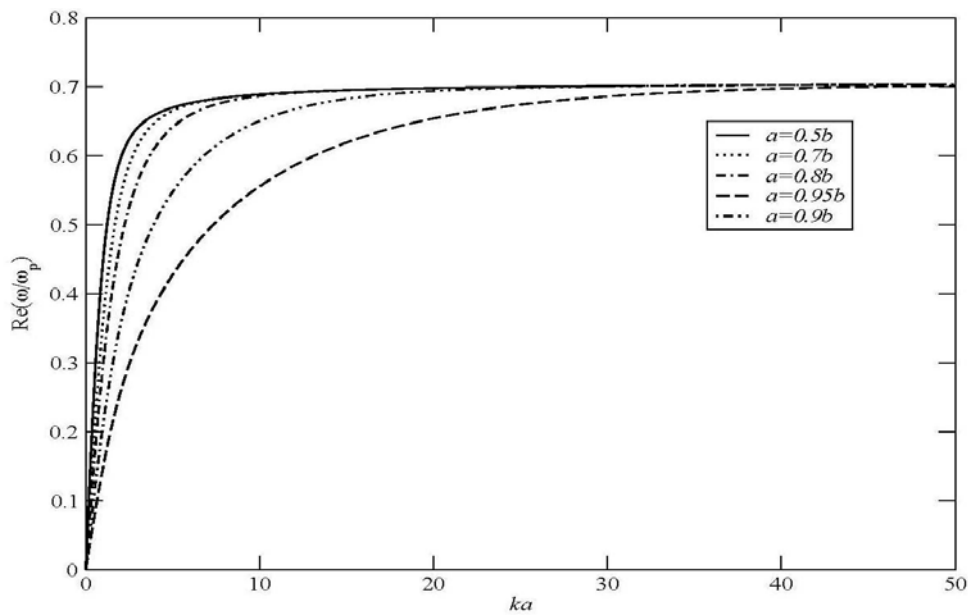


Fig. 2: Real part of the EMSW spectra according to equation (2.10) for pipe radius $b = 10$ cm, conductivity of stainless steel $\sigma_\omega = 1.1 \times 10^6$ S/m, plasma frequency $f_p = 300$ MHz, and for plasma widths $a = 0.5b$, $a = 0.7b$, $a = 0.8b$, $a = 0.9b$, and $a = 0.95b$.

Fig. 3 shows the imaginary part of the EMSW spectra according to equation (2.10) for pipe radius $b = 10$ cm, conductivity of stainless steel $\sigma_\omega = 1.1 \times 10^6$ S/m, plasma frequency $f_p = 300$ MHz with a values from low to high peaked curves $a = 0.5b$, $a = 0.8b$, $a = 0.9b$, and $a = 0.95b$. By changing the plasma frequency, the

imaginary part of the EMSW spectra of equation (2.10) is shown in Fig. 4 for $b = 10$ cm, plasma width $a = 0.5b$, wall conductivity of $\sigma_\omega = 1.1 \times 10^6$ S/m, plasma frequencies f_p in MHz with values from low to high peaked curves, respectively, 200 MHz, 300 MHz, 2 GHz, and 3 GHz

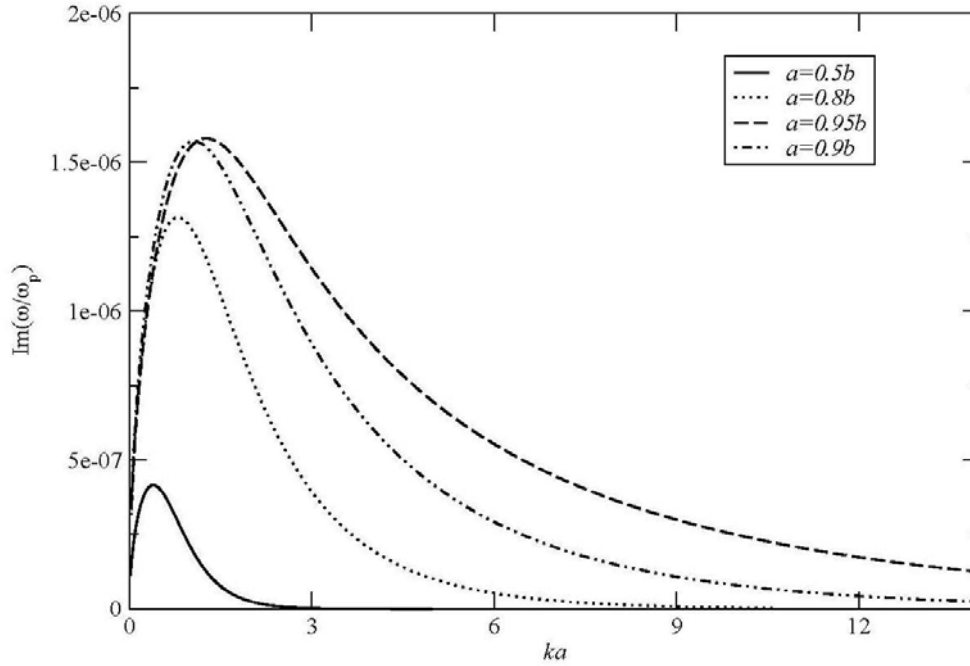


Fig. 3: Imaginary part of the EMSW spectra according to equation (2.10) for pipe radius $b = 10$ cm, conductivity of stainless steel $\sigma_{\omega} = 1.1 \times 10^6$ S/m, plasma frequency $f_P = 300$ MHz, and for plasma widths $a=0.5b$, $a = 0.8b$, $a = 0.9b$, and $a = 0.95b$.

For small a/b values corresponding to thin plasma or a plasma surface at large distance from the conducting wall of the pipe, we observe the same spectra characteristics of Fig. 1 of the electrostatic surface wave modes for plasma–vacuum interface. By bringing the conducting wall closer and closer to the surface of the plasma, Fig. 2 shows for large ka (or for short wavelengths) that all curves converge toward the plasma–vacuum cutoff frequency $\omega = \omega_p / \sqrt{2}$. However, for moderate ka values, we observe considerable modifications of spectra curves, namely, by increasing the ratio a/b , surface wave frequencies shift down with the curves being shifted to the right. For small ka values, the dispersion curve gives a non–vanishing group velocity of the SW's indicating a transport of energy, while for large k values

surface waves become localized oscillations with a vanishing group velocity.

The imaginary part of ω in Fig. 3 shows the opposite behavior, namely, all curves of different a/b ratio tend toward zero for large ka , and they show peaks that shift slightly to the right and become wider by increasing the ratio a/b . Including the finite, but large conductivity of the pipe wall, shows no observable effect on the real part of the surface wave spectra. Its effect manifests itself in introducing an imaginary part which has a peak value of 300 MHz for the parameters used to produce Fig. 3. For a fixed ratio $a/b = 0.5$ and varying plasma frequency, Fig. 4 shows that the imaginary part of ω can reach values of few tens of kilo Hz.

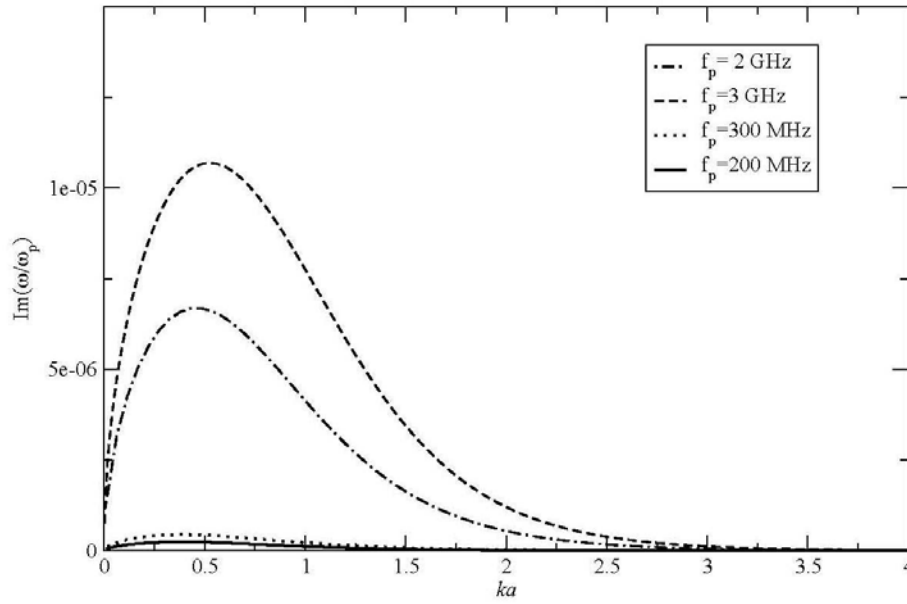


Fig. 4: Imaginary part of the EMSW spectra according to equation (2.10) for pipe radius $b = 10$ cm, Plasma width $a = 0.5b$, conductivity of stainless steel $\sigma_\omega = 1.1 \times 10^6$ S/m, plasma frequency $f_p = 200$ MHz, 300 MHz, 2GHz, and 3GHz.

The observed characteristics of the surface oscillation is lower than that of the bulk oscillations $\omega = \omega_p$ because a part of the wave field is outside the plasma and the effective force of interaction among the plasma particles is weaker [24]. Electric charges whose fluctuations give rise to surface waves are localized at the plasma–dielectric interface. In the long wavelength limit, these charges interact with each other as if they were in a medium with an effective dielectric constant $\varepsilon_{eff} = (\varepsilon_p + \varepsilon_d)/2$. The condition $\varepsilon_{eff} = 0$ results in the surface wave spectra $\omega = \omega_p / \sqrt{1 + \varepsilon_d}$, where $\varepsilon_d = 1$ for vacuum [see Figs. 1 to 4].

Conclusions

We have derived the general dispersion relation [equation (2.10)] for the TM electromagnetic surface waves on the interface separating an axially symmetric plasma and vacuum, both enclosed in a resistive cylindrical pipe. By assuming finite transverse width of a homogeneous cold plasma, whether in vacuum or in a resistive pipe, the spectra of surface waves resulting from the solution of the dispersion relation (2.10) have been found in terms a , ω_p , b and Z_m .

For the two equivalents physical situations of thin plasma or a conducting wall far away from the plasma surface, the observed spectra converge towards those of electrostatic surface wave modes existing at plasma–vacuum interface [see Fig. 1 and 2]. By bringing the conducting wall to a finite distance from the plasma–vacuum interface, large ka (short wavelengths) are not affected and all curves of Fig. 2 converge toward the plasma–vacuum cutoff frequency ($\omega = 0.707\omega_p$). On the other hand, for moderate values of ka , we observe appreciable modifications of spectra curves; by increasing the ratio a/b , surface wave frequencies shift down with the curves being shifted to the right.

For conducting pipe–walls that can be represented by a surface impedance Z_m , and since Z_m is frequency dependent, the dispersion relation of waves existing in the structure under consideration becomes a function of the dispersive properties of the wall. Due to the large wall conductivity, the small value of surface impedance shows no observable effect on the real part of the surface wave spectra, and its effect is found to introduce an imaginary part of ω having a peak value of 300 Hz [see Fig. 3]. By varying the plasma frequency and keeping the ratio

a/b fixed at 0.5, the imaginary part of ω is found to reach values of few tens of kilo Hz [see Fig. 4].

Including surface wave spectra in modeling beam dynamics, especially, in beam instability analysis and impedance calculations, can improve modeling of longitudinal and transverse beam dynamics. When coupled to an external driver such as particle beams [25, 26, 27, 28, 29, 30], surface wave fields may be amplified gaining energy at the expense of the beam energy, coupled to the beam fields, and finally affecting the beam dynamics. Contributions from including higher order waveguide modes resulting from medium asymmetries or off-axis motion of transversally kicked beams are at hand and are topics of future investigation.

Acknowledgments

A. Al-Khateeb would like to thank the Arab Fund for Economic and Social Development (AFESD, State of Kuwait) for the financial support of his stay at the GSI-Darmstadt (Germany) via their Fellowship Award. N. Laham would like to thank Al-AlBayt University for their kind hospitality during his stay there on a sabbatical leave. All authors thank the Council of Scientific Research of Yarmouk University, Irbid, Jordan, for partially supporting this work by the grant 6/2006.

References

- [1] R.L.Granatstein and S.P.Schlessinger. (1964). *J. Appl. Phys.* 35, 2846.
- [2] G. F. Matthews, S. J. Fielding, G. M. McCracken, C. S. Pitcher, P. C. Stangeby and M. Ulrickson. (1990). *Plasma Phys. Controlled Fusion* 32 (14), 1301.1320.
- [3] Yu. M. Aliev, H. Schlüter, and A. Shivarova. (2000). *Guided-Wave-Produced Plasmas* (Springer, Berlin).
- [4] Y.Kabouzi, D.B.Graves,E.Castanos-Martínez, and M. Moisan. (2007). *Phys. Rev. E* 75, 016402.
- [5] A. D. Boardman. (1982). *Electromagnetic Surface Modes* (Wiley, New York).
- [6] A. Shivarova and I. Zhelyazkov. (1978). *Plasma Phys.* 20, 1049.
- [7] A. W. Trivelpiece and R. W. Gould. (1959). *J. Appl. Phys.* 30, 1784.
- [8] R. L. Guernsey. (1969). *Phys. Fluids* 12, 1852.
- [9] V. Atanassov. (1981). *J. Plasma Phys.* 25, 285.
- [10] P. Kaw and J. B. McBride. (1970). *Phys. Fluids* 13, 1784.
- [11] H. C. Barr and T. J. M. Boyd. (1972). *J. Phys. A* 5, 1108.
- [12] P. C. Clemmow and J. Elgin. (1974). *J. Plasma Phys.* 12, 91.
- [13] P. Diament, V. L. Granatstein, and S. P. Schlessinger. (1966). *J. Appl. Phys.* 37, 1771.
- [14] Nicholas A. Krall and Alvin W. Trivelpiece. (1973). *Principles of Plasma Physics*, McGraw–Hill Book Company, pp.175.
- [15] A. W. Trivelpiece. (1958). Ph. D. thesis, California Institute of Technology.
- [16] A. Shivarova and I. Zhelyazkov. (1982). *Electromagnetic Surface Modes*, Edited by A. D. Boardman (Wiley, New York), Ch. 12.
- [17] D. S. Jones. (1964). *The Theory of Electromagnetism*, Edit. Sneddon, Ulam and Stark (Pergamon Press Ltd.), Ch. 7.
- [18] I. Akoa and Y. Ida. (1965). *J. Appl. Phys.* 35, 2565.
- [19] M. Moisan, A. Shivarova, and A. W. Trivelpiece. (1982). *Plasma Physics* 24, 1331.
- [20] M. A. Leontovich. (1948). *Issledovanya po Rasprostraneniyu Radiovoln* (USSR Acad. Press, Moscow).
- [21] D. M. Pozar, (1990). *Microwave Engineering*, Ch. 5, Addison - Wesley.
- [22] R. E. Collin. (1992). *Foundations of Microwave Engineering*, 2nd ed., McGraw - Hill, N. Y.
- [23] A. M. Al-Khateeb, O. Boine-Frankenheim, R. W. Hasse, and I. Hofmann. (2005). *Phys. Rev. E* 71, 026501-1.
- [24] M. Fuse and S. Ichimaru. (1975). *J. Phys. Soc. Japan* 38, 559.
- [25] S. R. Seshadri. (1972). *Can. J. Phys.* 50, 2244.
- [26] K. W. Ha and S. R. Seshadri. (1973). *J. Appl. Phys.* 44, 5280.
- [27] M. M. Shoucri and R. R. J. Gange. (1977). *J. Appl. Phys.* 48, 3132.
- [28] K. C. Swami and S. R. Sharma. (1977). *J. Appl. Phys.* 48, 5014.
- [29] B. Jazi, B. Shokri, and H. Arbab. (2006). *Plasma Phys. Control. Fusion* 48, 1105.
- [30] Yu A. Akimov, V. P. Olefir and N. A. Azarenkov. (2006). *Phys. Scr.* 74, 149.

Optical Characteristics of Amorphous Tin Nitride Thin Films Prepared by Ion Beam Assisted DC Magnetron Reactive Sputtering

I. M. Odeh

Physics Department, Yarmouk University, Irbid 21163, Jordan.

Received on: 7/12/2007; Accepted on: 5/6/2008

Abstract: This work reports the preparation of thin films of amorphous tin nitride (a-Sn₃N₄) by a novel implementation of simultaneous ion beam assisted deposition (IBAD) and reactive DC magnetron sputtering of a metal tin target in pure nitrogen plasma. The work also reports the optical characterization and determination of the optical constants of a-Sn₃N₄ thin film material. The refractive index n varies only slightly over the spectral range of 400-900 nm while the extinction coefficient k displays a gradual but significant increase starting at ~470nm. We have estimated the optical energy gap, E_{opt} , to be 2.32 ± 0.047 eV deduced from the transmittance measurements. Other important optical characteristics, such as the high frequency dielectric constant ϵ_{∞} , the average oscillator's wavelength λ_0 , the average oscillator strength S_0 , tangent loss ($\tan \delta$) and the optical conductivity σ , are also determined. Determination and interpretation of some of the optical properties are based on the single oscillator model proposed by Wemple and DiDomenico.

Key Words: Amorphous Materials, Reactive Sputtering, Ion Beam Assisted Deposition (IBAD), Thin Films, Optical Properties.

Introduction

Crystalline Tin (IV) Nitride of the form Sn₃N₄, non-stoichiometric SnN_x and Sn_xN_y in thin film forms have attracted the attention of a considerable number of researchers because of the potential applications of this material and their semi-conducting electrochromic properties. These include optical storage devices, write-once optical recording media, applications in microelectronic devices, as materials for optical switching devices for solar energy purposes, and optical recording media. Sn₃N₄ is also one of the Nitrides of the fourth group of the periodic table, which received much interest after the findings of the significant physical characteristics and the chemical properties [1-6].

Preparation methods of the various forms, powder and thin films, of tin nitrides varied from chemical procedures [7-9] to physical methods including reactive sputtering [2, 3, 10-14], reactive ion plating

[15], chemical vapor deposition [16] and plasma enhanced CVD [17].

Structural, optical, and electronic properties of almost any material, particularly thin films, depend essentially on the preparation technique. This is also true for the various forms of tin nitrides.

Most of the research works in the published literature have concentrated mainly on the crystalline forms of tin nitride produced by different methods [1-17].

In a review of the group (IV) nitrides, Kroke and Schwarz [18] mentioned that very few reports on tin nitride phases appeared in the literature. The electrical and optical characteristics of non-stoichiometric (SnN_x) crystalline tin nitride films have been examined for solar energy purposes [5, 19]. Maruyama and Morishita [12] reported a band gap of 1.5 eV for the crystalline SnN_x. Recent theoretical calculations [20] predict that γ -Sn₃N₄, in the spinel structure, is a semiconductor with a direct band gap of

1.40 eV and an attractive small electron effective mass of $0.17 m_0$.

Only a very limited number of research papers reported specifically on the amorphous tin nitride [21-23]. However, a thorough investigation of the optical characteristics, namely the refractive index, the absorption coefficient, dielectric constant and the optical energy gap of this interesting material in particular is not available.

We have prepared and studied the optical properties of amorphous tin nitride as a part of an ongoing research in the area of amorphous metal nitrides [24], and because of the need to explore the properties of alternative optical materials with potential applications. Our contribution to studying this type of film material takes a different approach in the deposition method, the structure form, and the method of determining the optical characteristics. Here we combine the ion beam assisted deposition (IBAD) and reactive DC magnetron sputtering for the deposition of the films. This novel approach [24] to preparation of thin films has produced amorphous tin nitride films that are compatible with the crystalline tin nitride films in some aspects of the optical characteristics and stability at room temperature conditions.

The optical constants, n , and k , of thin films are fundamental parameters both from theoretical and practical points of view. These provide essential information on the optical energy gap for semiconductors and insulators. Furthermore, the refractive index is necessary for the design and modeling of optical components and optical coatings [25].

In this work, we place a particular emphasis on the optical properties of the amorphous a-Sn: N films in comparison with the crystalline Sn_3N_4 . For calculating the optical constants and thicknesses of a-Sn:N thin films from transmittance measurements, we have applied the PUMA method and software [26], which has proved suitable for the purpose of retrieving the optical constants from transmittance measurements only [25].

Experimental Details and Preparation Conditions

The tin nitride films were deposited onto glass and silicon substrates in an Edwards E306 coating system fitted with an Edwards sputtering accessory (75 mm Magnetron

Cathode E093-01-000). An End-Hall ion beam source [27] was specifically designed, built, and retrofitted to the vacuum chamber (in house) in such a way that the ions produced would impinge onto the films during deposition process. A novel substrate holder (Hexa-holder) capable of loading six substrates simultaneously was also designed and constructed (in house) specifically for this work. The holder rotates at controlled speeds in a fashion such that the substrates always face the sputtering target one at a time during deposition. Ions from the ion beam source bombarded the substrate during deposition. In this way low energy ions ($<100\text{eV}$) would impart enough energy during the film deposition which would enhance the quality of the deposited films. This also improved the adhesion of the film to the substrate.

The substrates were thoroughly cleaned by first washing in a detergent (Decon5) and de-ionized water followed by rinsing in alcohol. All cleaning steps were carried out in an ultrasonic bath. To insure maximum cleaning and to remove oxides and contamination, both substrates and sputtering target were further bombarded with argon ions from the ion beam source for several minutes prior to deposition.

A 1kW DC power supply (MDX 1K Magnetron Drive from Advanced Energy, USA) delivered the DC power to the water-cooled tin target. An independent power supply (HP 6521A) and a low-tension transformer provided the necessary power to the ion source during deposition.

The spacing between the target and substrate was always maintained at 5cm. Reactive sputtering was carried out at room temperature in a glass bell jar vacuum chamber. The chamber was backfilled with pure nitrogen and maintained at a pressure of ~ 100 mbar during deposition. The power applied to the tin target was 100W dc. The vacuum chamber was always pumped down to better than 10^{-5} mbar and flushed with nitrogen to remove any residual oxygen prior to deposition.

As a routine procedure, we have performed the following characterization experiments on the as-deposited films.

X-ray Diffraction (XRD)

To establish the structure of the films whether crystalline or amorphous; X-ray diffraction (XRD) measurements were carried out using a computer controlled

Phillips PW1710 Diffractometer equipped with copper tube, for CuK α radiation, and a theta compensatory slit assembly. The diffractometer was operated under the following experimental conditions: a voltage of 35 kV, beam current of 40mA, step size of 0.02 2 θ , counting time of 0.01sec/step, 1mm receiving slit and a scanning range of 5-100 $^\circ$ 2 θ .

Transmittance Measurements

Transmittance (%T) of the as deposited tin nitride films was measured in a UV-Visible double-beam spectrophotometer over a spectral range of 400-900nm. The transmittances of the films were recorded with a blank substrate placed in the reference beam path.

Experimental Results and Discussion

Fig.1 shows a representative X-ray diffraction spectrum of the Tin Nitride (SnNx) films on glass substrates. The Tin Nitride films prepared here clearly do not display

any well-defined peaks, which are typical of crystalline structures. It is clear from the figure that the ion beam assisted DC magnetron reactive sputtering has produced amorphous films. Quantitative estimate of the composition from the data is not a straightforward conclusion. Therefore, the exact atomic ratio of the sputtered SnNx is unknown. However, since the films were prepared by sputtering from a pure tin target in pure nitrogen plasma, and all samples were non-metallic, as was deduced from the optical transmittance, it was clear that a reaction occurred and some sort of SnNx was present in the films. Nevertheless, Energy Dispersive X-ray analysis (EDX), a well known technique used for identifying the elemental composition of an area of the film and an integrated feature of the scanning electron microscope (SEM), revealed that x~3 in some of the films. Maruymama et al. [12] produced amorphous SnNx films at comparable conditions, except for the use of IBAD.

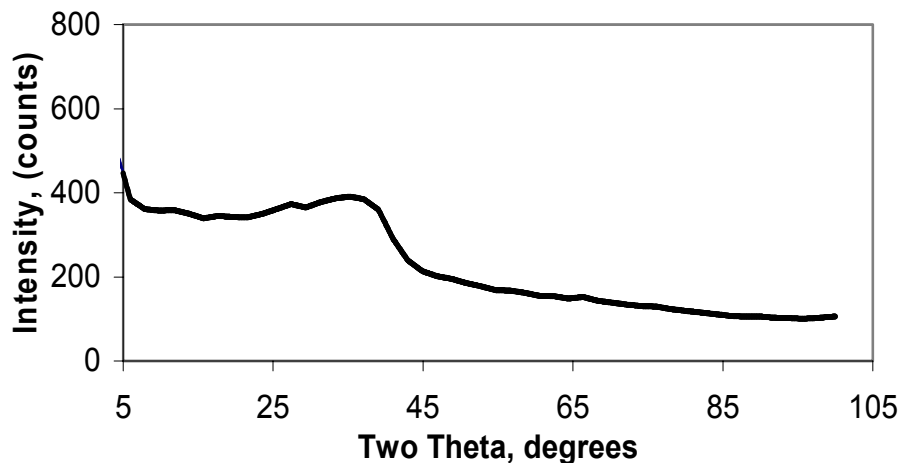


Fig. 1: A typical XRD pattern (Smoothed) of the a-Sn: N thin films on a glass substrate. The broad peak is due to the glass substrate.

Fig.2 shows transmittance spectra over a wavelength range of 400-900 nm for a representative set of films deposited at similar preparation conditions of nitrogen pressure (~100mbar) and dc power (~100W) over various time durations. The tin nitride films show almost invariably low optical transmittance over the visible range but

higher transmittance over the near infrared range. The spectra exhibit a behavior typical of the amorphous thin films where a broad absorption is evident compared to sharp absorption that usually characterizes crystalline materials. The films have a clear yellow to brown coloring depending on the thickness of films.

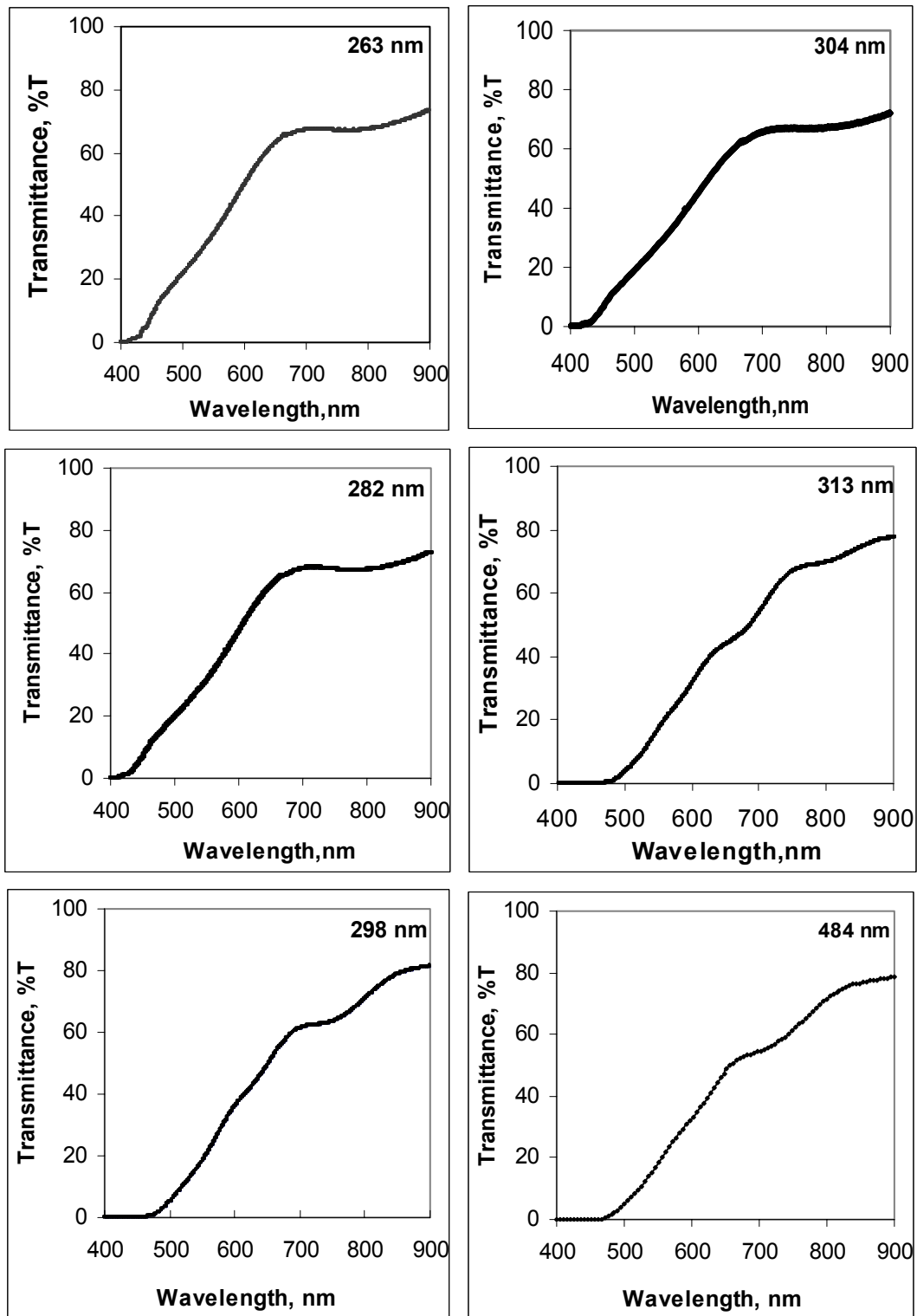


Fig. 2: Transmittances (%T) of a number of a-Sn: N thin films of different thicknesses (263- 484 nm) over the spectral range of interest (400-900 nm).

The Optical Constants: the Refractive Index n and Extinction Coefficient k

Determination of the real part, n , and the imaginary part, k of the complex refractive index is a challenging task when it comes to studying the optical properties of materials. The procedure involves complex equations

and extensive computing. A number of approaches and different methods exist for determining the optical constants [28-36].

The easiest are those, which depend on single transmittance measurement [25]. The refractive index n and the extinction coefficient k as well as the thickness d of the

amorphous tin nitride films studied here were determined from the transmittance data only using Point-wise Unconstrained Minimization Approach for the estimation of the thickness d and optical constants n and k of thin films (PUMA) approach and software [26]. It is a procedure and software

described by Birgin et al [26]. This method implements the complex optical equations derived and formulated by Heavens [29] and Swanepool [31, 32]. The transmission T of a thin absorbing film deposited on a thick transparent substrate is given by:

$$T = [Ax / (B - Cx + Dx^2)] \quad (1)$$

where:

$$A = 16n_s (n^2 + k^2)$$

$$B = [(n+1)^2 + k^2][(n+1)(n+n_s^2) + k^2]$$

$$C = [(n^2 - 1 + k^2)(n^2 - n_s^2 + k^2) - 2k^2(n_s^2 + 1)]2 \cos \theta$$

$$- k[2(n^2 - n_s^2 + k^2) + (n_s^2 + 1)(n^2 - 1 + k^2)]2 \sin \theta$$

$$D = [(n-1)^2 + k^2][(n-1)(n-n_s^2) + k^2]$$

$$\beta = 4\pi nd / \lambda$$

$$x = \exp(-\alpha d)$$

$$\text{And } \alpha = 4\pi k / \lambda$$

Where n_s is the refractive index of the substrate, n and k are the real and imaginary parts of the refractive index of the film respectively, d is the film thickness, λ is the wavelength of the incident light and α is the absorption coefficient of the film.

The substrate is sufficiently thick such that the additional interference effects resulting from the multiple reflections in the substrate are eliminated because they are incoherent.

In PUMA, the experimental transmittance obtained for the film is compared with a theoretical value. The difference between the two values is minimized until a best solution is reached for the refractive index n , the extinction coefficient k and the film thickness d . Thicknesses of the films

determined from PUMA calculations and based on the transmittances of the films ranged from 263 to 484 nm. Poelman et al [25] have reviewed and tested his method independently and shown it to produce excellent estimates of optical parameters of thin films.

Fig.3 shows average values of the refractive index n and the extinction coefficient k as a function of photon energy over the spectral range 400-900nm. The figure clearly shows that the refractive index exhibits only very slight increase over the spectral range. The extinction coefficient k displays a knee above 2.3eV (below 540nm). We attribute this change to higher dispersion and strong absorption of the tin nitride films at that wavelength.

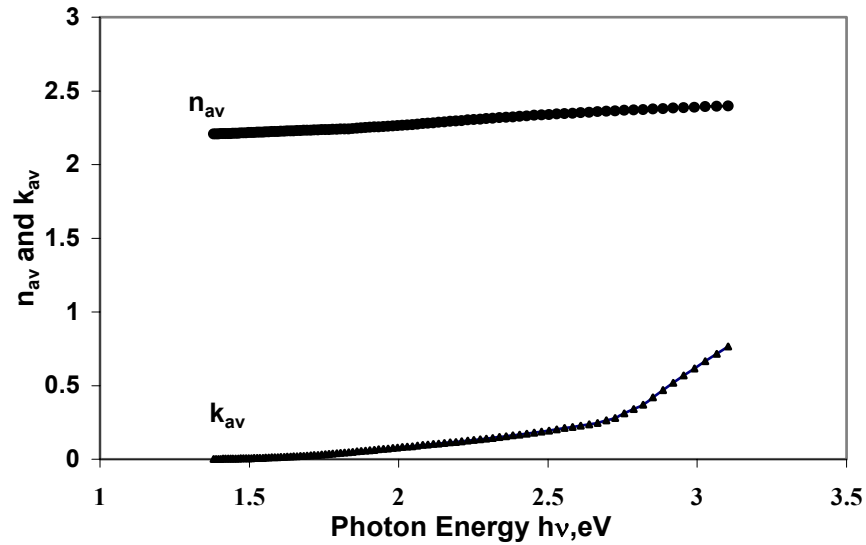


Fig. 3: Plots of n and k , the real refractive index and the extinction coefficient respectively, versus photon energy of the spectral range of interest (400-900 nm) for the a-Sn: N thin films.

A plot, Fig.4, of a typical absorption coefficient α of the tin nitride over the same spectral range clearly shows this inflection in the absorption. Nevertheless, it is not sharp

enough to resemble the sharp absorption of a crystalline material but consistent with amorphous thin film materials.

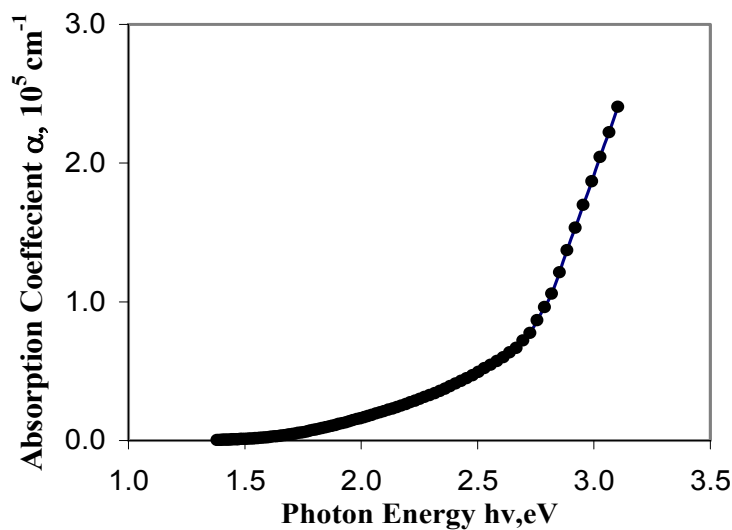


Fig. 4: A typical plot of the absorption coefficient, α , as a function of the photon energy of the spectral range of interest (400-900 nm).

In order to establish the optical transitions involved in the films, a plot of $\log(\alpha h\nu)$ against $\log(1/\lambda)$ should yield one straight line for a single optical transition. However if the plot should produce more

than one line then this would indicate multiple transitions [37].

Fig.5 shows such a plot, where it produced a single line, clearly indicating a single optical transition. We will show below that this is consistent with indirect transition.

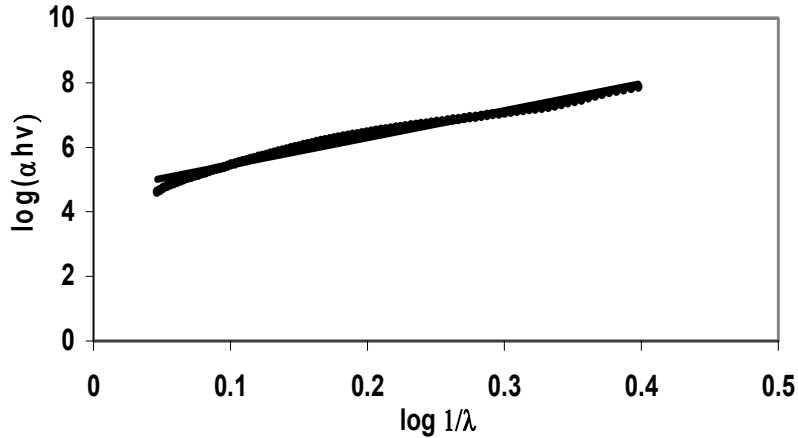


Fig. 5: A plot of $\log(\alpha hv)$ versus $\log(1/\lambda)$ shows a single line indicating a single optical transition.

The Optical Energy Gap E_{opt}

The optical energy gap E_{opt} is another important quantity that characterizes semiconductors and dielectric materials since it has a paramount importance in the design and modeling of such materials [25]. For the amorphous tin nitride films studied here, the optical energy gap was deduced from the intercept of the extrapolated linear part of the plot of $(\alpha hv)^{1/2}$ versus the photon energy hv as abscissa. This followed from the method of Tauc et al [38] where

$$(\alpha hv)^{1/2} = \text{constant}(hv - E_{opt}) \quad (2)$$

Fig.6 displays plots of $(\alpha hv)^{1/2}$ versus photon energy hv for a number of representative a-Sn: N films. The plot is a straight line as a best fit of the Tauc's relation above which suggests an indirect optical transition. An average value of optical energy gap E_{opt} of $2.320 \pm 0.047\text{eV}$ is calculated from the intercepts of the extrapolated lines with photon energy axis for the amorphous tin nitride films. The results of Fig.5 support a single optical

indirect transition. The value of the optical energy gap for the amorphous films is greater than the optical energy gap of 1.5 eV reported for the crystalline tin nitride Sn_3N_4 thin films prepared by radio frequency reactive sputtering [2, 3]. A recent ab initio calculation of the electronic structure and spectroscopic properties of spinel $\gamma\text{-Sn}_3\text{N}_4$ report that this is a semiconductor with a direct band gap of 1.40 eV [20].

The higher optical energy gap estimated in this work for a-Sn: N is consistent with the nature of the amorphous materials characterized by the absence of long-range order, high resistivity, and presence of defects. We believe that the bombardment of the films with low energy nitrogen ions from the ion source during deposition has contributed to the formation of the amorphous structure in addition to improving the quality, stability at laboratory conditions, and homogeneity of the amorphous films. Zeng et al [39] reported ion beam induced growth of amorphous alloy films of Co-Nb system by ion beam assisted deposition.

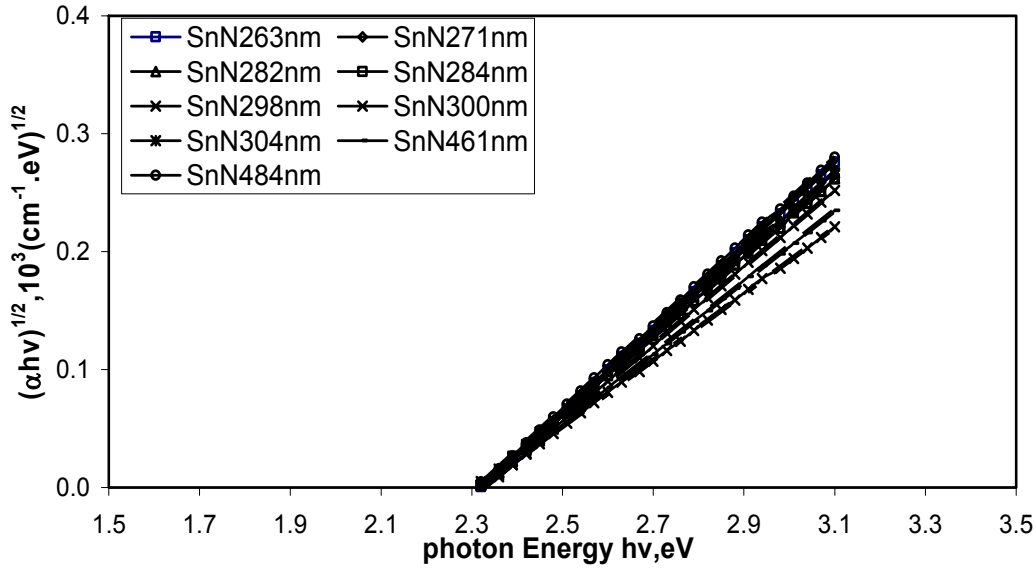


Fig. 6: Plots of $(\alpha hv)^{1/2}$ versus photon energy, hv , for a-Si:N illustrating the intercepts of the extrapolated linear part with the photon energy axis. An average estimate for the optical gap is $E_{opt} = 2.320 \pm 0.047\text{eV}$ for a number of films.

The above result of the optical energy gap may be further confirmed based on the following relation [40-43].

$$h^2 \nu^2 \epsilon_2 \sim (h\nu - E_{opt})^2 \quad (3)$$

where $\epsilon_2 (= 2nk)$ is the imaginary part of the dielectric constant.

A plot of $h\nu(\epsilon_2)^{1/2}$ versus photon energy exhibits a linear relation. This gives the optical gap when extrapolated to the energy axis. Fig.7 shows such a plot where the extrapolated linear part yields an optical energy gap of 2.28 eV in excellent agreement with the value $2.320 \pm 0.047\text{eV}$ obtained from the plot in Fig.6.

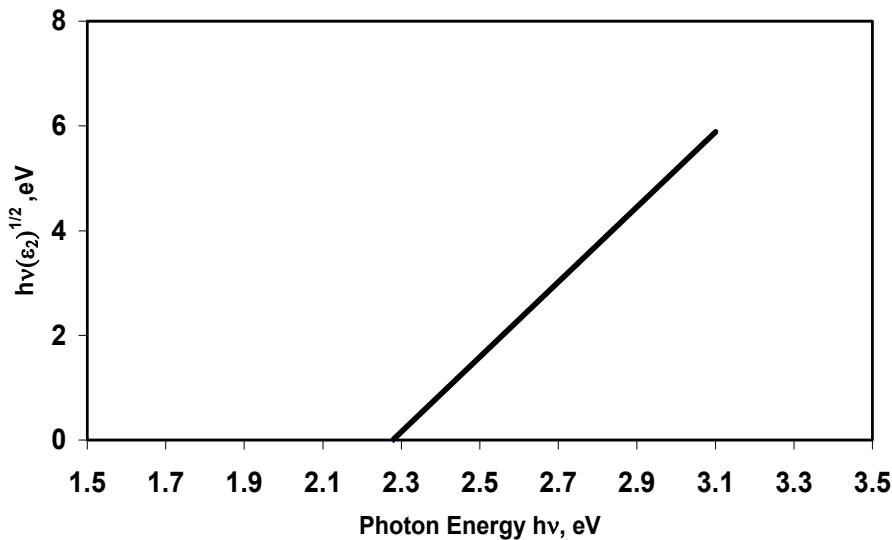


Fig. 7: A plot of $h\nu(\epsilon_2)^{1/2}$ versus photon energy, hv , for a-Sn: N illustrates the intercepts of the extrapolated linear part with the photon energy axis. An estimate of optical gap is $E_{opt} = 2.28\text{ eV}$.

Analysis of Dispersion of Films

Dispersion, the frequency dependence or energy dependence of the refractive index, can be analyzed based on the concept of a single oscillator model proposed by Wemple

and DiDominico [41, 42]. In this model, the following relation expresses the energy dependence of the refractive index, n as:

$$n^2 = 1 + E_d E_o / (E_o^2 - E^2) \quad (4)$$

where $E (=hv)$, E_o and E_d are the photon energy, the oscillator energy and the dispersion energy respectively. The parameter E_d is a measure of the intensity of the interband optical transition. It is independent of the optical band gap [44]. Fig.8 illustrates a plot of the dispersion relation (4) where $(n^2-1)^{-1}$ is plotted versus E^2 for the a-Sn: N films. Extrapolation of the lower energy part of the spectral range

where the films are more transparent displays a linear trend as shown in Fig.8. Dispersion energy E_d and oscillator energy E_o are estimated from the slope of -0.0077 and the intercept of 0.273 of the extrapolated linear part. We find these estimates from the equation of the best linear fit to be $E_d = 21.81\text{eV}$ and $E_o = 5.95\text{ eV}$. In addition, we find an estimate for the optical dielectric constant $\epsilon_\infty = n_\infty^2 = 4.664$.

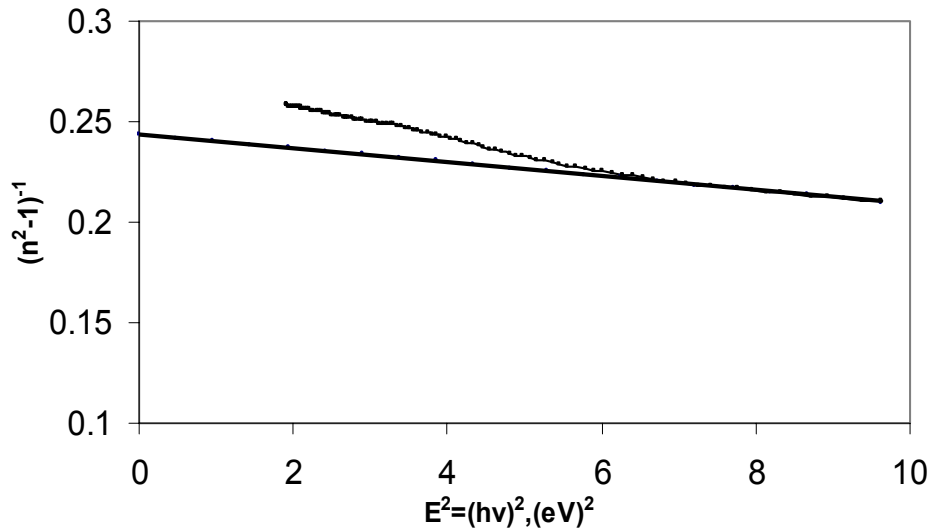


Fig. 8: A plot of the dispersion relation (4) where $(n^2-1)^{-1}$ is plotted versus $E^2 = (hv)^2$ for the a-Sn: N films.

The refractive index n , the wavelength λ and the lattice dielectric constant ϵ_L are related through the relation (5), which takes into consideration the contribution of the free carriers and the lattice vibration modes [44, 45]:

$$n^2 = \epsilon_L - C\lambda^2 \quad (5)$$

where $C = (e^2 N / 4\pi^2 c^2 \epsilon_o m^*)$, ϵ_L is the lattice dielectric constant, e is the electronic charge, N is the concentration of the free charge carriers, ϵ_o is the vacuum permittivity, m^* is the effective mass of the charge carrier, c is the speed of light and λ is the photon wavelength.

Conclusions

We have prepared thin films of amorphous tin nitride by a novel implementation of reactive DC magnetron sputtering and ion beam assisted deposition simultaneously. This technique has produced high quality, stable and uniform amorphous films. The bombardment of the film during deposition with low energy ions played a major role in producing the amorphous structure through imparting energies to the accumulating atoms. The

XRD patterns of films, Fig.1, clearly support this conclusion where the typical sharp peaks of crystalline structures are absent. Amorphous and crystalline tin nitrides both have similar yellow coloring for thinner films and dark brown for thicker films. The refractive index varied only slightly over the wavelength range of interest, 400-900 nm. The films are not highly absorptive over the visible part of the same spectral range.

A distinct difference between the amorphous and the crystalline tin nitrides is the invariably higher optical energy gap determined for the amorphous films of $2.320 \pm 0.047\text{eV}$ compared with the inconsistent values, 1.4-1.5 eV, for the crystalline films. The amorphous films have shown stability and have sustained normal lab and room temperature conditions for very long periods. Based on the optical properties presented in this work we believe that amorphous tin nitride may have potential applications as a decorative material, UV absorber and to a lesser extent as a hard coating.

Acknowledgements

We would like to thank the Deanship of Scientific Research and Higher Studies at Yarmouk University for the financial support. We would also like to thank Mosa Al-Jabali and A. Shehadeh from the Workshop at the physics Department, Yarmouk University.

References

- [1] T. Maruyama and Y. Osaki. (1996). *J. Electrochem. Soc.* 143, 326.
- [2] T. Maruyama and T. Morishita. (1996). *Appl. Phys. Lett.* 69, 890.
- [3] Y. Inoue, M. Nomiya and O. Takai. (1998). *Vacuum*, 51, 673.
- [4] Naoyuki Takahashi, Masahisa Takekawa, Tadashi Takahashi, Takato Nakamura, Masayuki Yoshioka, Wataru Inami and Yoshimasa Kawata. (2003). *Solid State Sciences*, 5, 587–589
- [5] N. Takahashi, K. Terada, T. Takahashi, T. Nakamura, W. Inami and Y. Kawata. (2003). *J. Electron. Mater.* 32, 268.
- [6] H. Lange, G. Wötting and G. Winter. (1991). *Angew. Chem.* 103, 1606.
- [7] L. Maya. (1992). *Inorg. Chem.* 31, 1958.
- [8] N. Scotti, H. Jacobs, W. Kockelmann and Z. Anorg. (1999). *Allg. Chem.* 625, 1435-1439.
- [9] M. P. Shemkunas, G. H. Wolf, K. Leinenweber and W. T. Petuskey. (2002). *J. Am. Ceram. Soc.* 85, 101.
- [10] J. C. Remy and J. J. Hantzpergue. (1975). *Thin Solid Films* 30, 197.
- [11] R. S. Lima, P. H. Dionisio, W. H. Schreiner and C. Achete. (1991). *Solid State Commun.* 79, 395.
- [12] T. Maruyama and T. Morishita. (1995). *J. Appl. Phys.* 77, 6641.
- [13] R. Kamei, T. Migita, T. Tanaka and K. Kawabata. (2000). *Vacuum*, 59, 764.
- [14] H. M. Al-Mosawi. (1999). MSc thesis, Yarmouk University,
- [15] Y. Inoue, Y. Fukui and O. Takai. (1994). *Proc. Symp. Plasma Sci. Mater.* 7, 147.
- [16] R. G. Gordon, D. M. Hoffman and U. Riaz. (1992). *Chem. Mater.* 4, 68.
- [17] D. M. Hoffman, S. P. Rangarajan, S. D. Athavale, D. J. Economou, J. R. Liu, Z. Zheng and W. K. Chu. (1995). *J. Vac. Sci. Technol.*, A 13, 820.
- [18] E. Kroke and M. Schwarz. (2004). *Coordination Chemistry Reviews*, 248, 493–532.
- [19] T. Lindgren, M. Larsson and S. E. Lindquist. (2002). *Solar Energy Mater. Solar Cells* 73, 377.
- [20] W. Y. Ching and P. Rulis. (2006). *Physical Review B* 73, 045202-1-9.
- [21] Y. Inoue, Y. Fukui and O. Takai. (1994). *Proc. Symp. Plasma Sci. for Materials*, 7, 147.
- [22] Y. Inoue and O. Takai. (1996). *Proc. Symp. Plasma Sci. for Materials*, 9, 39.
- [23] Dirk Lu'tzenkirchen-Hecht* and Ronald Frahm. (2005). *Thin Solid Films*, 493, 67 – 76.
- [24] I. M. Odeh. (2007). Fabrication and optical constants of amorphous copper nitride thin films prepared by ion beam assisted dc magnetron reactive sputtering. In press. *Journal of Alloys and Compounds*, doi:10.1016/j.jallcom.2006.12.020.
- [25] D. Poelman and P. F. Smet. (2003). *J. Phys. D: Appl. Phys.* 36, 1850–1857.
- [26] E. G. Birgin, I. Chambouleyron, and J. M. Martínez. (1999). *Journal of Computational Physics*, 151, 862-880.
- [27] H. R. Kaufman and R. S. Robinson. (1987). *Operation of Broad-Beam Sources*, Commonwealth Scientific corporation.
- [28] M. Born and E. Wolf. (1980). *Principles of Optics*, Pergamon, London.
- [29] O. S. Heavens. (1991). *Optical Properties of Thin Films*, Dover, New York.
- [30] J. C. Manifacier, J. Gasiot, and J. P. Fillard. (1976). *J. Phys. E: Sci. Instrum.* 9, 1002.
- [31] R. Swanepoel. (1983). *J. Phys. E: Sci. Instrum.* 16, 1214–1222.
- [32] R. Swanepoel. (1984). *J. Phys. E: Sci. Instrum.* 17, 896–903.

- [33] A. R. Forouhi and I. Bloomer. (1986). Phys. Rev. B 34, 7018–26.
- [34] A. R. Forouhi and I. Bloomer. (1988). Phys. Rev. B 38, 1865–74.
- [35] I. Bloomer and R. Mirsky. (2002). Photonics Spectra, 86–92.
- [36] A. R. Forouhi and I. Bloomer. (1991). Handbook of Optical Constants of Solids II, Ed E. D. Palik Boston: Academic, 151–75.
- [37] H. S. Soliman, B. A. Khalifa, M. M. El-Nahass and E. M. Ibrahim. (2004). Physica B 351, 11–18.
- [38] J. Tauc, R. Grigorovici and A. Vancu. (1966). Phys. Status Solidi 15 627.
- [39] F. Zeng, F. Pan. (2002). Journal of Alloys and Compounds, 335, 181–187.
- [40] M. M. Abdel-Aziz, I. S. Yahia, L. A. Wahab, M. Fadel and M. A. Affi. (2006). Applied Surface Science, 252, 8163–8170.
- [41] M. DiDomenico and S. H. Wemple. (1969). J. Appl. Phys. 40, 720.
- [42] S. H. Wemple and M. DiDomenico. (1971). Phys. Rev. B3, 1338.
- [43] M. G. Hutchins, O. Abu-Alkhair, M. M. El-Nahass and K. Abd El-Hady. (2006). Materials Chemistry and Physics, 98, 401–405
- [44] J. Roberts, A. Marks and W. Alexander. (1985). J. Appl. Optics, 24, 3680 .
- [45] J. N. Zemel, J. D. Jensen and R. B. Schouler. (1965). Phys. Rev. A.140, 330.

Magnetization Measurements on “as Prepared” and Annealed $\text{Fe}_{3-x}\text{Mn}_x\text{Si}$ Alloys

M. S. Lataifeh^a, M. O’Shea^b, A. S. Saleh^c and S. H. Mahmood^c

^a Department of Physics, Mu’tah University, Mu’tah, Jordan

^b Kansas State University, Manhattan, KS 66506-2601, USA

^c Department of Physics, Yarmouk University, Irbid, Jordan

Received on: 30/10/2007; Accepted on: 17/3/2008

Abstract: The magnetic properties of the alloy system $\text{Fe}_{3-x}\text{Mn}_x\text{Si}$ have been studied by measuring magnetization for samples with $x = 0, 0.1, 0.25, 0.5$, and by thermal scanning techniques for samples with $x = 0, 0.1$. The results reveal that the system is ferromagnetic in this composition range. Zero field cooling and field cooling magnetization measurements indicate a similar magnetic ordering and magnetic anisotropy in all samples. The saturation magnetization for the annealed samples was higher than that for “as prepared” samples. This is attributed to the reduction of magnetic domain boundaries rather than to improving magnetic order as a result of annealing. Further, T_C values determined from thermal DSC measurements are in good agreement with previously reported results based on magnetic measurements.

Keywords: Heusler Alloys, Magnetization, Magnetic Order.

Introduction

The unit cell of the $\text{Fe}_{3-x}\text{Mn}_x\text{Si}$ alloys consists of four interpenetrating f.c.c sublattices A, B, C, and D, with origins displaced along the body diagonal at the points A (0,0,0), B (1/4,1/4,1/4), C (1/2,1/2,1/2) and D (3/4, 3/4, 3/4). Fe_3Si crystallizes in the DO_3 structure with the A, B, and C sites occupied by Fe and the D site by Si [1, 2].

The magnetic behavior of the alloy $\text{Fe}_{3-x}\text{Mn}_x\text{Si}$ exhibits ferromagnetism at low Mn concentration ($x < 0.75$), and shows a complex magnetic structure at higher values of x [1]. As Mn is introduced into the alloy, it preferentially occupies the B site for $x < 0.75$, and then begins to occupy the A, C sites as x increases. It has been found also that nearest neighbor interactions dominate at low Mn concentration [3].

This system has attracted the interest of many researchers [1-12] since it shows a variety of magnetic phases as x is increased up to 3.0. It is ferromagnetic below $x=0.75$,

and shows spin glass behavior for $0.75 < x < 1.2$.

The substitution of Mn for Fe in these pseudo-binary alloys has been studied using various techniques. Fe Mössbauer spectroscopy (MS) was used to study the dependence of the average hyperfine fields at the different sites on Mn concentration [2-4, 7, 8, 12]. Magnetic and crystallographic properties have also been studied by X-ray and neutron diffraction techniques, together with magnetization, resistivity, and magnetostriction measurements [1,9]. Ferromagnetic resonance studies have also been made on this system [5,6]. The above results show that the Mn substitution reduces the magnetic exchange energy, thus leading to a reduction in the critical (Curie or Neel) temperature.

In this work we present the results of magnetization measurements using the Superconducting Quantum Interference Device (SQUID), and the dependence of magnetization on the temperature under zero field cooling and field cooling conditions

on the as prepared and annealed alloys. Also, thermal measurements using Differential Scanning Calorimetry (DSC) is used to determine the Curie temperature for some of the samples under investigation. This work is part of an ambitious project, intended to carry a thorough investigation of the system by studying a series of samples with different Mn concentrations using MS and X-ray techniques.

Experimental

Appropriate proportions of high purity metals (better than 99.9%) were melted in an argon arc furnace, forming a series of the alloy buttons. The buttons were flipped and remelted several times in order to insure homogeneity. The mass of each button was measured and compared with the total mass of the initial powders; mass losses of 1% or less were found, which indicates that the achieved concentrations are consistent with the desired ones. The alloy buttons were then crushed into fine powders, part of which was used to prepare the "as prepared" samples. The "annealed samples" were prepared by annealing parts of the powders under vacuum in quartz tubes for two weeks at 800 °C and then left to cool to room temperature.

Magnetization measurements were performed using a superconducting Quantum Interference Device (SQUID) Magnetometer, at the Department of Physics, Kansas State University, USA. Measurements were made in the temperature range from 10 K to 400 K in an applied magnetic field up to 5.5 Tesla. To reduce demagnetization, the powders were placed in cylindrical sample holders.

For thermal DSC measurements, 25-40 mg of the powder were placed in a crucible beside an inert reference and subjected to the same temperature program. The temperature was scanned from 100 °C to 600 °C. The magnetic phase transition could be exothermic or endothermic, which

produces a signal in the DSC scan, from which the critical transition temperature is determined.

Results and Discussion

Fig. 1 shows the Zero Field Cooled (ZFC) and the Field Cooled (FC) magnetization curves for the two samples Fe_3Si and $\text{Fe}_{2.75}\text{Mn}_{0.25}\text{Si}$. The ZFC curves were obtained by cooling the sample from Room Temperature (RT) down to 10 K in zero field, and then a small field (200 Oe) is applied and the magnetization is measured as the sample is warmed up to 400 K. This procedure will have a maximum effect on the magnetic domains with the least magnetic anisotropy, and will produce a net magnetization in the direction of the applied field.

The FC curves were measured by first cooling the sample down to 10 K in the presence of the small applied field (200 Oe) and then measuring the magnetization as the sample is warmed up to 400 K. Cooling down the sample in a 200 Oe field is sufficient to have more alignment of magnetic domains at 10 K. So we expect to observe larger magnetization in the FC process than in ZFC case.

The curves (Fig. 1) show almost constant magnetization as the temperature increases, indicating ferromagnetic order. The difference in magnetization between the ZFC and the FC processes is small and similar for the samples under investigation, indicating similar magnetic anisotropy in this composition range. The observed ferromagnetic behavior is consistent with the results of other workers using magnetization [1,9] and MS [4,7,8,12] measurements. Fig.1 also reveals a reduction in the magnetization upon replacement of Fe by Mn, which indicates a lower magnetic moment per formula unit. These findings are consistent with the observed decrease in the average hyperfine field with increasing Mn concentration as obtained from Mössbauer spectra [8,12].

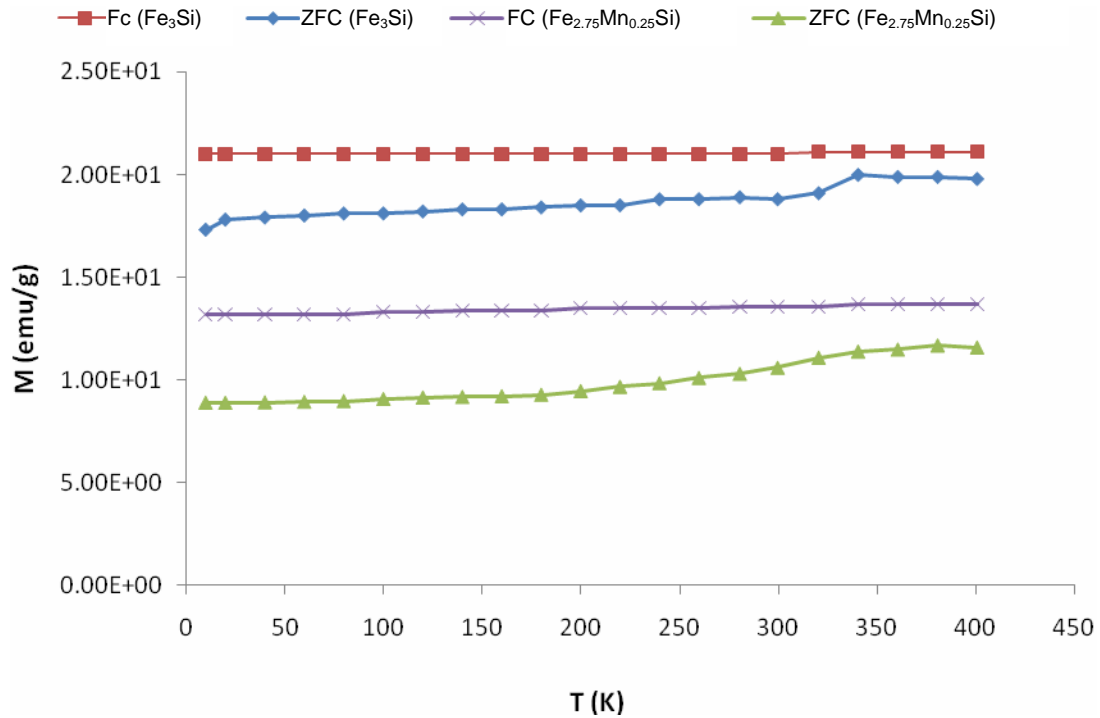


Fig. 1: ZFC and FC magnetization curves for the samples Fe_3Si and $\text{Fe}_{2.75}\text{Mn}_{0.25}\text{Si}$. The solid line is a guide for the eye.

The spontaneous magnetization at 10 K was found to be higher for FC process than for ZFC. This indicates that the partial alignment of the moments due to the application of the 200 Oe field in the FC process is responsible for the difference in magnetization M [$M(\text{FC}) - M(\text{ZFC}) > 0$]. This difference becomes smaller as T increases due to the slight increase in M in the ZFC process, and the saturated value of M in the FC process. The increase in M in the ZFC process is associated with progressively increasing the freedom for the orientation of the magnetic moments in the direction of the applied field due to the progressive unblocking of the frozen random state at 10 K. Ideally, the ZFC and FC curves would meet at 400 K. However, due to the irreversibility of the magnetic properties upon cooling and heating, a small difference

in M is observed at 400 K. It is obvious also that M does not decrease with increasing temperature, indicating that the temperature range of the measurements is way below T_C .

The saturation magnetization, M'_s for the annealed samples is higher than that for the as prepared ones at a given temperature (Fig.2). This result could be attributed to either the improvement of magnetic order, or the reduction in the magnetic domain boundaries as a result of annealing. However, MS data [8] do not show any appreciable difference in the hyperfine field distributions for the two sets of samples. Due to the fact that MS is sensitive to local atomic environments, but not to domain structure, it is more likely that the effect of annealing results in the reduction of domain boundaries rather than decreasing the magnetic disorder.

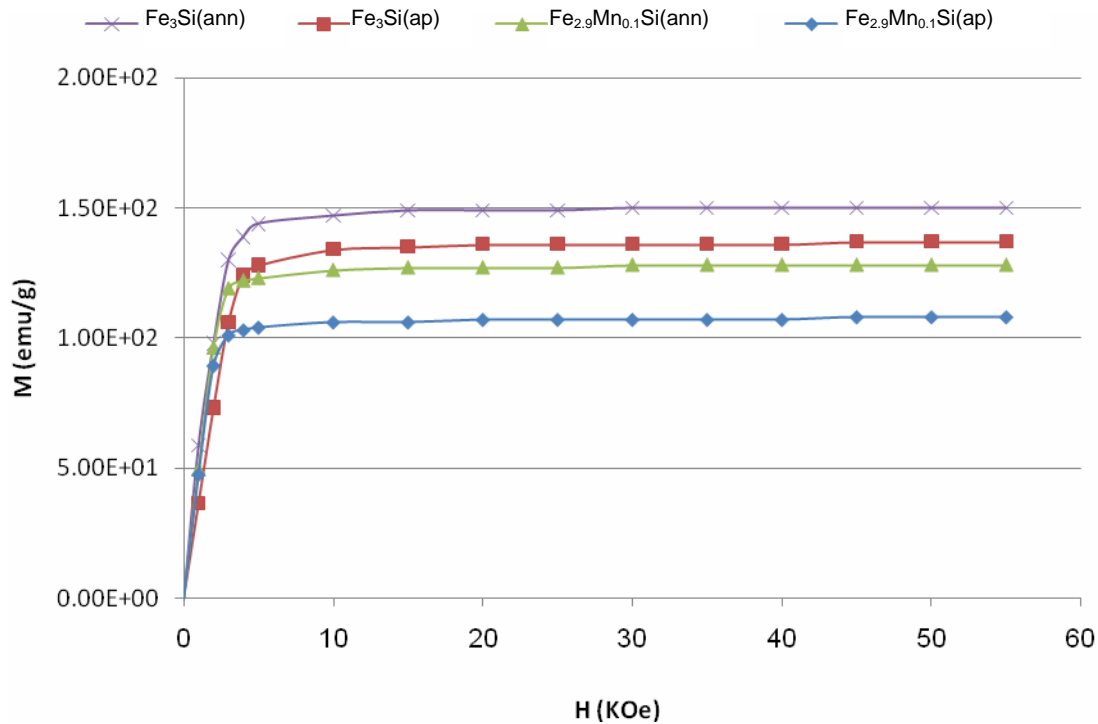


Fig. 2: Magnetic isothermal curves (M vs H) at 300 K for annealed Fe_3Si , as prepared Fe_3Si , annealed $\text{Fe}_{2.9}\text{Mn}_{0.1}\text{Si}$, and as prepared $\text{Fe}_{2.9}\text{Mn}_{0.1}\text{Si}$.

Also, Fig.3 shows the magnetization curves for the annealed samples at 300 K and at 10 K. The figure shows that the difference in M_s between RT and 10 K for a given sample is small (~6%). This small change in M_s is due to the fact that the measurements were made far below the

Curie temperature, T_C ($RT \leq 0.5 T_C$). Fig.3 also shows a reduction in the saturation magnetization with increasing x , consistent with the reduction of the magnetic moment per formula unit upon replacement of Fe by Mn.

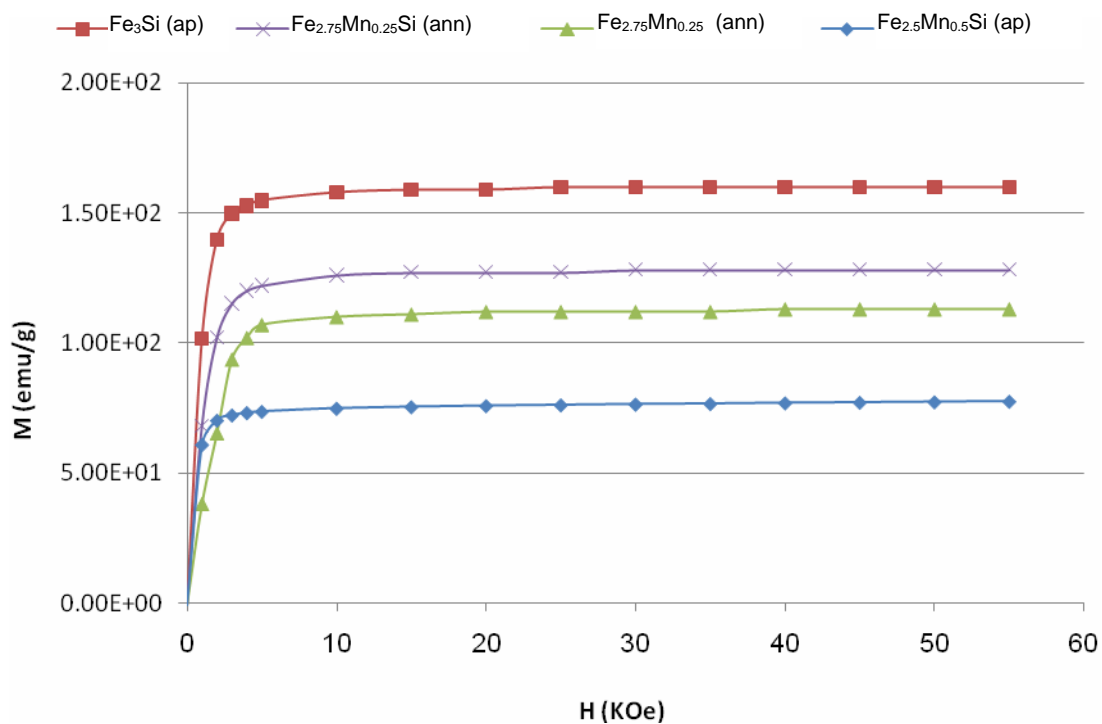


Fig. 3: Magnetic isothermal curves (M vs H) for as prepared Fe_3Si at 10 K, annealed $\text{Fe}_{2.75}\text{Mn}_{0.25}\text{Si}$ at 10 K, annealed $\text{Fe}_{2.75}\text{Mn}_{0.25}\text{Si}$ at 300 K, as prepared $\text{Fe}_{2.5}\text{Mn}_{0.5}\text{Si}$ at 300 K.

Differential scanning calorimetry (DSC) measurements were performed for the two samples Fe_3Si and $\text{Fe}_{2.9}\text{Mn}_{0.1}\text{Si}$. The Curie temperature for these samples deduced from the measurements were 849 K and 794 K, respectively. It was reported in reference [1] that T_C for the system under investigation

decreases almost linearly as x increases up to 0.9. Fig.4 shows that our values for T_C determined from the DSC measurements are consistent with the linear drop of T_C with increasing x up to 0.9. Our results are also in good agreement with previous results [1,3,10, 11].

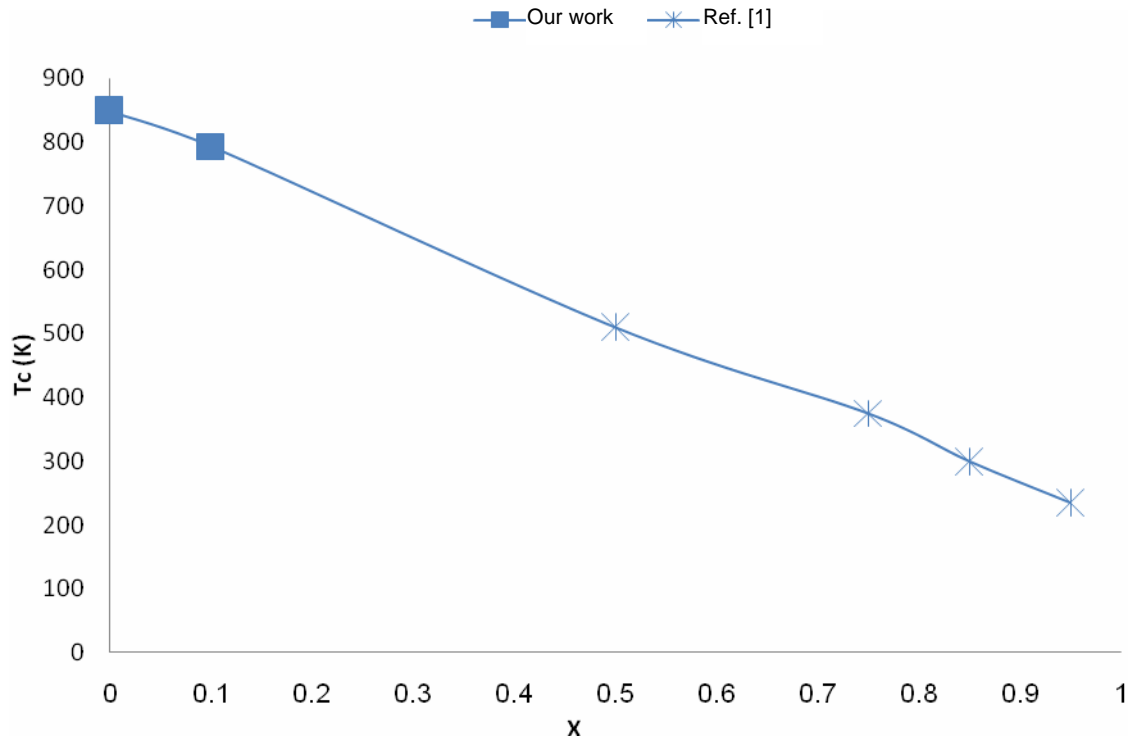


Fig. 4: Variation of the Curie temperature T_C with composition x (this work for $x=0.0$ and 0.1 , and other values are from reference [1]). The solid line is a guide for the eye.

Conclusions

Thermal magnetization curves for samples of Fe_3Si and $\text{Fe}_{2.75}\text{Mn}_{0.25}\text{Si}$ have shown difference in M between the ZFC and the FC processes. The magnetization measured in the ZFC process increase slightly with increasing the temperature due to the progressive unblocking of the magnetic moments, while that measured in the FC process remains almost constant with increasing temperature.

The saturation magnetization at a given temperature is found higher for the annealed sample than for the as prepared one. This is attributed to the reduction of the magnetic domain boundaries rather than the

improvement of magnetic order as a result of annealing.

The Curie temperature T_C was determined for the samples with $x = 0$ and 0.1 using DSC measurements. Our results are consistent with previous results obtained from magnetization measurements.

Acknowledgment

One of the authors (M.S. Lataifeh) would like to acknowledge the grant obtained from the Center for Theoretical and Applied Physical Sciences (CTAPS) at Yarmouk University as a partial support towards the completion of this work. Thanks are due to Dr. Ali Qudah from Mu'tah university for his help in the DSC measurements.

References

1. S. Yoon and J. G. Booth. (1977). *J. Phys. F: Metal Phys.* Vol. 7, No. 6, 1079-1095.
2. J. T. T. Kumaran and C. Bansal. (1990). *Solid State Commun.* Vol. 74, No. 10, 1125-1130.
3. J. T. T. Kumaran and C. Bansal. (1989). *Solid State Commun.* Vol. 69, No. 7, 779-783.
4. G. A. Al-Nawashi. (1999). MSc. Thesis, Structural and Mossbauer Spectroscopy study of $Fe_{3-x}Mn_xSi$ alloys, Yarmouk University.
5. S. W. Kaul, T. V. S. M. Mohan and Babu, C. Bansal. (1995). *J. Magn. Magn. Mater.* 140-144, 127-128.
6. Chakravarti, R. Ranganathan and S. Chatterjee. (1994). *J. Magn. Magn. Mater.* 138, 329-338.
7. S. H. Mahmood, A. Lehlooh, A. S. Saleh and N. Darlington. (1997). *Proceedings of the 5th International Conference on Advanced Materials, Islamabad, Pakistan* 321-323.
8. G. A. Al-Nawashi, S. H. Mahmood, A. D. Lehlooh and A. S. Saleh. (2002). *Physica B*, 321, 167-172.
9. M. R. Said, Y. A. Hamam, I. Abu-Aljarayesh and S. Mahmood. (1999). *J. Magn. Magn. Mater.* 195, 679-686.
10. V. A. Niculescu, T. J. Burch and J. I. Budnick. (1983). *J. Magn. Magn. Mater.* 39, 223-267.
11. T. J. Burch, J. I. Budnick, V. A. Niculescu, K. Raj and T. Litrenta. (1981). *Phys. Rev. B*24, 3866.
12. S. H. Mahmood, A. F. Lehlooh, A. S. Saleh and F. E. Wagner. (2004). *Physica Status Solidi (b)*, Vol. 241, No. 6, 1186-1191.

Magnetic and Structural Studies of $\text{Ba}_{0.5}\text{Sr}_{0.5}(\text{ZnTi})_x\text{Fe}_{12-2x}\text{O}_{19}$ Prepared by Ball Milling

A. González-Angeles^a, A. Grusková^b, J. Lipka^b, J. Sláma^b and V. Jančárik^b

^a*Facultad de Ingeniería, Universidad Autónoma de Baja California, Blvd. Benito Juárez s/n, Cp 21280 Mexicali, B. C., México.*

^b*Faculty of Electrical Engineering and Information Technology, Slovak University of Technology, Ilkovičova 3, 81219 Bratislava, Slovak Republic.*

Received on: 4/3/2008; Accepted on: 5/6/2008

Abstract: Results on structural and magnetic studies of $\text{Ba}_{0.5}\text{Sr}_{0.5}(\text{ZnTi})_x\text{Fe}_{12-2x}\text{O}_{19}$ (where $x = 0.2$ to 0.6) ferromagnetic powders prepared by mechanical milling are presented. The obtained X-ray diffraction patterns of Zn-Ti substituted $(\text{BaSr})_{0.5}\text{M}$ samples showed Magnetoplumbite phase formation for all substituted mixtures; no other secondary phases were detected. Scanning electron microscope analyses revealed that all processed samples possess particle size much below $1\ \mu\text{m}$ and may exhibit promising magnetic and dielectric properties. Magnetic measurements showed that the intrinsic coercivity, H_{ci} , and remanent magnetization, M_r , decreased as the substitution took place, while the saturation magnetization, M_s , remained almost constant (diminution $\sim 9\%$). H_{ci} , decreased from 389.92 down to $171.88\ \text{k A/m}$ that represents a 56% drop, whilst M_r registered a fall of $\sim 17\%$.

Key Words: Magnetic Studies, Mössbauer Spectroscopy, Ba-Sr-Hexaferrites, Ball Milling.

Introduction

Intensive work have been done to modify the magnetic parameters of barium or strontium hexaferrite by substitution of Fe^{3+} ions with other cations or cation combinations such as Co-Ti, Zn-Sn, Co-Sn, Ni-Zr, Co-Mo and so on [1-3]. Several methods have been used to modify the structural and magnetic properties of M-type ferrites [1, 3, 4]. The magnetic properties of substituted $\text{Ba}_{1-x}\text{Sr}_x\text{Fe}_{12}\text{O}_{19}$, where Ba^{2+} gradually substitutes Sr^{2+} ions, have been studied and reported by other researchers [5-7]. These studies show that $\text{Ba}_{0.5}\text{Sr}_{0.5}\text{Fe}_{12}\text{O}_{19}$ sample possesses higher Curie temperature, $T_C \sim 510\ ^\circ\text{C}$, than that of $\text{BaFe}_{12}\text{O}_{19}$ ($502\ ^\circ\text{C}$) sample, which increases as Sr concentration increases. In addition, electrical characteristics (AC and DC) of the $\text{Ba}_x\text{Sr}_{1-x}\text{Fe}_{12}\text{O}_{19}$ compound have been studied [7]. The largest value for the dielectric constant (ϵ') corresponds to the $x = 0.0$ sample ($\epsilon_r' \gg 1300$) and it decreases, as

the Ba content increases, to around 100 for $x = 1.0$. Therefore, it seems interesting to investigate more cationic combination in this ferrite system [8]. Previous studies have shown that Zn-Ti cationic mixture produces materials with suitable characteristics for high-density magnetic recording [9, 10].

This paper reports structural and magnetic properties of the Zn-Ti substituted $(\text{BaSr})_{0.5}\text{M}$ -type hexaferrite, prepared by high energy milling.

Experiment

To synthesize $\text{Ba}_{0.5}\text{Sr}_{0.5}(\text{ZnTi})_x\text{Fe}_{12-2x}\text{O}_{19}$; BaCO_3 , SrCO_3 , Fe_2O_3 , ZnO , and TiO_2 (ACS reagent $\sim 98\%$ of purity, Aldrich Co.) were used as starting materials. The raw materials were charged in a Segvari Attritor mill together with several 9-mm steel balls. The powders were milled during 24 hours in air with an angular velocity of 400 rpm and 250 ml of benzene to avoid agglomeration at the mill bottom. The as-milled powders were

annealed at 1050 °C with a soaking time of 1.5 h.

To determine the crystalline structure of the prepared specimens, X-ray diffraction and Mössbauer spectroscopy studies were performed in an X' Pert Philips diffractometer using Cu-K α radiation and a Mössbauer spectrometer with γ -ray source of ^{57}Co embedded in a rhodium matrix, respectively. The magnetic properties at room temperature were measured using a Lake Shore 430 vibrating sample magnetometer and applying an external magnetic field up to 954.9 kA/m. The temperature dependence of the magnetic susceptibility, $\chi(T)$ was obtained using the bridge method in an alternating magnetic field of 421 A/m and 920 Hz. Finally, to obtain information on both morphology and

particle size, the $(\text{BaSr})_{0.5}\text{M}$ doped samples were observed employing a Philips XL 30 scanning electron microscope (SEM).

Results and Discussions

The X-ray diffraction patterns of Zn-Ti substituted $(\text{BaSr})_{0.5}\text{M}$ samples, obtained at different sample preparation stages, are shown in Fig.1. The patterns of all samples (as-milled) after milling for 24 hours show broadened diffraction peaks corresponding to Fe_2O_3 hematite phase. Magnetoplumbite phase was formed for all substituted samples ($x = 0$ to 0.6) after being annealed at 1050 °C; no other secondary phases were detected, at least within the errors inherent to this technique.

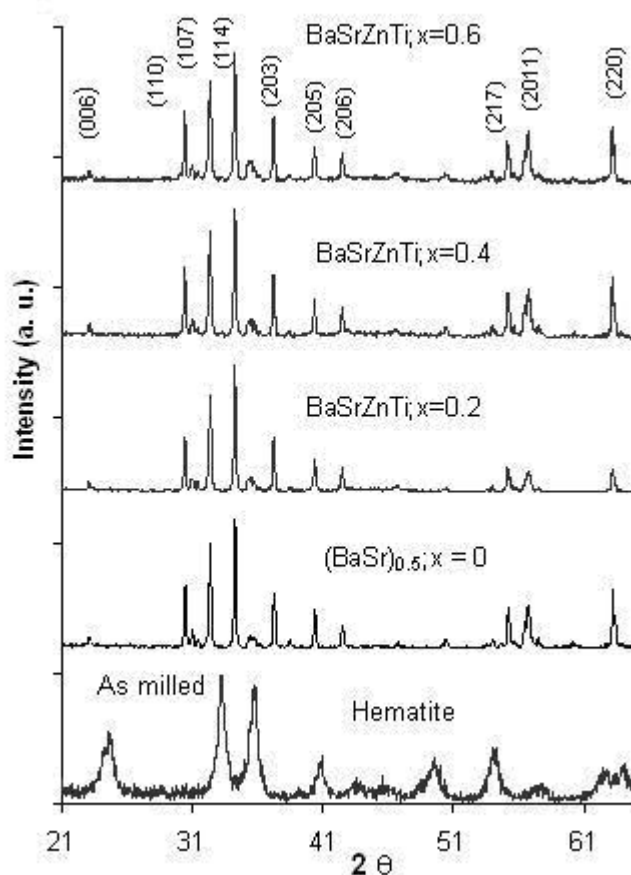


Fig. 1: X-ray diffraction patterns for all prepared samples.

Room temperature Mössbauer spectra for $\text{Ba}_{0.5}\text{Sr}_{0.5}(\text{ZnTi})_x\text{Fe}_{12-2x}\text{O}_{19}$ samples with $x = 0.0, 0.2, 0.4$ and 0.6 are shown in Fig.2. These measurements revealed that at low substitutions, Ti^{4+} ions substitute Fe^{3+} ions

on the $4f_2$ octahedral site, and the Zn^{2+} ions substitute them on the tetrahedral $4f_1$ site. At higher concentrations other iron positions are replaced also, like 2a octahedral sites by Ti^{4+} ions and 2b positions by Zn^{2+} ions [10].

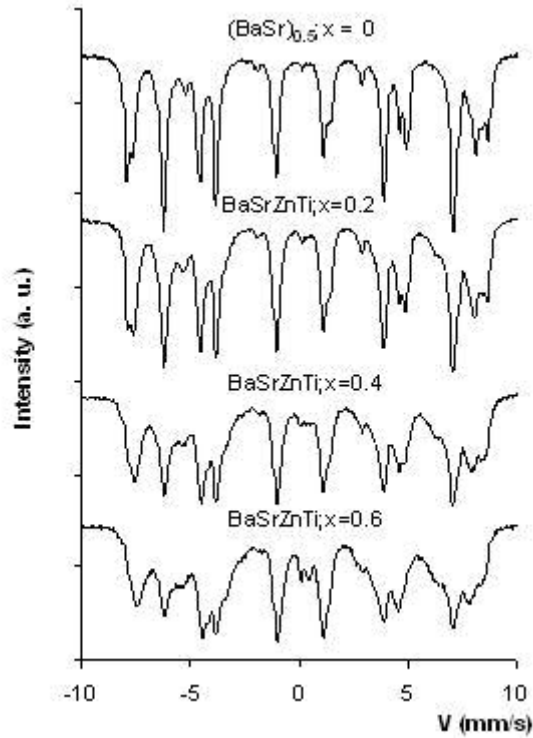


Fig. 2: Mössbauer spectra of Zn-Ti substituted $(\text{BaSr})_{0.5}\text{M}$ ferrites.

The results of the temperature dependence of the initial susceptibility of $\text{Ba}_{0.5}\text{Sr}_{0.5}(\text{ZnTi})_x\text{M}$ ferrites is shown in Fig.3. It can be observed, that at room temperature the susceptibility, χ , increases with the substitution level. These curves can be also used as quality test for some preparation techniques. From the sample with $x = 0.0$ it could be concluded that no other secondary phase was nucleated for all synthesized mixtures. On the other hand, Hopkinson peak appears near Curie point T_C and falls from a relatively high value to near zero. This drop provides a possibility of homogeneity in sample chemical composition. This peak value also gives information about quantity percentage of the ordered single-phase structure with particles smaller than $1\mu\text{m}$. In addition, $x = 0.0$ sample exhibits a curve that roughly approaches the theoretical behavior of hexaferrite initial magnetic susceptibility as a function of temperature. Besides, it could be concluded that T_C for all substituted samples were almost not affected by the increase in x , (diminution $\sim 2\%$).

The magnetic properties behavior of Zn-Ti-substituted $(\text{BaSr})_{0.5}\text{M}$ obtained by vibrating sample magnetometry is shown in Fig.4. Both, the intrinsic coercivity, H_{ci} , and the remanent magnetization, M_r , decreased as the substitution took place, while the saturation magnetization, M_s , remained almost constant (diminution $\sim 9\%$). H_{ci} , decreased from 389.92 down to 171.88 kA/m, which represents a 56% drop, whilst M_r registered a fall of $\sim 17\%$. The fast reduction of H_{ci} is related to the reduction of the magnetocrystalline anisotropy field, H_a , which has been attributed to the cation preference for the bipyramidal site, 2b and octahedral site $4f_2$, which possess the largest contribution to H_a in BaM. On the other hand, the small diminution of M_s and M_r can also be explained by the gradual break down of the magnetic ordering, due to the disappearance of some super exchange interactions when the iron ions are substituted for other diamagnetic or paramagnetic cations.

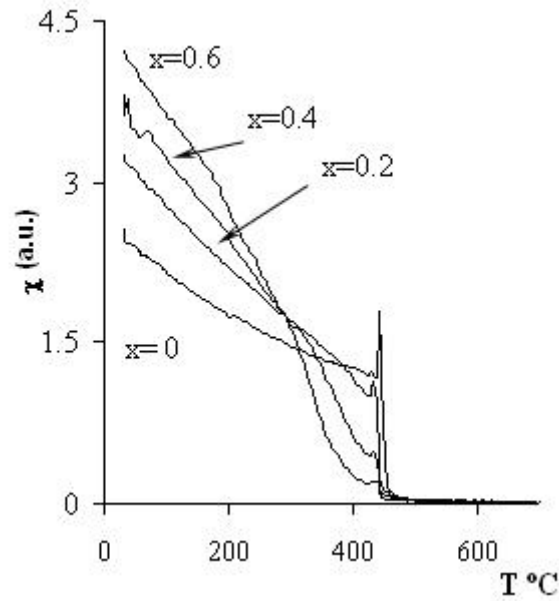


Fig. 3: Temperature dependence of the magnetic susceptibility of $\text{Ba}_{0.5}\text{Sr}_{0.5}(\text{ZnTi})_x\text{Fe}_{12-2x}\text{O}_{19}$.

In Fig.5 the micrographs taken by SEM for the pure $(\text{BaSr})_{0.5}\text{M}$ ferrite and $x = 0.6$ substituted ferrite are shown. It can be seen that all particles of the samples are nearly

hexagonal platelet in shape and have a wide spread in particle size. However, it is clear that the particle size is much below $1\ \mu\text{m}$,

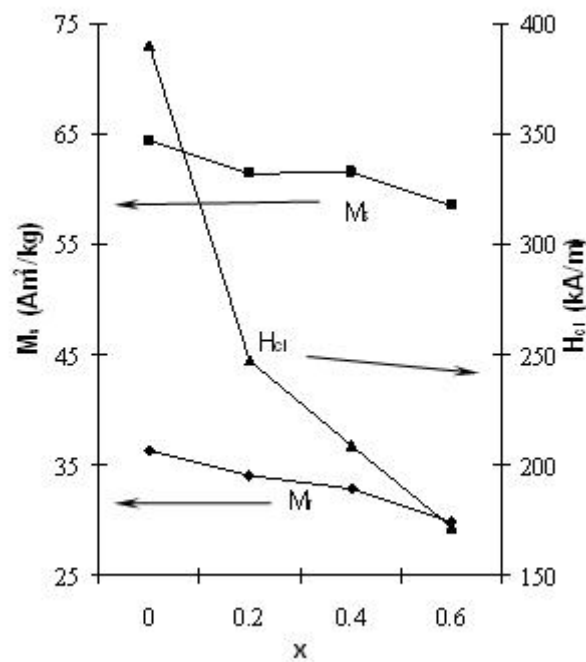


Fig. 4: Magnetic properties behavior of all synthesized samples as the substitution level increased.

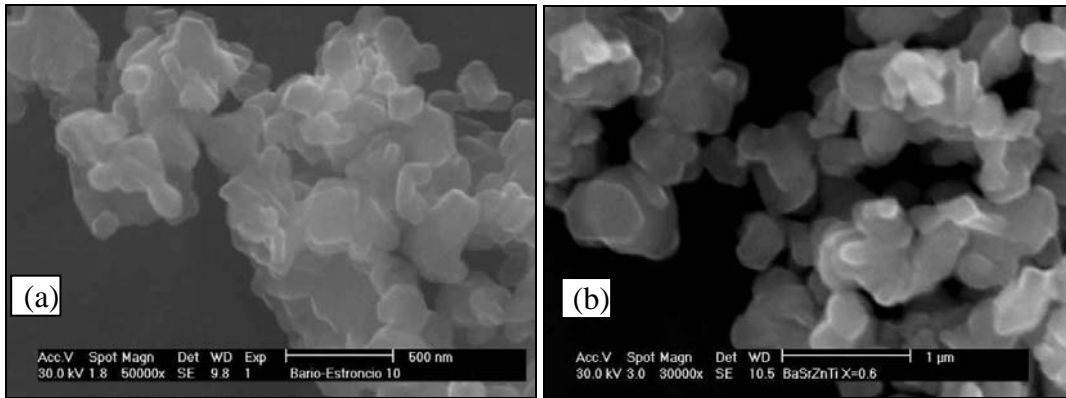


Fig. 5: SEM micrographs show particle size and morphology for samples $\text{Ba}_{0.5}\text{Sr}_{0.5}(\text{ZnTi})_x\text{Fe}_{12-2x}\text{O}_{19}$.
a) $x = 0$, b) $x = 0.6$.

Conclusions

This work has shown that it was possible to synthesize $\text{Ba}_{0.5}\text{Sr}_{0.5}\text{M}$ hexaferrite substituted with Zn^{2+} - Ti^{4+} ions by mechanical milling. The magnetic ordering was reduced somewhat (~2%) for all levels of substitution. Changing the substitution ratio x , the coercivity could be easily controlled without a significant reduction of M_s . Magnetic susceptibility measurements have shown that with the increase of x , χ at room temperature increases, which is believed to have a relation with the disappearance of some superexchange interactions. The micrographs of Fig. 5 indicate that the particle size of the samples is much below $1 \mu\text{m}$. The studied samples may exhibit promising magnetic and dielectric properties.

Acknowledgements

We would like to thank both CONACyT - México and VEGA - Slovak Republic (Grant No. 1/3096/06, 1/3189/06 and EU/INTAS/07) for given support to carry out this work. Special thanks to Ing. Tóth for Mössbauer measurements.

References

- [1] Darja Lisjak, Vlado B. Bregar and Miha Drofenik. (2007). *J. Magn. Magn. Mater.* 310, 2558-2560.
- [2] Z. Haijun, L. Zhichao, M. Chengliang, Y. Xi, Z. Liangying and W. Mingzhong. (2002). *Mater. Sci. Eng. B* 96, 289.
- [3] K. G. Rewatkar, N. M. Patil, S. Jaykumar, D. S. Bhowmick, M. N. Giriya and C. L. Khobragade. (2007). *J. Magn. Magn. Mater.* 316, 19-22.
- [4] H. C. Fang, Z. Yang, C. K. Ong, Y. Li and C. S. Wang. (1998). *J. Magn. Magn. Mater.* 187, 129.
- [5] S. Yong An, S. Won Lee, S. Wha Lee and Ch. Sung Kim. (2002). *J. Magn. Magn. Mater.* 242-245, 413.
- [6] S. A. Palomares-Sánchez, S. Ponce-Castañeda and M. Mirabal-García. (1999). *Rev. de Met.* 35 (3) 143.
- [7] A. Huanosta-Tera, R. de Lira-Hueso, O. Pérez-Orta, S. A. Palomares-Sánchez, S. Ponce-Castaneda and M. Mirabal-García. (2000). *J. Scr. Mater.* 42 (6) 603.
- [8] Charanjeet Singh, S. Bindra Narang, I. S. Hudiara, Yang Bai and Faride Tabatabaei. (2008). *Mater. Research Bulletin*, 43, 176-184.
- [9] Q. Fang, Y. Lui, P. Yin and X. Li. (2001). *J. Magn. Magn. Mater.* 234, 366.
- [10] A. González-Angeles, G. Mendoza-Suárez, A. Grusková, M. Papánová. and J. Sláma. (2005). *Mater. Lett.* 59, 26

Partial Substitution Effects on the Structure and Electrical Properties of the High Temperature Superconducting System



A. El Ali (Al-Dairy)^a, A. D. Alazawi^b, Y. A. Hamam^a and K. Khasawinah^a

^a *Physics Department, Yarmouk University, Irbid, Jordan*

^b *Department of Physics, University of Mousl, Iraq*

Received on: 6/9/2007; Accepted on: 13/3/2008

Abstract: The partial substitution effects on the structure and electrical properties of the high temperature $\text{Bi}_{2-x}\text{Tl}_x\text{Ba}_{2-y}\text{Sr}_y\text{Ca}_2\text{Cu}_3\text{O}_{10+\delta}$ superconducting compounds have been investigated with $x=0.00, 0.05, 0.10, 0.20$ and $y=0.0, 0.1, 0.2, 0.3$. X-ray diffraction studies showed that the structure was tetragonal with $a=b=5.43\text{\AA}$, $c=34.13\text{\AA}$ for $x=0, y=0$. The structure almost remained tetragonal for all x values with $y=0$, and the c -parameter increased only for $x=0.05$ and then a decrease in the c -parameter with increasing x value was observed. On the other hand, for $x=0$ and $y=0.1, 0.2, 0.3$ the structure was tetragonal with a slight decrease in the lattice parameters with increasing y . There was an observed change to orthorhombic phase with increasing both x and y at the same time.

The critical temperature was very sensitive to the thallium content x , in the absence of strontium, as it increased to 128K for small x but decreased noticeably with increasing x value. A similar behavior was observed for Sr content. However a large enhancement in the critical temperature was observed in the presence of lower concentrations of both thallium and strontium. Finally, the increase in the volume of the lattice or the oxygen content is associated with higher critical temperature values.

Key Words: HTSC, Partial Substitution, Crystal Structure, BSCCO, TBCCO.

Introduction

The discovery of superconductivity above 77K in Bi-Sr-Cu-O compound has been reported in [1,2]. The discovery of the high temperature superconducting system, Tl-Ba-Cu-O, was initially overshadowed by the discovery of the Bi-Ca-Sr-Cu-O system [3,4,5]. Extensive studies by several groups were carried out to study the structural, electrical, and magnetic properties of the Bi-based or Tl-based superconducting systems [6-12]. Some other workers studied the effects of doping these compounds with certain elements.[13-20]. However, many scientists concentrated on the Bi-based superconducting system since Tl is poisonous and needs special careful treatment. It was reported that doping the superconducting phases $\text{Tl}_2\text{Ba}_2\text{CaCu}_2\text{O}_8$ (TI-

2212) and $\text{Tl}_2\text{Ba}_2\text{Ca}_2\text{Cu}_3\text{O}_{10}$ (TI-2223) with Pb or Li improved only their critical currents, and when the superconducting phases $\text{Bi}_2\text{Sr}_2\text{CaCu}_2\text{O}_x$ (Bi-2212) and $\text{Bi}_2\text{Sr}_2\text{Ca}_2\text{Cu}_3\text{O}_x$ (Bi-2223) were doped with Pb or Li, their critical temperatures and critical currents were improved [19-22]. It was also reported that the addition of specific small amounts of boron (B) to Tl-based superconductors increased the superconducting phase TI-2223 and improved the critical temperature of the samples, while higher amounts of B eliminated TI-2223 phase and reduced the TI-2212 phase [23]. Furthermore, it was reported that fluorine addition to Tl-based compounds affected their properties drastically [24].

Very few researchers worked on systems containing both Bi and Tl elements at the same time [21,22]. Epitaxial films of Tl-Bi-Sr-Ba-Ca-Cu-O were prepared using laser ablation and showed critical temperatures between 106-110K and critical currents at 77K of about 10^5 A/cm². Due to their high superconducting transition temperatures and high irreversible magnetic fields, Tl-based and Bi-based superconductors are very promising materials for making magnetic tapes above 77K.

This work aims at studying further superconducting samples containing both Bi and Tl. We have doped $\text{Bi}_2\text{Ba}_2\text{Ca}_2\text{Cu}_3\text{O}_{10}$ (Bi-2223 phase) with different amounts of Tl and Sr. The effect of this partial substitution of Tl and Sr on the structure and the electrical properties of the superconducting system $\text{Bi}_{2-x}\text{Tl}_x\text{Ba}_{2-y}\text{Sr}_y\text{Ca}_2\text{Cu}_3\text{O}_{10+\delta}$, with $x=0, 0.05, 0.1, 0.2$, and $y=0, 0.1, 0.2, 0.3$ will be investigated in this paper.

Experimental Technique

The solid state reaction technique was used to prepare the superconducting samples $\text{Bi}_{2-x}\text{Tl}_x\text{Ba}_{2-y}\text{Sr}_y\text{Ca}_2\text{Cu}_3\text{O}_{10+\delta}$ from appropriate amounts of the high purity oxides Bi_2O_3 , Tl_2O_3 , BaCO_3 , CaCO_3 , $\text{Sr}(\text{NO}_3)_2$, and CuO as starting materials. The high purity powders were mixed well and loaded in an alumina crucible which was then placed in a furnace. The temperature of the furnace was raised to 850 °C at a rate of 120 °C/hr. This material was sintered at 850 °C for 12 hrs then cooled down at a rate of 30 °C/hr in air to room temperature. The same heating process was repeated but with a flow of oxygen. The resulting material was then ground and pressed into 1gm pellets of approximately 12mm diameter and 1.2mm thickness. Fig.1 shows the annealing process carried on these pressed pellets in oxygen environment.

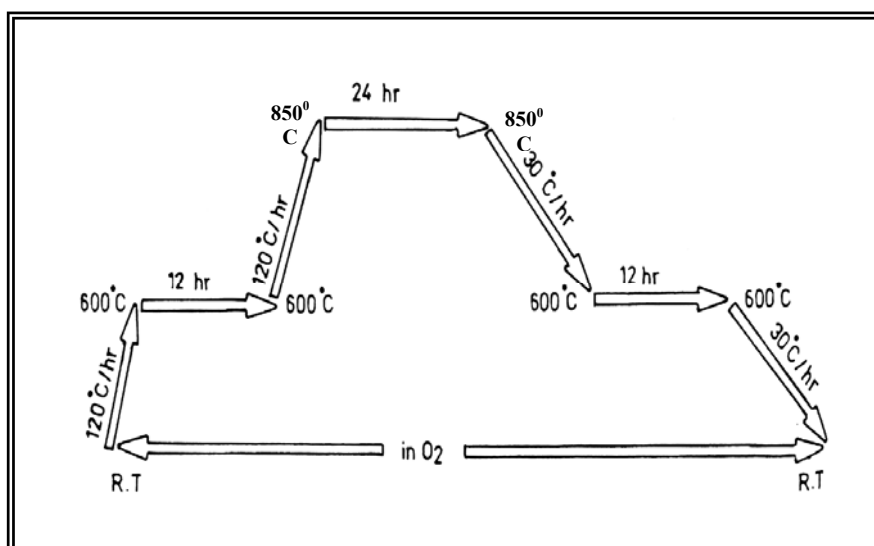


Fig. 1: Annealing process of pressed pellets in O₂

Standard four-probe-method was used to measure the resistivity (ρ) versus temperature (T). For each sample, we plotted resistivity (ρ) versus temperature (T) and the critical temperature (T_c) was determined. We have used the 50% rule to find T_c and not the onset value nor the T_c value for zero resistance. The oxygen content in each sample was measured by using iodometric titration method. Detailed experimental work for the determination of (T_c) and the oxygen content are described in references [12,15].

X-ray diffraction patterns for the $\text{Bi}_{2-x}\text{Tl}_x\text{Ba}_{2-y}\text{Sr}_y\text{Ca}_2\text{Cu}_3\text{O}_{10+\delta}$ samples at room temperature were obtained using Phillips X-ray diffractometer with CuK_α source and

$\lambda=1.5418$ Å. Using these patterns and a computer program the lattice parameters were then calculated.

Results and Discussion

Using the X-ray data obtained, the structures of $\text{Bi}_{2-x}\text{Tl}_x\text{Ba}_{2-y}\text{Sr}_y\text{Ca}_2\text{Cu}_3\text{O}_{10+\delta}$, high temperature superconducting samples prepared at 850°C were studied. The structural calculations of the lattice parameters were carried with the help of a computer program written in BASIC. Fig.2 shows x-ray diffraction pattern of the Bi-2223 phase ($x=0, y=0$). It shows the existence of a single tetragonal phase with lattice parameters $a=b=5.43\text{Å}$ and $c=34.13\text{Å}$.

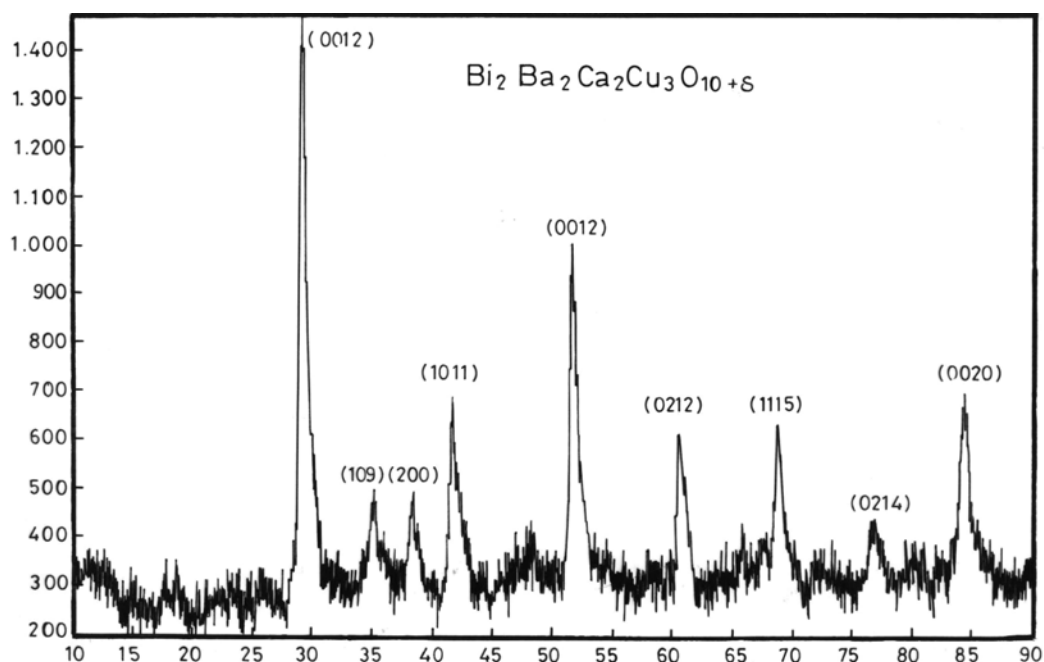


Fig (2): X – ray diffraction pattern of $\text{Bi}_2\text{Ba}_2\text{Ca}_2\text{Cu}_3\text{O}_{10+\delta}$ high temperature superconductor

Figures (3), (4), and (5) show x-ray diffraction patterns for the values: i) $y=0$ and $x=0.05, 0.1, 0.2$, ii) $x=0$, and $y=0.1, 0.2, 0.3$, iii) $x=0.05$ and $y=0.1, 0.2, 0.3$ respectively. From Fig.3, it was noticed that peak intensity decreases with increasing the value of the Tl content and small peaks like (0024) disappeared. In Table I we present the calculated values of lattice parameters. It is noticed that when no Sr is added and when Tl is partially substituted for Bi, with $x = 0.05, 0.1$, the structure of the samples remained tetragonal with a slight increase in the c-parameter with decreasing x-values. The maximum increase in the c-parameter was up to 34.81\AA for $x=0.05$. On the other hand, when $x=0.2$, the structure changed from tetragonal to orthorhombic phase with lattice parameters $a=5.40\text{\AA}$, $b=5.21\text{\AA}$, $c=30.13\text{\AA}$.

Fig.4 shows the x-ray pattern for the samples when only Sr is substituted for Ba

with $y=0.1, 0.2, 0.3$ and $x=0$. The structure for samples with all y values remained tetragonal. It is noticed that there was a slight shift in the original peaks associated with the slight increase in the c-parameter. The maximum value calculated for the c-parameter was when $y=0.1$ and the lattice parameters were $a=b\approx 5.40\text{\AA}$ and $c=34.72\text{\AA}$.

From Fig.5 and Table I, the structure of the samples changed in a different manner when Tl is substituted for Bi together with Sr substituted for Ba. For the samples with $x=0.05$ and $y=0.1$ the structure was tetragonal with $a=b=5.46\text{\AA}$, but for $x=0.05$ and $y=0.2$ or $x=0.05$ and $y=0.3$ new peaks appeared which could be due to the formation of new phases of CuO and SrO. However, when $x=0.1$ and $y=0.1$ or $x=0.2$ and $y=0.3$, the structure of the samples was clearly orthorhombic.

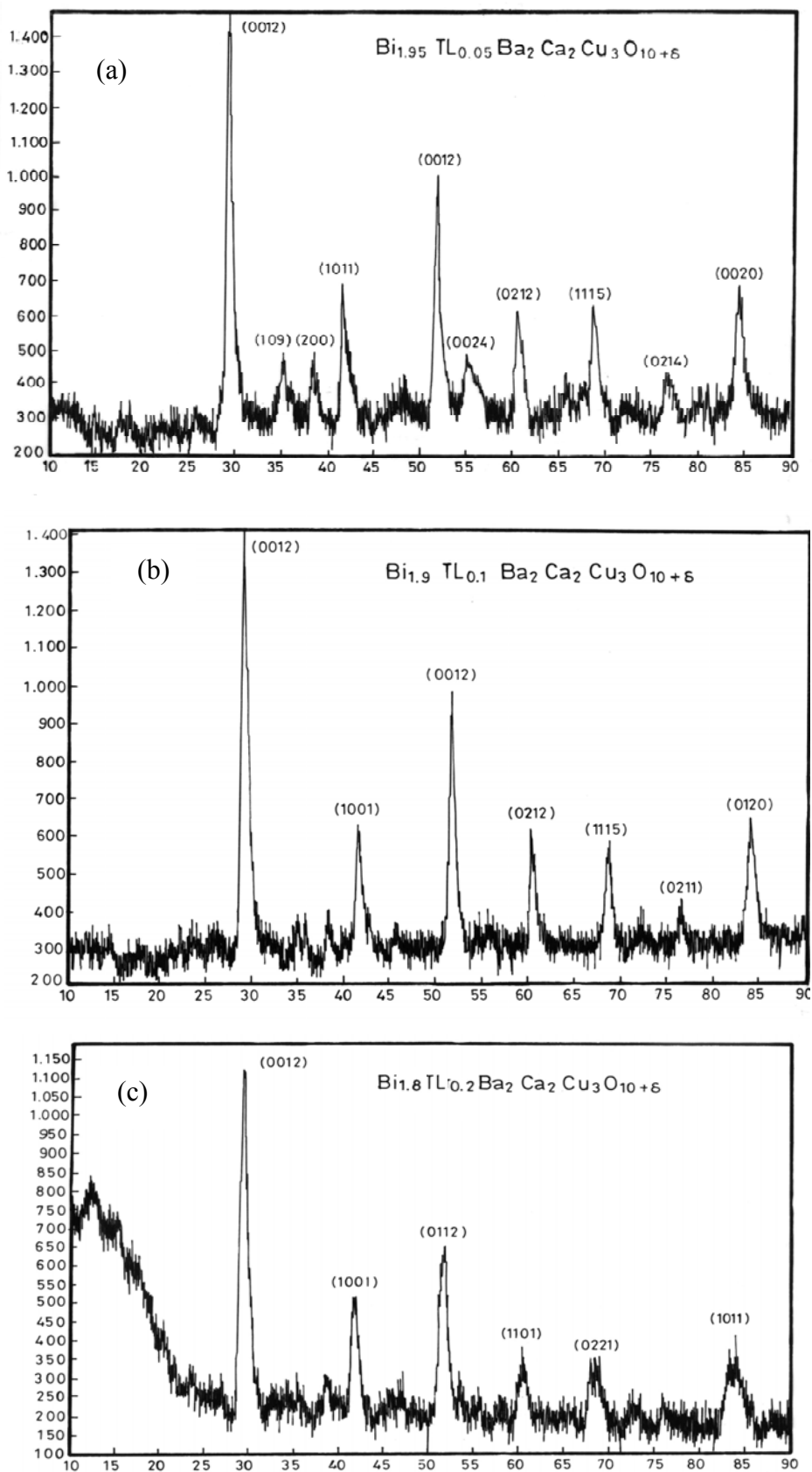


Fig (3): X – ray diffraction patterns for $\text{Bi}_{2-x}\text{Tl}_x\text{Ba}_2\text{Ca}_2\text{Cu}_3\text{O}_{10+\delta}$ system for $y=0$ and: $x = 0.05$ (a), $x = 0.1$ (b), $x=0.2$ (c).

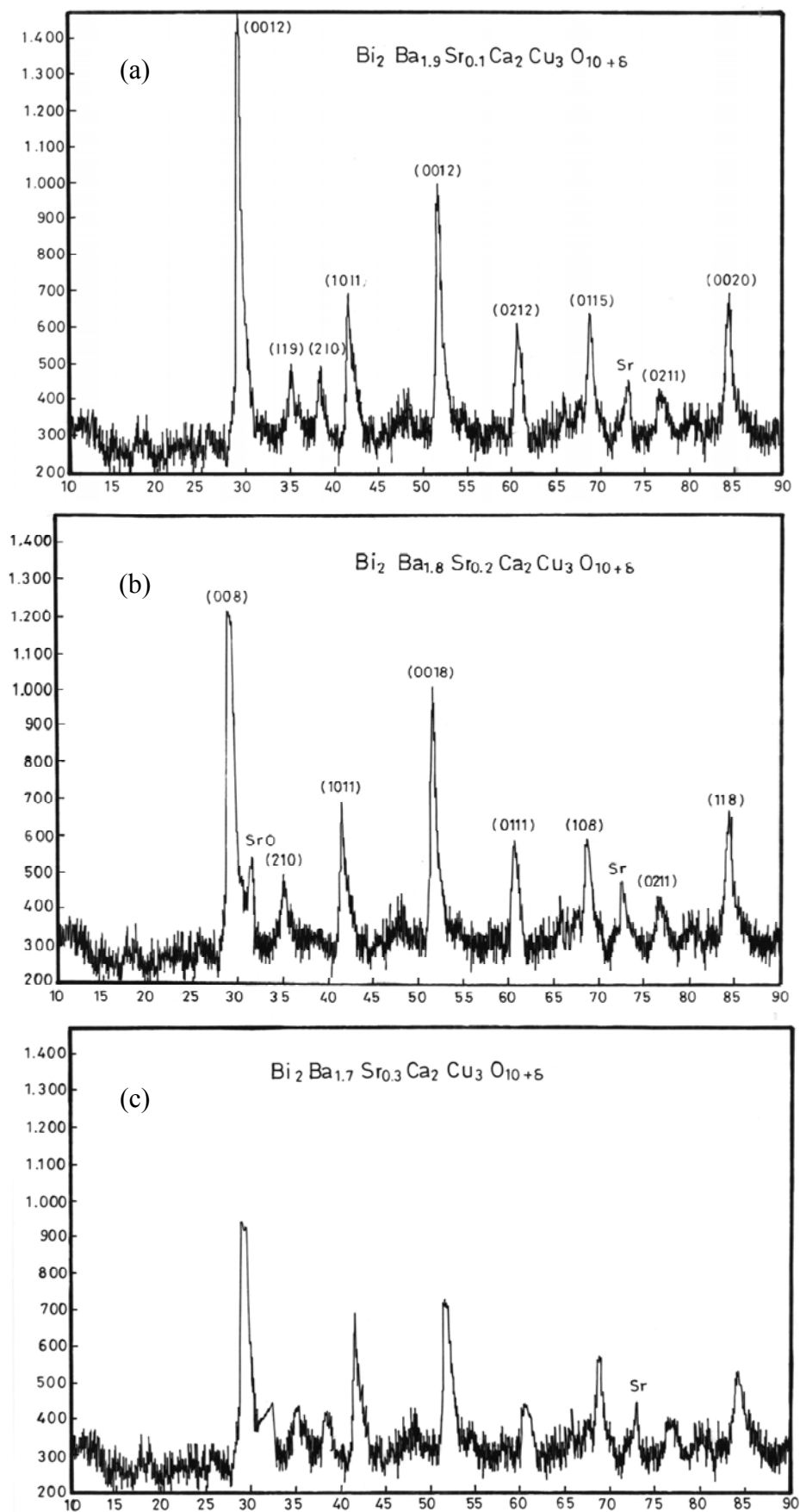


Fig (4): X – ray diffraction patterns for $\text{Bi}_2\text{Ba}_{2-y}\text{Sr}_y\text{Ca}_2\text{Cu}_3\text{O}_{10+\delta}$ high temperature superconductor for $x = 0$, and: $y = 0.1$ (a), $y = 0.2$ (b), $y = 0.3$ (c).

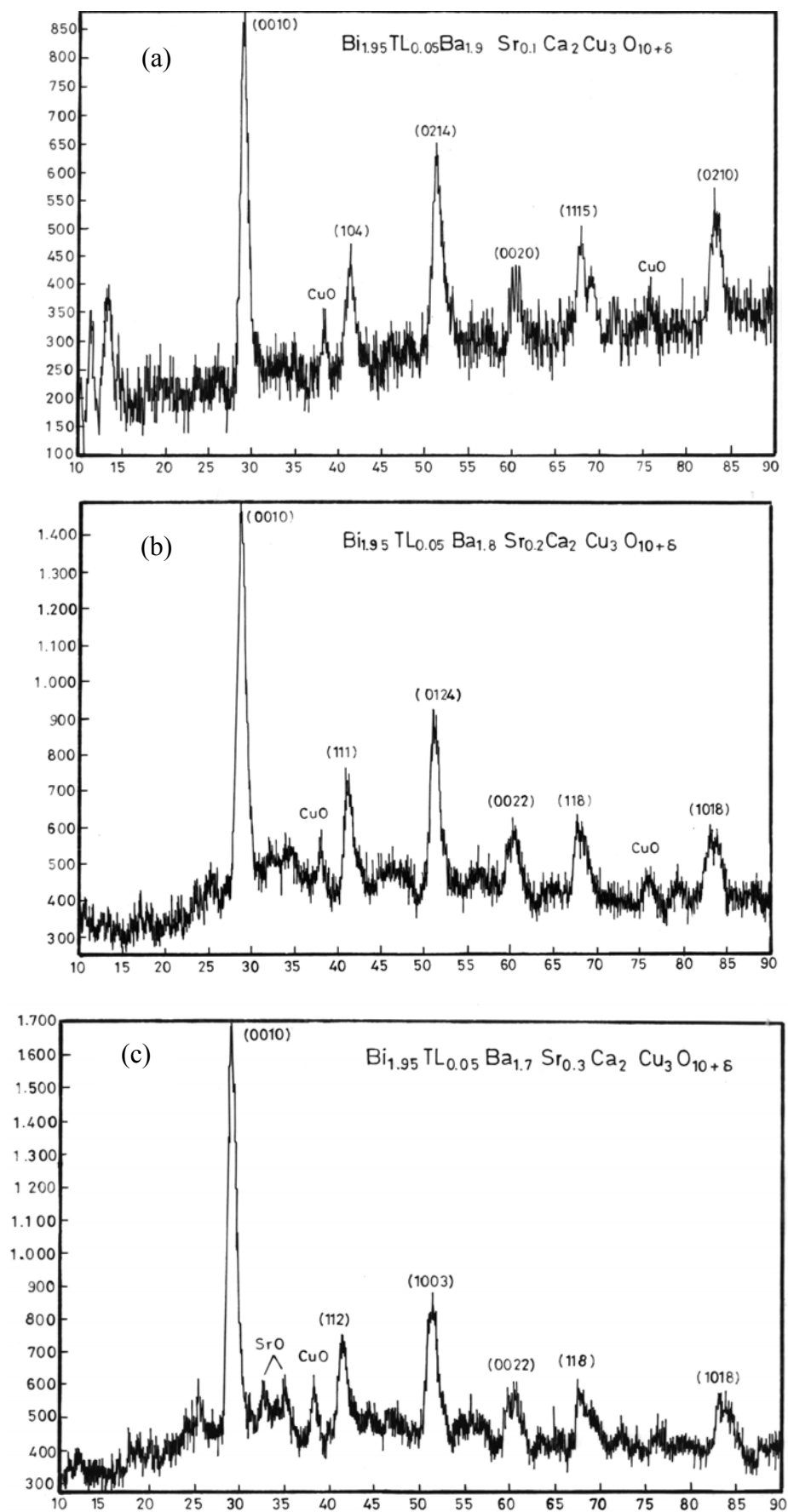


Fig (5): X – ray diffraction patterns for $\text{Bi}_{2-x}\text{Tl}_x\text{Ba}_{2-y}\text{Sr}_y\text{Ca}_2\text{Cu}_3\text{O}_{10+\delta}$ system for: a ($x = 0.05, y = 0.1$), b ($x = 0.05, y = 0.2$), and c ($x = 0.05, y = 0.3$).

Table I: Lattice parameters of the superconducting system $\text{Bi}_{2-x}\text{Tl}_x\text{Ba}_{2-y}\text{Sr}_y\text{Ca}_2\text{Cu}_3\text{O}_{10+\delta}$

Sample	Lattice Parameters		
	a (Å)	b (Å)	c (Å)
$\text{Bi}_2\text{Ba}_2\text{Ca}_2\text{Cu}_3\text{O}_{10+\delta}$	5.43	5.43	34.13
$\text{Bi}_{1.95}\text{Tl}_{0.05}\text{Ba}_2\text{Ca}_2\text{Cu}_3\text{O}_{10+\delta}$	5.43	5.43	34.81
$\text{Bi}_{1.9}\text{Tl}_{0.1}\text{Ba}_2\text{Ca}_2\text{Cu}_3\text{O}_{10+\delta}$	5.42	5.42	30.18
$\text{Bi}_{1.8}\text{Tl}_{0.2}\text{Ba}_2\text{Ca}_2\text{Cu}_3\text{O}_{10+\delta}$	5.40	5.21	30.13
$\text{Bi}_2\text{Ba}_{1.9}\text{Sr}_{0.1}\text{Ca}_2\text{Cu}_3\text{O}_{10+\delta}$	5.44	5.44	34.72
$\text{Bi}_2\text{Ba}_{1.8}\text{Sr}_{0.2}\text{Ca}_2\text{Cu}_3\text{O}_{10+\delta}$	5.41	5.41	30.18
$\text{Bi}_2\text{Ba}_{1.7}\text{Sr}_{0.3}\text{Ca}_2\text{Cu}_3\text{O}_{10+\delta}$	5.41	5.41	30.01
$\text{Bi}_{1.95}\text{Tl}_{0.05}\text{Ba}_{1.9}\text{Sr}_{0.1}\text{Ca}_2\text{Cu}_3\text{O}_{10+\delta}$	5.46	5.46	34.88
$\text{Bi}_{1.9}\text{Tl}_{0.1}\text{Ba}_{1.9}\text{Sr}_{0.1}\text{Ca}_2\text{Cu}_3\text{O}_{10+\delta}$	5.28	5.22	31.18
$\text{Bi}_{1.8}\text{Tl}_{0.2}\text{Ba}_{1.7}\text{Sr}_{0.3}\text{Ca}_2\text{Cu}_3\text{O}_{10+\delta}$	5.18	5.26	30.18

The measurements of resistivity versus temperature for samples with only Tl substituted for Bi; $x=0.00, 0.05, 0.10,$ and $0.20,$ are shown in Fig.6. It was noticed that the critical temperature initially increased from 123K to 128K when x was increased from 0 to 0.05, and T_c started to decrease with increasing the content of the thallium, $x=0.10$ and 0.20 . In Fig.7, we show the resistivity versus temperature for samples

with only Sr partially substituted for Ba. Fig.8 shows resistivity versus temperature when both Tl and Sr are added for the smallest value of Tl, $x=0.05,$ and with different amounts of Sr, $y=0.1, 0.2,$ and 0.3 . Figures (7) and (8) show a clear drop in the critical temperature with increasing the Sr. The values of the critical temperatures, $T_c,$ determined from the Figures (6), (7), and (8) are summarized in table II.

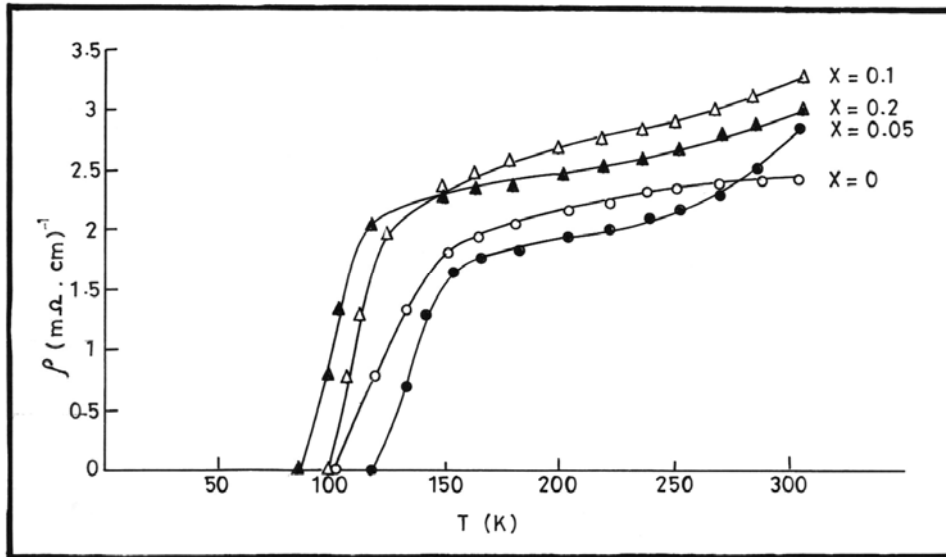


Fig (6): The resistivity versus temperature for the $\text{Bi}_{2-x}\text{Tl}_x\text{Ba}_2\text{Ca}_2\text{Cu}_3\text{O}_{10+\delta}$ superconductors with $x = 0, 0.05, 0.1, 0.2$.

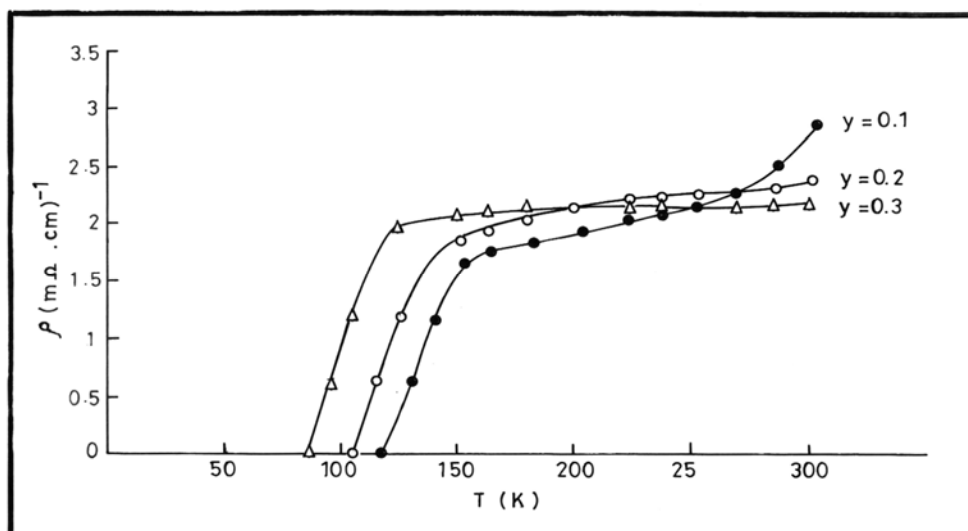


Fig (7): The resistivity versus temperature for $\text{Bi}_2\text{Ba}_{2-y}\text{Sr}_y\text{Ca}_2\text{Cu}_3\text{O}_{10+\delta}$ high temperature superconductor with $y = 0.1, 0.2, 0.3$.

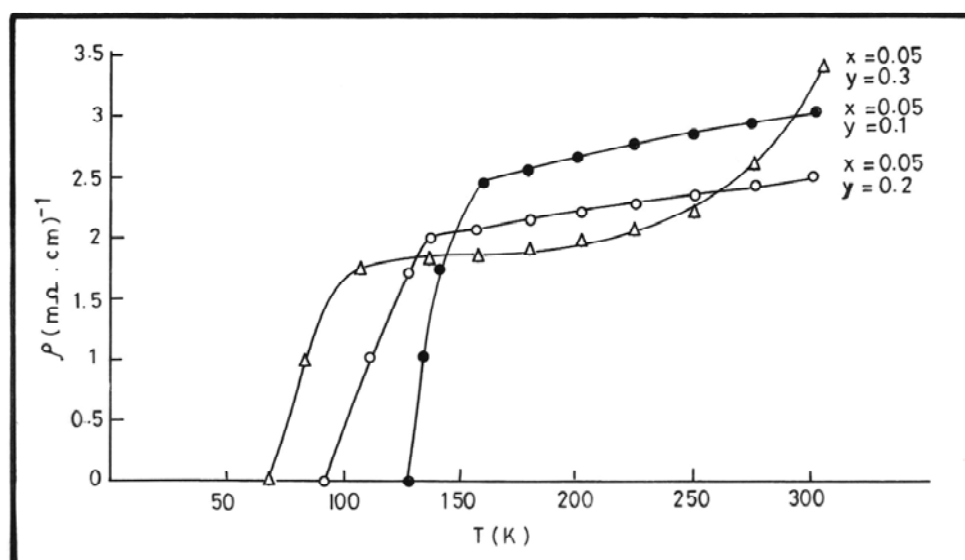


Fig (8): The resistivity versus temperature for $\text{Bi}_{2-x}\text{Tl}_x\text{Ba}_{2-y}\text{Sr}_y\text{Ca}_2\text{Cu}_3\text{O}_{10+\delta}$ for $x = 0.05$ and $y = 0.1, 0.2, 0.3$.

Table II: Critical temperatures measured and Oxygen contents for the superconducting system $\text{Bi}_{2-x}\text{Tl}_x\text{Ba}_{2-y}\text{Sr}_y\text{Ca}_2\text{Cu}_3\text{O}_{10+\delta}$

Sample	Critical temperature T_c (°K)	Oxygen content $10+\delta$
$\text{Bi}_2\text{Ba}_2\text{Ca}_2\text{Cu}_3\text{O}_{10+\delta}$	123	10.22
$\text{Bi}_{1.95}\text{Tl}_{0.05}\text{Ba}_2\text{Ca}_2\text{Cu}_3\text{O}_{10+\delta}$	128	10.28
$\text{Bi}_{1.9}\text{Tl}_{0.1}\text{Ba}_2\text{Ca}_2\text{Cu}_3\text{O}_{10+\delta}$	108	10.21
$\text{Bi}_{1.8}\text{Tl}_{0.2}\text{Ba}_2\text{Ca}_2\text{Cu}_3\text{O}_{10+\delta}$	100	10.18
$\text{Bi}_2\text{Ba}_{1.9}\text{Sr}_{0.1}\text{Ca}_2\text{Cu}_3\text{O}_{10+\delta}$	125	10.26
$\text{Bi}_2\text{Ba}_{1.8}\text{Sr}_{0.2}\text{Ca}_2\text{Cu}_3\text{O}_{10+\delta}$	120	10.18
$\text{Bi}_2\text{Ba}_{1.7}\text{Sr}_{0.3}\text{Ca}_2\text{Cu}_3\text{O}_{10+\delta}$	110	10.14
$\text{Bi}_{1.95}\text{Tl}_{0.05}\text{Ba}_{1.9}\text{Sr}_{0.1}\text{Ca}_2\text{Cu}_3\text{O}_{10+\delta}$	140	10.38
$\text{Bi}_{1.9}\text{Tl}_{0.1}\text{Ba}_{1.9}\text{Sr}_{0.1}\text{Ca}_2\text{Cu}_3\text{O}_{10+\delta}$	112	10.26
$\text{Bi}_{1.8}\text{Tl}_{0.2}\text{Ba}_{1.7}\text{Sr}_{0.3}\text{Ca}_2\text{Cu}_3\text{O}_{10+\delta}$	95	10.21

It was observed that the critical temperature was enhanced drastically for small amounts of Tl and Sr and decreased significantly with increasing Sr content. The decrease in T_c values could be attributed to the change in structure from tetragonal to orthorhombic phase. The increase in T_c could mean that there was an increase in the mobility of electrons in the b-direction of Cu-O plane. Finally it is noticed that increasing the volume of the lattice cell, which could be caused by growth of a larger number of Cu-O layers in the unit cell, can lead to an increase in T_c .

The oxygen content in each sample was measured by using iodometric titration method and results are shown in Table II. It is noticed, from Table II, that higher critical temperatures are associated with higher values of oxygen content and the increase in the oxygen content might affect the electronic behavior by shifting the Fermi level.

Conclusion

The partial substitution effects on the structure & electrical properties of $\text{Bi}_{2-x}\text{Tl}_x\text{Ba}_{2-y}\text{Sr}_y\text{Ca}_2\text{Cu}_3\text{O}_{10+\delta}$ superconducting compounds have been investigated. X-ray diffraction studies showed that the structure is tetragonal with $a=b=5.43\text{\AA}$, $c=34.13\text{\AA}$ for

$x=0$, $y=0$. The structure almost remained tetragonal for all x values when no Sr was added. The c -parameter increased only for $x=0.05$ and then a decrease in the c -parameter with increasing x value was observed. On the other hand, for $x=0$ and $y=0.1, 0.2, 0.3$ the structure was tetragonal with a slight decrease in the lattice parameters with increasing y . There was an observed change of structure to orthorhombic with increasing the content of both Tl and Sr resulting in a drop in T_c .

The critical temperature was very sensitive to the Tl content in the absence of Sr since it increased to 128K but decreased noticeably with increasing x value. A similar behavior was observed for Sr content. However a large enhancement in the critical temperature was observed in the presence of lower concentrations of both Tl and Sr. Finally it is noticed that the increase in the volume of the lattice, which could be caused by growth of a larger number of Cu-O layers in the unit cell, and the increase of the oxygen content are associated with higher critical temperatures.

Acknowledgement

This work was supported by Yarmouk University, Deanship of Graduate studies and Research through grant 18/2006.

References

- [1] C. Michel, M. Hevicu, M. Borel, F. Grantin and B. Reveau. (1987). *Z. phys.* 421. B68.
- [2] M. Meada, Y. Teanaka, M. Fukutomi and A. Asano. (1988). *Jpn. J. Appl. Phys.* 27, L209.
- [3] Z. Sheng and A. Hermann. (1988). *Nature*, 33255.
- [4] M. A. Subramanian, C. C. Torardi, J. C. Calabrese, J. Gopalakrishnan, K. J. Morrissey, T. R. Askew, R. B. Flippen, U. Chowdhry and A. W. Sleight. (1988). *Science*, 239 (4843).
- [5] M. A. Subramanian, C. C. Torardi, P. L. Gopalakrishnan, J. Gai., J. C. Calabrese, T. R. Askew, Flippen and A. W. Sleight. (1988). *Science*, 242 (4876).
- [6] C. Chu, J. Bechtold, P. Hor and Y. Xuc. (1988). *Phys. Rev. Lett.* 941, 60.
- [7] R. Hazen and Y. Sun. (1988). *Phys. Rev. Lett.* 881, 60 .
- [8] C. Rao. (1988). *Chemistry of oxide superconductors*, Sci. publi. oxford.
- [9] M. A. Subramanian and K. Morrissey. (1990). *Mod. Phys. Lett.* 95, B4 .
- [10] S. Putilin, E. Antipov, O. Chmaissem and M. Marezio. (1993). *Nature*, 362, 226 .
- [11] J. Li, S. Ding, J. Zhu and Y. Wang. (1995). *J. Appl. Phys.* 77, 3698 .
- [12] A. Asab, A. Armstrong, I. Gameson and P. Edwards. (1995). *Physica. C* 255. 180.
- [13] C. C. Torardi, M. A. Subramanian, J. C. Calabrese, J. Gopalakrishnan, K. J. Morrissey, T. R. Askew, R. B. Flippen, U. Chowdhry and A. W. Sleight. (1988). *Science*, 240 (4852) [14].
- [14] W. Wang, G. Xiong, X. Tang and Z. Hong. (1993). *Physica C*210.
- [15] Jr., C. P. Poole, H. C. Farach and R. J. Creswick. (1995). *Superconductivity*, Academic Press Inc., San Diego, California, USA.
- [16] J. Schwartz and S. Wu. (1991). *Physica C*190.
- [17] M. Fujiwara, M. Nagae, Y. Kusano, T. Fujii and J. Takada. (1997). *Physica C*274.
- [18] I. Matsubara, H. Tanigawa, T. Ogura, H. Yamashita, M. Kinoshita and T. Kawai. (1990). *Appl. Phys. Lett.* 80.
- [19] T. S. Kayed. (2003). *Cryst. Res. Technol.* 38 (11).
- [20] Z. F. Ren and J. H. Wang. (1992). *Appl. Phys. Lett.* 61.
- [21] W. Li, D. Z. wang, J. Y. Lao, Z. F. Ren, J. H. Wang, M. Paranthaman, D. T. Verebely and D. K. Christen. (1999). *Supercond. Sci. Technol.* 12.
- [22] A. Cigan, B. Andrzejewski, G. Plesch, G. Gritzner, J. Manka and V. Zrubec. (2001). *Measurement Science Review* 1 (1).
- [23] T. S. Kayed. (2003). *Material Research Bulletin* 38 (3).
- [24] A. I. Akimov, V. Ksenofontov, S. A. Lebedev and T. M. Tkachenka. (2006). *Physica C: Superconductivity* 443.

Jordan Journal of Physics

ARTICLE

Modeling Atmospheric Turbidity at Zarqa Area Using Meteorological Data

S. Hamasha^a, M. Abu-Allaban^b and A. Abulaban^c

^a Department of Physics, The Hashemite University, Zarqa-Jordan.

^b Department of Water Management & Environment, The Hashemite University, Zarqa-Jordan.

^c California Department of Water Resources, Fresno, CA, USA

Received on: 14/8/2007 ; Accepted on: 13/3/2008

Abstract: Clearness index (k) and atmospheric turbidity over Zarqa have been calculated using solar data obtained by a GS1 Dome Solarimeter for the period from 25th of June 2001 to 18th of May 2002. The clearness index found to be highly scattered and never exceeded 0.8. Several attempts were made in order to find a correlation between the clearness index and turbidity with measurable meteorological parameters such as air temperature, relative humidity, and atmospheric pressure. No correlations were found. However, when the clearness index was plotted against the daily temperature range (ΔT), an exponential trend that is best described by the formula $k=0.13(\Delta T)^{0.52}$ was found. This result enabled us to modify traditional formula used in obtaining atmospheric turbidity through replacing the clearness index part by $0.13(\Delta T)^{0.52}$ in order to provide a mean to calculate atmospheric turbidity based on the daily temperature range.

Key Words: Clearness Index, Atmosphere, Turbidity, Air Pollution, Air Temperature, Daily Temperature Range.

Introduction

Atmospheric turbidity (T_1), is a dimensionless measure of the opacity of a vertical column of the atmosphere (Zakey, 2004). It is of great importance to research community including atmospheric scientists and solar energy researchers. T_1 is useful for understanding many physical characteristics of the structure and properties of the atmosphere (Macris, 1959). However, quantifying atmospheric turbidity is costly due to expensive instrumentation used for this purpose (Togrul and Togrul, 2002). This justifies the extensive efforts that have been spent in order to come up with empirical formula that links the atmospheric turbidity with readily measured meteorological parameters such as air temperature and water vapor content (Togrul and Togrul, 2002; Lin et al., 2005; Molineaux et al., 1995; Gueymard, 1998; Ineichen and Perez, 2002).

The clearness index (k) is defined as the attenuation of solar radiation by the atmosphere. Its value ranges from zero to one. The clearness index is affected by air pollution in both urban and rural areas. Therefore, it may serve as an indicator for air quality and air pollution by fine particles particularly for upper atmospheric layers such as the stratosphere (Zakey, 2004).

Zarqa is a growing industrial city with a population of around one million people. Zarqa hosts more than 35% of the Jordanian industrial activities including an oil refinery, a thermal power plant, steel factories, a pipe factory, a cement factory, a fertilizers factory, a wastewater treatment plant, as well as several other small industrial facilities. A total of 2400 industrial activities are registered in Zarqa Industrial Chamber. Phosphate mines and Ar-Rusaifeh landfill are other sources of air pollution in Zarqa. Motor vehicles make up additional sources of air pollution. Emissions from the oil

refinery, the power plant, and diesel trucks contain fine particulates as sulfate and volatile organic compounds (VOCs), which are known to be good light scatterers (Seinfeld and Pandis, 2006). As a result of such concentrated anthropogenic activities, the air quality in Zarqa has been deteriorating and the clearness index is not likely to be close to 1.0 under normal conditions.

This paper aims at (1) calculating k and T_1 over Zarqa using solar data and (2) developing an empirical formula that could be used in determining k and T_1 from readily measured meteorological parameters.

Instrumentation

Meteorological data is obtained using a GS1 Dome Solarimeter through Delta-T Logger Devices (Ltd, United Kingdom) for the period from 25th of June 2001 to 18th of

$$H_o = \frac{86,400 I_{sc}}{\pi} \left[1.034 \cos \left(\frac{360 N}{365.25} \right) \right] \left[\cos \phi \cos \delta \cos \omega_s + \left(\frac{\pi \omega_s}{180} \right) \sin \phi \sin \delta \right] \quad (1)$$

where,:

I_{sc} : the extraterrestrial solar irradiance outside the Earth's atmosphere (1367 W/m²)

N : Julian day of the year. It is a continuous count of days since December 31 of the previous year. For example, January 1 is the Julian day 1, February 1 is the Julian day 32, and December 31 is the Julian day 366 for the leap year.

ϕ : latitude (32.2° North for Zarqa)

$$m = \frac{P}{1013.25 \left[\cos \theta_z + 0.50572 (96.07995 - \theta_z)^{-1.6364} \right]} \quad (2)$$

where:

P : atmospheric pressure in millibar

θ_z : Zenith angle in degrees calculated from the formula:

$$\cos \theta_z = \sin(\phi) \sin(\delta) + \cos(\phi) \cos(\delta) \cos(\omega)$$

The clearness index (k) is calculated using the following formula (Jallo and Barakat, 2003):

May 2002. The filter of the Solarimeter is a blackened thermopile with a glass-covering dome. The dome acts as a filter letting-through solar radiation. The instrument's sensor has a flat spectral response in the range between 0.3 and 3.0 μm . The sensitivity of the solarimeter is 19.88×10^{-6} at 20°C and 500 W/m² and it operates in the temperature range -40 to 80°C.

Theoretical Computations

Solar radiation incident outside the Earth's atmosphere is called extraterrestrial radiation. On average, the extraterrestrial irradiance is 1367 W/m². This value varies within $\pm 3\%$ as the Earth orbits the sun. The cumulative extraterrestrial solar beam irradiance on a horizontal surface over twenty four hours (H_o) in joules per square meter (J/m²), is calculated using the following formula (Togrul and Togrul, 2002):

δ : declination angle in degrees, which is equal to

$$\delta = 23.45 \pi / 180 * \sin (2\pi * (284 + N) / 365)$$

$\omega_s = \arccos(-\tan(\phi)\tan(\delta))$ is the hour angle of sunset,

The following formula is used to compute air mass (m) at any zenith angle (θ_z), (Kasten and Young, 1989):

$$k = \frac{H}{H_o} \quad (3)$$

where H is the measured daily solar irradiance at the ground surface. The clearness index was found experimentally to depend on the daily temperature range (ΔT) such that (Togrul and Togrul, 2002):

$$k = A (\Delta T)^B \quad (4)$$

where A and B are constants determined from data fitting.

According to Molineaux et al.(1995), Linke turbidity is calculated from the formula:

$$T_l = \frac{1}{m(0.124 - 0.0656 \log(m))} \ln\left(\frac{H_o}{H}\right) \quad (5)$$

The term $\ln(H_o/H)$ in equation 5 is nothing but $-\ln(k)$, therefore equation 4 will lead to the following expression:

$$\ln\left(\frac{H_o}{H}\right) = -\ln(A(\Delta T)^B) = -\ln(A) - B \ln(\Delta T) \quad (6)$$

Substituting equation 6 in equation 5 leads to the following formula:

$$T_l = -\frac{\alpha}{m(0.124 - 0.0656 \log(m))} (\ln(A) + B \ln(\Delta T)) \quad (7)$$

Where α is a fitting parameter, which is crucial in improving data fitting in order to mimic actual data points.

Results and Discussion

Fig.1 shows the calculated daily clearness index. The clearness index is very scattered and ranges from zero to 0.8. The index is likely affected by the two potential air pollution sources; the oil refinery and the thermal power plant. Measurements took

place at the Hashemite University campus, which is located downwind from these sources. Even if the wind direction is reversed the clearness index would not be expected to be significantly different since the wind would carry fugitive dust as it passes over the desert.

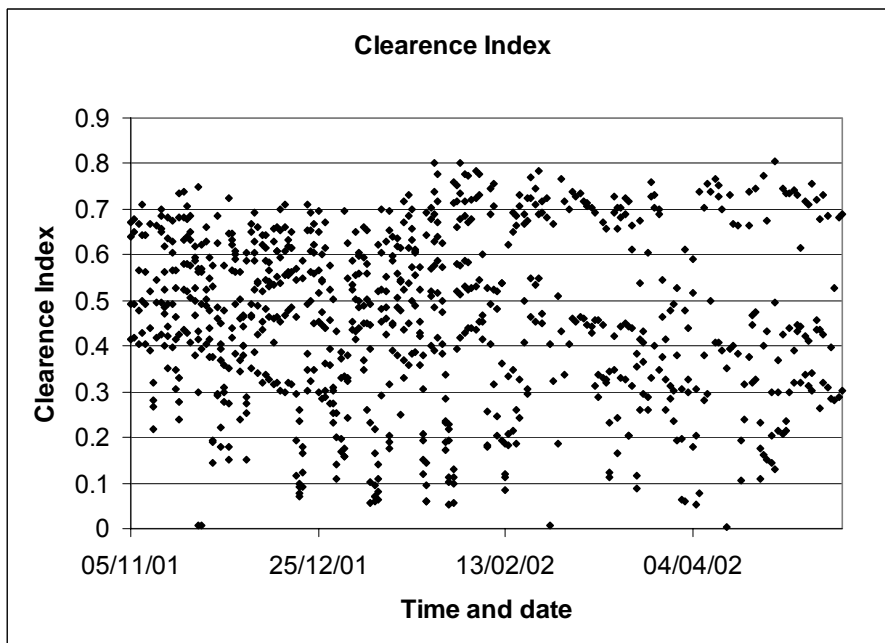


Fig. 1: Clearness index over Zarqa.

Clearness index is plotted against measured meteorological parameters including air temperature, wind speed, relative humidity, and atmospheric pressure, (Figures 2-5). No correlations were found between clearness index and the examined parameters. Moreover, as Fig.6 shows, the variation of the clearness index is in phase

with the daily temperature range. In Fig.7 the clearness index was plotted against the temperature range. A power relation was found to best fit the data. This result is supported by the finding of Jallo and Barakat (2003). The constants A and B were found to be 0.13 and 0.52, respectively.

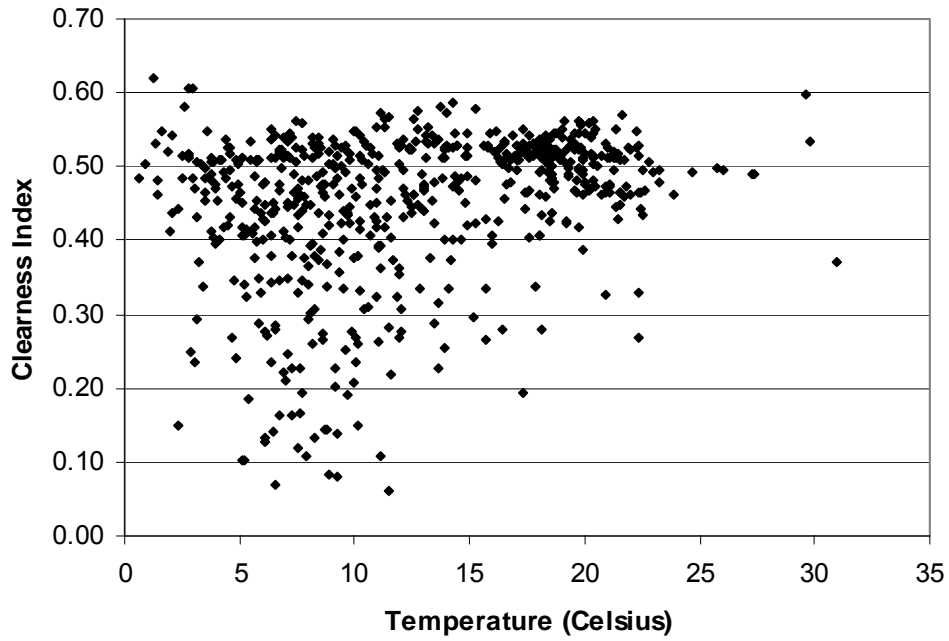


Fig. 2: Clearness index versus air temperature.

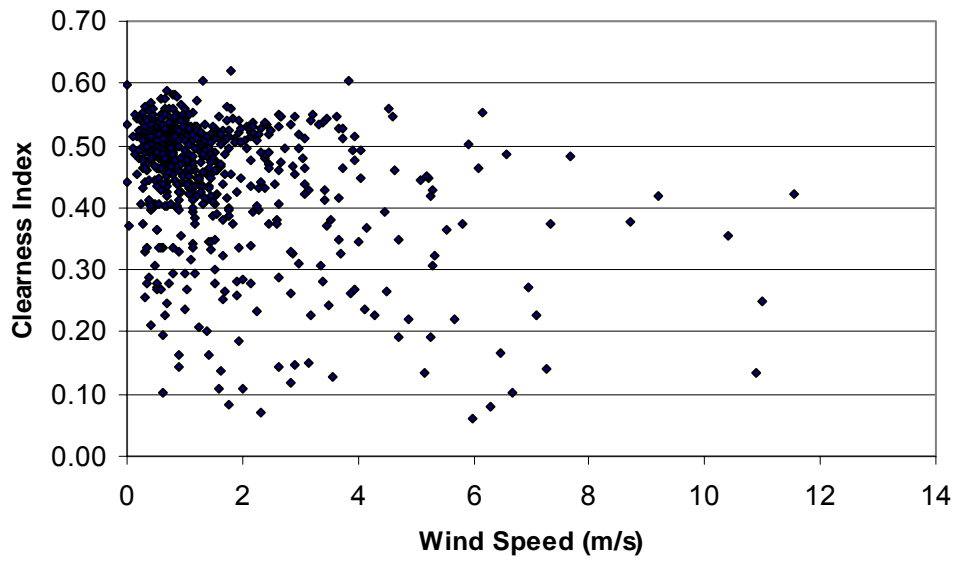


Fig. 3: Clearness index versus wind speed.

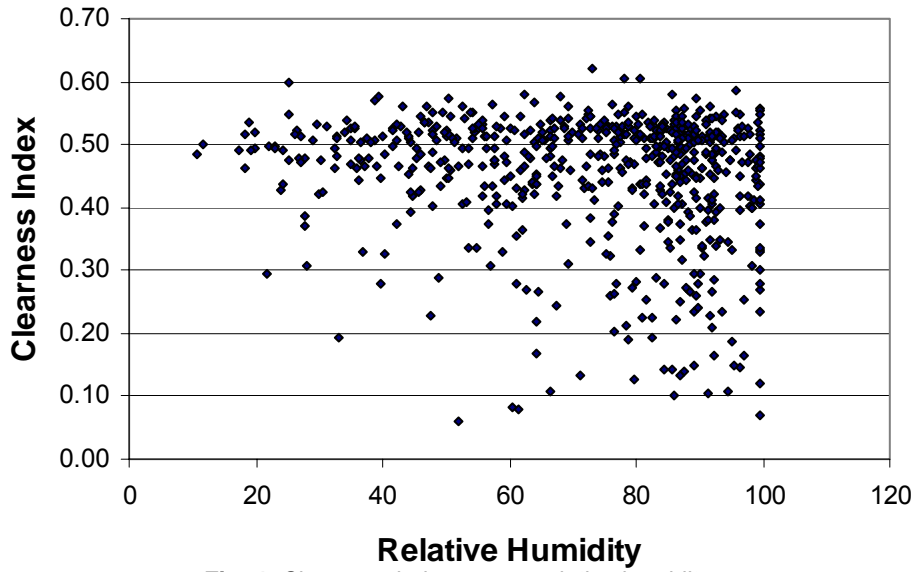


Fig. 4: Clearness index versus relative humidity.

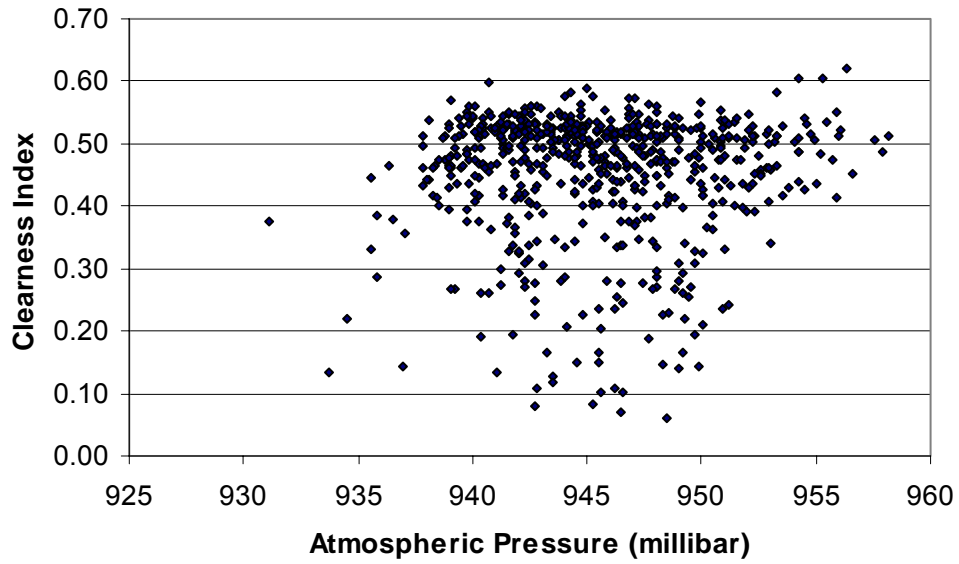


Fig. 5: Clearness index versus atmospheric pressure.

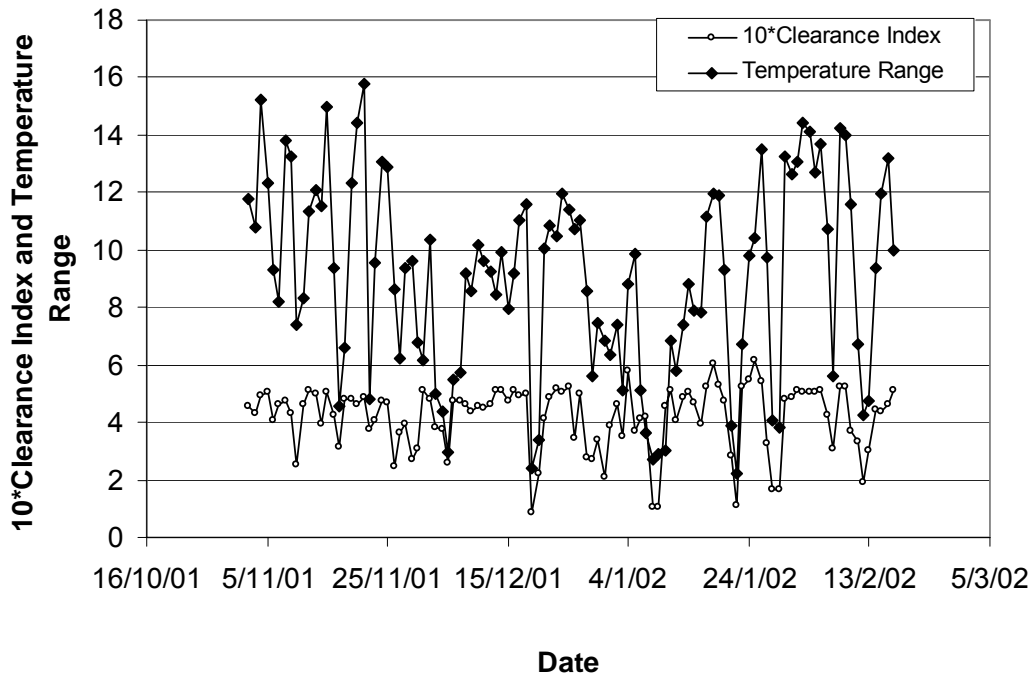


Fig. 6: Daily temperature range and clearness index over Zarqa during winter. The clearness index is multiplied by 10 in order to help visualizing its trend and how it matches the daily temperature variation.

Based on the values of the constants A and B obtained from Fig.7, the revised formula of Linke Turbidity (equations 7) can

be rewritten as a function of the temperature range as follows:

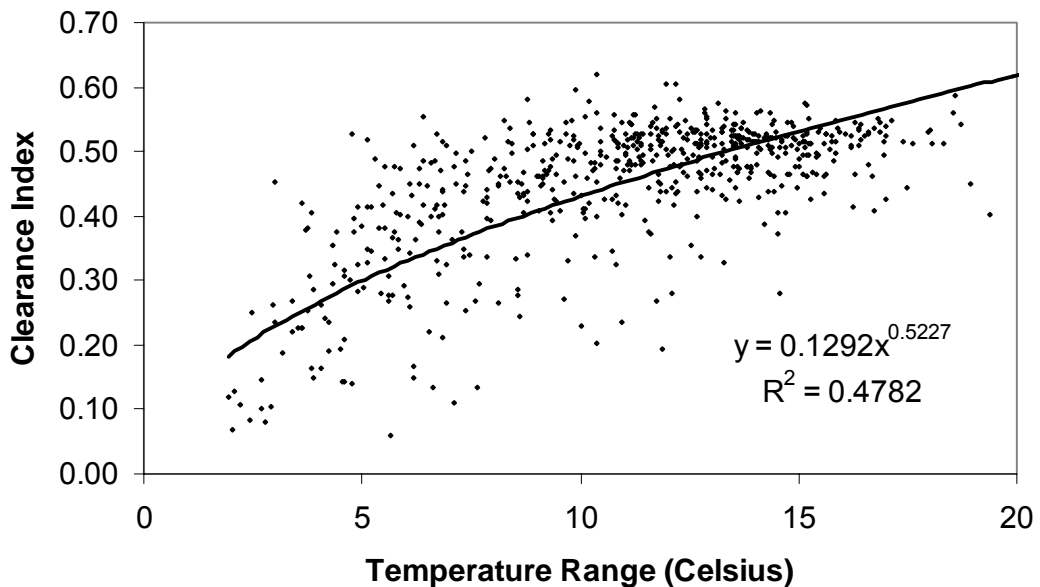


Fig. 7: The relation between the clearness index and daily temperature range.

$$T_l = - \frac{\alpha}{m(0.124 - 0.0656 \log(m))} (\ln(0.1292) + 0.5227 \ln(\Delta T)) \dots\dots (8)$$

Fig.8 presents the calculated T_l using equation 5. The figure shows that T_l is less than 10 for most of the days with few exceptions. We have also used equation 8

to calculate Linke Turbidity based on the temperature range and compared the results with the values obtained based on equation 5 using solar data (Fig.9).

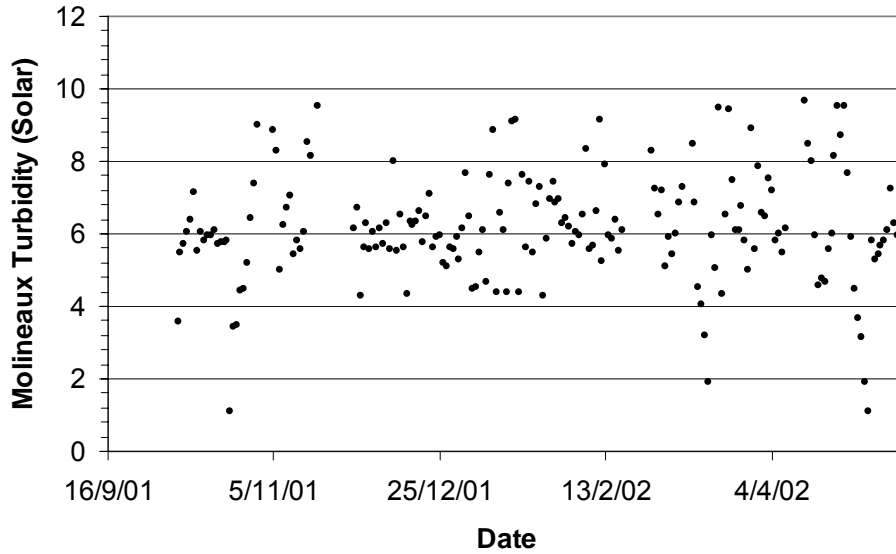


Fig. 8: Linke turbidity over Zarqa calculated based on the formula modified by Molineaux et al., (1995).

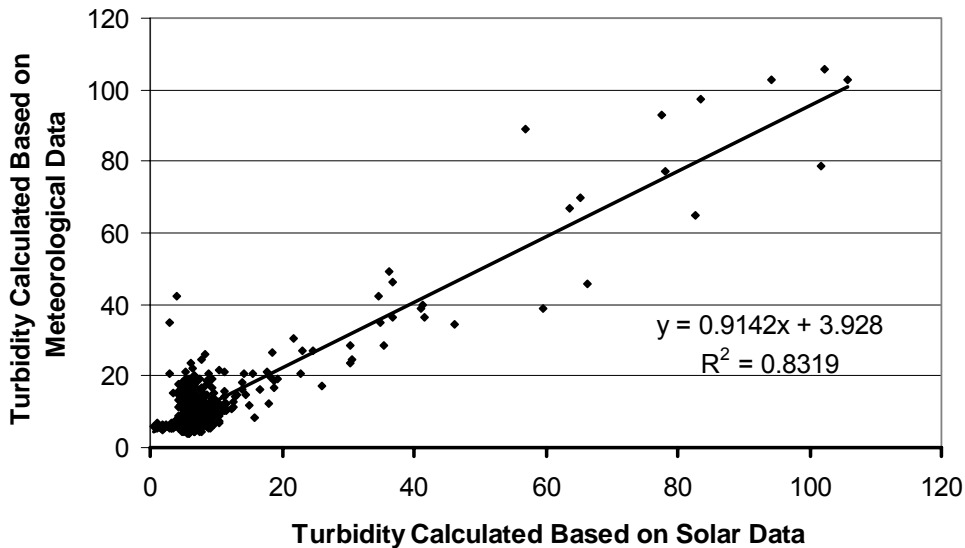


Fig. 9: Correlation between turbidity as calculated using meteorological data and turbidity as calculated using solar data. α that gave the best fit is 6.

As can be learned from Fig.9, Linke turbidity calculated using daily temperature range (solid line) matches its values obtained by applying traditional formula (dotted line). It is evident that the two techniques yield similar values. The root mean square value ($R^2 = 0.83$) indicates a strong correlation between modelled and actual values of the turbidity.

Summary and Conclusions

Clearness index and atmospheric turbidity are of great importance to a broad range of atmospheric and solar energy experts. However, quantifying them is not an easy task due to costly instrumentation needed for obtaining solar data. In this research, several attempts were made in order to come up with correlations that may

relate the clearness index and atmospheric turbidity with meteorological parameters routinely measured in traditional weather stations such as air temperature, atmospheric pressure, wind speed, and relative humidity. No significant correlations were observed. In addition, the clearness index was plotted against the daily temperature range and it was evident that there is an exponential relation of the form $k=0.13(\Delta T)^{0.52}$ between the two parameters. The power law dependence of the clearness index on the daily temperature range enabled us to modify the traditional formula used in obtaining atmospheric turbidity. The new modified formula for the atmospheric turbidity is based on the daily temperature range which is routinely measured throughout the world at low cost.

References

- Gueymard, C. A. (1998). Turbidity Determination from Broadband Irradiance Measurements: A Detailed Multicoefficient Approach. *Journal of Applied Meteorology*, 37: 414-435
- Ineichen, P. and Perez, R. (2002). A new Airmass Independent Formulation for the Linke Turbidity Coefficient. *Solar Energy*, 73 (3): 151-157
- Jallo, N. I. B. and Barakat, M. H. (2003). Comparison Between Measured Global Irradiance at the Ground Surface and Estimated Extraterrestrial Irradiance Over Zarqa City/Jordan. *Mu'tah Lil-Buhuth Wad-Dirasat*, (18); 131-145.
- Kasten, F. and A. T. Young (1989), "Revised Optical Air Mass Tables and Approximation Formula" *Applied Optics*, 28 (22): 4735-4738.
- Lin, T.H.; Liu, G.R.; Liang, C.K. (2005). To Construct an Effective Coefficient of Aerosol Size Distribution for Atmospheric Turbidity Retrieval. *TAO*, 16 (3) August, 2005, 691-706.
- Macris, G.J. (1959). Atmospheric Turbidity at Athens, Greece. *Monthly Weather Review*, November: 401-408.
- Molineaux, B.; Ineichen, P., Delaunay, J.J. (1995). Direct Luminous and Atmospheric Turbidity-Improving Model Performance. *Solar Energy* 55 (2): 125-137.
- Seinfeld, John H.; Pandis, Spyros N (2006). *Atmospheric chemistry and physics: from air pollution to climate change*. Wiley-Interscience, New York.
- Togrul, I.T., and Togrul, H. (2002). Global Solar radiation Over Turkey: Comparison of Predicted and Measured Data. *Renewable Energy* 25: 55-67
- Zakey, A.S.; Abdelwahab, M.M.; Makar, P.A. (2004). Atmospheric Turbidity Over Egypt. *Atmospheric Environment (Africa & Middle East)*, 38: 1579-1591.

Authors Index

A. Abulaban.....	53
A. Al-Khateeb	9
A. D. Alazawi.....	43
A. El Ali (Al-Dairy)	43
A. González-Angeles	37
A. Grusková	37
A. I. Al-Sharif	9
A. S. Saleh	31
I. M. Odeh	19
J. Lipka.....	37
J. Sláma	37
K. Khasawinah	43
M. Abu-Allaban.....	53
M. J. Hagmann.....	1
M. O'Shea	31
M. S. Lataifeh	31
M. S. Mousa	1
N. M. Laham.....	9
S. H. Mahmood	31
S. Hamasha	53
V. Jančárik	37
W. M. Daqa	9
Y. A. Hamam.....	43

Subject Index

Air Pollution	53
Air Temperature	53
Amorphous Materials	19
Atmosphere	53
Ball Milling	37
Ba-Sr-Ferrite	37
BSCCO.....	43
Carbon Nanotubes	1
Clearness Index	53
Crystal Structure	43
Daily Temperature Range	53
Electromagnetic Surface Waves.....	9
Field Emission.....	1
Fowler-Nordheim analysis.....	1
Heusler Alloys	31
HTSC.....	43
Ion Beam Assisted Deposition (IBAD)	19
Magnetic Order	31
Magnetic Studies.....	37
Magnetization	31
Mössbauer Spectroscopy.....	37
Optical Properties.....	19
Partial Substitution	43
Reactive Sputtering.....	19
Resistive Cylindrical Pipe.....	9
Surface Waves In Plasmas	9
TBCCO.....	43
Thin Films.....	19
Turbidity.....	53

النتائج: يستحسن عرض النتائج على صورة جداول وأشكال حيثما أمكن، مع شرح قليل في النص ومن دون مناقشة تفصيلية.

المناقشة: يجب أن تكون موجزة وتركز على تفسير النتائج.

الاستنتاج: يجب أن يكون وصفا موجزا لأهم ما توصلت إليه الدراسة ولا يزيد عن صفحة مطبوعة واحدة.

الشكر والعرفان: الشكر والإشارة إلى مصدر المنح والدعم المالي يكتبان في فقرة واحدة تسبق المراجع مباشرة.

المراجع: يجب طباعة المراجع بأسطر مزدوجة ومرقمة حسب تسلسلها في النص. وتكتب المراجع في النص بين قوسين مربعين فوق مستوى الكلمات. ويتم اعتماد اختصارات الدوريات حسب نظام Wordlist of Scientific Reviewers.

الجدول: تعطى الجداول أرقاماً متسلسلة يشار إليها في النص. ويجب طباعة كل جدول على صفحة منفصلة مع عنوان فوق الجدول. أما الحواشي التفسيرية، التي يشار إليها بحرف فوقي، فتكتب أسفل الجدول.

الرسوم التوضيحية: يتم ترقيم الأشكال والرسومات والرسومات البيانية (المخططات) والصور، بصورة متسلسلة كما وردت في النص.

تقبل الرسوم التوضيحية المستخرجة من الحاسوب والصور الرقمية ذات النوعية الجيدة بالأبيض والأسود، على أن تكون أصيلة وليست نسخة عنها، وكل منها على ورقة منفصلة ومعرفة برقمها بالمقابل. ويجب تزويد المجلة بالرسومات بحجمها الأصلي بحيث لا تحتاج إلى معالجة لاحقة، وألا تقل الحروف عن الحجم 8 من نوع Times New Roman، وألا تقل سماكة الخطوط عن 0.5 وبكثافة متجانسة. ويجب إزالة جميع الألوان من الرسومات ما عدا تلك التي ستنتشر ملونة. وفي حالة إرسال الرسومات بصورة رقمية، يجب أن تتوافق مع متطلبات الحد الأدنى من التمايز (1200 dpi Resolution) لرسومات الأبيض والأسود الخطية، و 600 dpi للرسومات باللون الرمادي، و 300 dpi للرسومات الملونة. ويجب تخزين جميع ملفات الرسومات على شكل (jpg)، وأن ترسل الرسوم التوضيحية بالحجم الفعلي الذي سيظهر في المجلة. وسواء أرسل المخطوط بالبريد أو عن طريق الشبكة (Online)، يجب إرسال نسخة ورقية أصلية ذات نوعية جيدة للرسومات التوضيحية.

مواد إضافية: تشجع المجلة الباحثين على إرفاق جميع المواد الإضافية التي يمكن أن تسهل عملية التحكيم. وتشمل المواد الإضافية أي اشتقاقات رياضية مفصلة لا تظهر في المخطوط.

المخطوط المنقح (المعدل) والأقراص المدمجة: بعد قبول البحث للنشر وإجراء جميع التعديلات المطلوبة، فعلى الباحثين تقديم نسخة أصلية ونسخة أخرى مطابقة للأصلية مطبوعة بأسطر مزدوجة، وكذلك تقديم نسخة إلكترونية تحتوي على المخطوط كاملاً مكتوباً على Microsoft Word for Windows 2000 أو ما هو استجد منه. ويجب إرفاق الأشكال الأصلية مع المخطوط النهائي المعدل حتى لو تم تقديم الأشكال إلكترونياً. وتخزن جميع ملفات الرسومات على شكل (jpg)، وتقدم جميع الرسومات التوضيحية بالحجم الحقيقي الذي ستظهر به في المجلة. ويجب إرفاق قائمة ببرامج الحاسوب التي استعملت في كتابة النص، وأسماء الملفات على قرص مدمج، حيث يعلم القرص بالاسم الأخير للباحث، وبالرقم المرجعي للمخطوط للمراسلة، وعنوان المقالة، والتاريخ. ويحفظ في مغلف واقٍ.

الفهرسة: تقوم المجلة الأردنية للفيزياء بالإجراءات اللازمة لفهرستها وتلخيصها في جميع الخدمات الدولية المعنية.

حقوق الطبع

يُشكّل تقديم مخطوط البحث للمجلة اعترافاً صريحاً من الباحثين بأن مخطوط البحث لم يُنشر ولم يُقدّم للنشر لدى أي جهة أخرى كانت وبأي صيغة ورقية أو إلكترونية أو غيرها. ويشتراط على الباحثين ملء أنموذج ينص على نقل حقوق الطبع لتصبح ملكاً لجامعة اليرموك قبل الموافقة على نشر المخطوط. ويقوم رئيس التحرير بتزويد الباحثين بأنموذج نقل حقوق الطبع مع النسخة المُرسلة للتنقيح. كما ويُمنع إعادة إنتاج أي جزءٍ من الأعمال المنشورة في المجلة من دون إذن خطي مُسبقٍ من رئيس التحرير.

إخلاء المسؤولية

إن ما ورد في هذه المجلة يعبر عن آراء المؤلفين، ولا يعكس بالضرورة آراء هيئة التحرير أو الجامعة أو سياسة اللجنة العليا للبحث العلمي أو وزارة التعليم العالي والبحث العلمي. ولا يتحمل ناشر المجلة أي تبعات مادية أو معنوية أو مسؤوليات عن استعمال المعلومات المنشورة في المجلة أو سوء استعمالها.

المجلة الأردنية للفيزياء هي مجلة بحوث علمية عالمية مُحكمة تصدر أربع مرات في العام عن اللجنة العليا للبحث العلمي، وزارة التعليم العالي والبحث العلمي، عمان ، الأردن . وتقوم بنشر المجلة عمادة البحث العلمي والدراسات العليا في جامعة اليرموك، إربد، الأردن. وتُنشر البحوث العلمية الأصلية، إضافة إلى المراسلات القصيرة Short Communications، والملاحظات الفنية Technical Notes، والمقالات الخاصة Feature Articles، ومقالات المراجعة Review Articles، في مجالات الفيزياء النظرية والتجريبية، باللغتين العربية والإنجليزية .

تقديم مخطوط البحث

تُرسل نسخة أصلية وثلاث نسخ من مخطوط البحث، مُرفقة برسالة تغطية من جانب الباحث المسؤول عن المراسلات، إلى رئيس التحرير:

أ.د. ابراهيم أبو الجرايش،

رئيس التحرير، المجلة الأردنية للفيزياء،

عمادة البحث العلمي والدراسات العليا،

جامعة اليرموك، إربد، الأردن.

هاتف : 00 962 2 72 11 111 / فرع: 3735

فاكس : 00 962 2 72 11 121

بريد إلكتروني : jjp@yu.edu.jo

ويجري تحكيم مقالات البحوث الأصلية والمراسلات القصيرة والملاحظات الفنية من جانب مُحكمين على الأقل من ذوي الاختصاص والخبرة. وتُشجّع المجلة الباحثين على اقتراح أسماء المحكمين. أما المقالات الخاصة في المجالات الفيزيائية النشطة، فتتم بدعوة من هيئة التحرير، ويُشار إليها كذلك عند النشر. ويُطلب من كاتب المقال الخاص تقديم تقرير واضح يتسم بالدقة والإيجاز عن مجال البحث تمهيداً للمقال. وتُنشر المجلة أيضاً مقالات المراجعة في الحقول الفيزيائية النشطة سريعة التغير، وتُشجّع كاتبى مقالات المراجعة أو مُستكثبيها على إرسال مقترح من صفحتين إلى رئيس التحرير. ويُرفق مع البحث المكتوب باللغة العربية ملخص (Abstract) وكلمات دالة (Keywords) باللغة الإنجليزية.

تقديم المخطوطات على الشبكة العالمية

يتوافر موقع آمن لتقديم المخطوطات الأصلية والمعدلة إلكترونياً. ويسمح أيضاً بتقديم نموذج حقوق النشر ورسالة التغطية إلكترونياً، على أن يتم إرسال نسخة موقعة من كل منها بالناسوخ (Fax) مباشرة بعد إرسالها إلكترونياً، ثم إرسال النسخة الورقية الأصلية إلى رئيس التحرير. ويوجد على موقع التقديم الإلكتروني التعليمات الكاملة للباحثين فيما يتعلق بألية تقديم المخطوط وترتيبه، والبرامج الحاسوبية التي يمكن استعمالها لتجهيز المخطوط.

ترتيب مخطوط البحث

يجب أن تتم طباعة مخطوط البحث بنيت 12 نوعه Times New Roman، ويسطر مزدوج، على وجه واحد من ورق A4 (21.6 × 27.9سم) مع حواشي 3.71سم، باستخدام معالج كلمات ميكروسوفت وورد 2000 أو ما استجد منه. ويجري تنظيم أجزاء المخطوط وفق الترتيب التالي: صفحة العنوان، الملخص، رموز التصنيف (PACS)، المقدمة، طرق البحث، النتائج، المناقشة، الخلاصة، الشكر والعرفان، المراجع، الجداول، قائمة بدليل الأشكال والصور والإيضاحات، ثم الأشكال والصور والإيضاحات. وتُكتب العناوين الرئيسة بخط غامق، بينما تُكتب العناوين الفرعية بخط مائل.

صفحة العنوان: وتشمل عنوان المقالة، أسماء الباحثين الكاملة وعناوين العمل كاملة. ويكتب الباحث المسؤول عن المراسلات اسمه مشاراً إليه بنجمة، والبريد الإلكتروني الخاص به. ويجب أن يكون عنوان المقالة موجزاً وواضحاً ومعبراً عن فحوى (محتوى) المخطوط، وذلك لأهمية هذا العنوان لأغراض استرجاع المعلومات.

الملخص: المطلوب كتابة فقرة واحدة لا تزيد على مائتي كلمة، موضحة هدف البحث، والمنهج المتبع فيه والنتائج وأهم ما توصل إليه الباحثون.

الكلمات الدالة: يجب أن يلي الملخص قائمة من 4-6 كلمات دالة تعبر عن المحتوى الدقيق للمخطوط لأغراض الفهرسة.

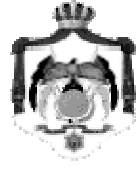
PACS: يجب إرفاق الرموز التصنيفية وهي متوفرة في الموقع <http://www.aip.org/pacs/pacs06/pacs06-toc.html>.

المقدمة: يجب أن توضّح الهدف من الدراسة وعلاقتها بالأعمال السابقة في المجال، لا ان تكون مراجعة مكثفة لما نشر (لا تزيد المقدمة عن صفحة ونصف الصفحة مطبوعة).

طرائق البحث (التجريبية / النظرية): يجب أن تكون هذه الطرائق موضحة بتفصيل كاف لإتاحة إعادة إجرائها بكفاءة، ولكن باختصار مناسب، حتى لا تكون تكراراً للطرائق المنشورة سابقاً.



جامعة اليرموك



المملكة الأردنية الهاشمية

المجلة الأردنية في
الفيزياء
مجلة بحوث علمية عالمية محكمة

المجلد (1)، العدد (1)، حزيران 2008م / جمادى الآخرة 1429هـ

المجلة الأردنية في
الفيزياء
مجلة بحوث علمية عالمية محكمة

المجلد (1)، العدد (1)، حزيران 2008م / جمادى الآخرة 1429هـ

المجلة الأردنية في الفيزياء: مجلة بحوث علمية عالمية محكمة أسستها اللجنة العليا للبحث العلمي، وزارة التعليم العالي والبحث العلمي، الأردن، وتصدر عن عمادة البحث العلمي والدراسات العليا، جامعة اليرموك، إربد، الأردن.

رئيس التحرير:

ابراهيم عثمان أبو الجرايش

قسم الفيزياء، جامعة اليرموك، إربد، الأردن.

E-mail: ijaraysh@yu.edu.jo

هيئة التحرير:

هشام بشاره غصيب

رئيس جامعة الأميرة سمية للتكنولوجيا، عمان، الأردن.

E-mail: ghassib@psut.edu.jo

نبيل يوسف أيوب

الجامعة الألمانية الأردنية، عمان، الأردن.

E-mail: nabil.ayoub@gju.edu.jo

مروان سليمان موسى

قسم الفيزياء، جامعة مؤتة، الكرك، الأردن.

E-mail: mmousa@mutah.edu.jo

سامي حسين محمود

قسم الفيزياء، جامعة اليرموك، إربد، الأردن.

E-mail: mahmoods@yu.edu.jo

ضياء الدين محمود عرفه

قسم الفيزياء، الجامعة الأردنية ، عمان، الأردن.

E-mail: darafah@ju.edu.jo

نهاد عبد الرؤوف يوسف

قسم الفيزياء، جامعة اليرموك، إربد، الأردن.

E-mail: nihad.yusuf@gju.edu.jo

جميل محمود خليفة

قسم الفيزياء، الجامعة الأردنية ، عمان، الأردن.

E-mail: jkalifa@ju.edu.jo

المحرر اللغوي: أحمد صالح.

سكرتير التحرير: مجدي الشناق.

ترسل البحوث إلى العنوان التالي: -

الأستاذ الدكتور ابراهيم عثمان أبو الجرايش
رئيس تحرير المجلة الأردنية في الفيزياء
عمادة البحث العلمي والدراسات العليا، جامعة اليرموك
إربد - الأردن

هاتف 00 962 2 7211111 فرعي 3735

Email: jjp@yu.edu.jo

Website: <http://jjp.yu.edu.jo>